Low-cycle fatigue deformation and damage behavior of equiatomic CoCrFeMnNi and CoCrNi alloys

Zur Erlangung des akademischen Grades eines

DOKTORS DER INGENIEURWISSENSCHAFTEN (Dr.-Ing.)

von der KIT-Fakultät für Maschinenbau des

Karlsruher Instituts für Technologie (KIT)

angenommene

DISSERTATION

von

M.Sc. Kaiju Lu

Tag der mündlichen Prüfung:	02. Nov. 2022
Referent:	Prof. Dr.-Ing. Jarir Aktaa Institut für Angewandte Materialien (IAM) Karlsruher Institut für Technologie (KIT)
Korreferent:	Prof. Dr.-Ing. Martin Heilmaier Institut für Angewandte Materialien (IAM) Karlsruher Institut für Technologie (KIT)

Low-cycle fatigue deformation and damage behavior of equiatomic CoCrFeMnNi and CoCrNi alloys

For the purpose of obtaining the academic degree of

DOCTOR OF ENGINEERING

from KIT-Faculty of Mechanical Engineering

of Karlsruhe Institute of Technology (KIT)

accepted

DISSERTATION

from

M.Sc. Kaiju Lu

Day of oral examination:	02. Nov. 2022
First referee:	Prof. Dr.-Ing. Jarir Aktaa
	Institute for Applied Materials (IAM)
	Karlsruhe Institute of Technology (KIT)
Co-referee:	Prof. Dr.-Ing. Martin Heilmaier
	Institute for Applied Materials (IAM)
	Karlsruhe Institute of Technology (KIT)

Abstract

Multi-principal element alloys (MPEAs) have attracted enormous scientific interest in recent years. Among them, face-centered cubic (FCC) equiatomic CoCrFeMnNi and CoCrNi model alloys have shown excellent combinations of mechanical properties. While many efforts have been made to uncover their monotonic deformation behavior, the understanding on their cyclic deformation behavior is still in infancy. This thesis aims to provide a fundamental understanding of the low-cycle fatigue (LCF) behavior and underlying mechanisms in the FCC model MPEAs.

Firstly, the LCF behavior and deformation mechanisms of CoCrFeMnNi alloy with two distinct grain sizes were systematically characterized at room temperature and 550 °C. The LCF responses including cyclic stress response and lifetime at different strain amplitudes were obtained. Extensive transmission electron microscopy (TEM) investigations revealed the microstructural evolution upon cycling. Based on these results, the influences of several testing and material parameters (including cycle number, strain amplitude, temperature, grain size and orientation) on the operating deformation mechanisms were discussed (with emphasis on dislocation slip modes and structures). Furthermore, the origins of different dislocation structures (such as walls, veins and cells) formation and some interesting phenomena (such as serrated flow and segregation) were clarified. In addition, the damage mechanisms were also examined.

Thereafter, the LCF behavior (including cyclic stress response and lifetime) and deformation mechanisms of CoCrNi alloy were investigated and compared to CoCrFeMnNi alloy. TEM investigations uncovered the microstructural reason (in terms of dislocation slip mode) for the difference in their LCF responses. The origin is further correlated to their different stacking fault energy (SFE). Hence, a strategy by tuning the SFE is identified to enhance the fatigue resistance of MPEAs.

Lastly, the LCF data of present CoCrFeMnNi and CoCrNi alloys were compared to those of a conventional FCC steel and dual-phase MPEAs. In comparison to the FCC steel, potential features that contribute to the peculiar fatigue properties of MPEAs were identified. By further comparing to dual-phase MPEAs, other effective strategies to tailor MPEAs with enhanced fatigue resistance were also elucidated.

Thus, this thesis not only serves as a reference to understand the cyclic deformation behavior and underlying mechanisms for MPEAs, but also sheds light on the strategies for improving fatigue resistance of MPEAs.

Kurzfassung

Multi-principle element alloys (MPEAs) sind neuartige metallische Legierungen, welche aus mehreren Hauptelementen bestehen. In den letzten Jahren haben diese Legierungssysteme ein außerordentliches Forschungsinteresse auf sich gezogen. Von besonderem Interesse sind die äquimolaren, kubisch-flächenzentrierten (kfz) Modelllegierungen CoCrFeMnNi sowie CoCrNi, welche eine bemerkenswerte Kombination unterschiedlicher mechanischer Materialeigenschaften aufweisen. Während das Verformungsverhalten unter monotoner mechanischer Belastung bereits tiefgreifend untersucht wurde, ist das Materialverhalten dieser neuen Legierungen unter zyklischer Beanspruchung bisher nur ungenügend erforscht. Ziel der vorliegenden Arbeit ist es, das niederzyklische Ermüdungsverhalten (low cycle fatigue, LCF) der Modelllegierungen CoCrFeMnNi sowie CoCrNi tiefgreifend zu untersuchen und ein grundsätzliches Verständnis der zugrundeliegenden Mechanismen zu entwickeln.

Zunächst wurden das LCF-Verhalten und die Verformungsmechanismen der CoCrFeMnNi Legierung im Falle von zwei unterschiedlichen Korngrößen bei Raumtemperatur und 550 °C systematisch charakterisiert. Zur Beurteilung des Kurzzeitermüdungsverhaltens der Legierung wurden die Wechselverformungskurven sowie Lebensdauern bei unterschiedlichen Totaldehnungsamplituden ermittelt. Die Mikrostrukturentwicklung während der zyklischen Belastung wurde durch detaillierte Untersuchungen mittels Transmissionselektronenmikroskopie (TEM) charakterisiert. Auf der Grundlage dieser Ergebnisse wurden die Einflüsse der Prüf- und Materialparameter (Lastspielzahl, Totaldehnungsamplitude, Temperatur sowie Korngröße und -orientierung) auf die ablaufenden Verformungsmechanismen (mit Schwerpunkt auf den Versetzungsgleitcharakter und -struktur) diskutiert. Darüber hinaus wurden die Ursachen für die Bildung unterschiedlicher Versetzungsstrukturen wie beispielsweise Venen- und Zellstrukturen aufgeklärt. Ferner sind weitere interessante Phänomene („serrated flow“ und Segregationseffekte) sowie die vorherrschenden Schädigungsmechanismen untersucht worden.

Ein weiterer Bestandteil der vorliegenden Arbeit ist die Charakterisierung des Kurzzeitermüdungsverhaltens der Modelllegierung CoCrNi im Vergleich zur CoCrFeMnNi-Legierung in Bezug auf das Wechselverformungsverhalten, die Lebensdauer sowie Verformungsmechanismen. Die Gründe für das unterschiedliche Ermüdungsverhalten der beiden Legierungen wurden durch Untersuchungen der Versetzungsstrukturen mittels Transmissionselektronenmikrokopie aufgeklärt. Der Ursprung des unterschiedlichen Ermüdungsverhaltens ist korreliert mit den unterschiedlichen Stapelfehlerenergien der Legierungen, woraus eine Strategie zur Verbesserung der Ermüdungsfestigkeit von MPEAs abgeleitet wurde.

Abschließend sind die ermittelten Daten zur Kurzzeitermüdung der CoCrFeMnNi- und CoCrNi-Legierung mit denen eines konventionellen kubisch-flächenzentrierten (kfz) Stahls sowie denen zweiphasiger MPEAs verglichen worden. Durch den Vergleich mit einem kubisch-flächenzentrierten Stahl konnten potenzielle Merkmale identifiziert werden, die zu den besonderen Ermüdungseigenschaften von MPEAs beitragen. Anhand des Vergleichs der Untersuchungsergebnisse mit dem Ermüdungsverhalten von MPEAs mit zweiphasiger Mikrostruktur wurden weitere effektive Strategien zur Anpassung der Ermüdungsfestigkeit von MPEAs ermittelt.

Die vorliegende Arbeit dient damit nicht nur als Referenz zum Verständnis des zyklischen Verformungsverhaltens und der zugrundeliegenden Mechanismen von neuartigen metallischen Legierungen mit mehreren Hauptelementen (MPEAs), sondern gibt auch Aufschluss über Strategien zur Verbesserung der Ermüdungsfestigkeit dieser Legierungssysteme.

Abbreviations

BCC	Body Centered Cubic
BF	Bright Field
CG	Coarse Grain
CTS	Critical Stress required for Twinning
DF	Dark Field
DSA	Dynamic Strain Aging
DT	Deformation Twinning
EBSD	Electron Back-Scatter Diffraction
ECCI	Electron Channeling Contrast Imaging
EDS	Energy Dispersive Spectrometry
FCC	Face Centered Cubic
GND	Geometrically Necessary Dislocation
FG	Fine Grain
GB	Grain Boundary
HAADF	High Angle Annular Dark Field
HEA	High Entropy Alloy
HCF	High Cycle Fatigue
IPF	Inverse Pole Figure
IQ	Image Quality

KAM	Kernel Average Misorientation
LCF	Low Cycle Fatigue
LD/LA	Loading Direction/Axis
MEA	Medium Entropy Alloy
MPEA	Multi-Principal Element Alloy
OM	Optical Microscopy
PSB	Persistent Slip Band
PSM	Persistent Slip Marking
RT	Room Temperature
SADP	Selected Area Diffraction Pattern
SEM	Scanning Electron Microscope
SB	Slip Band
SF	Stacking Fault
SFW	Stacking Fault Width
SRO	Short Range Ordering
STEM	Scanning Transmission Electron Microscopy
TEM	Transmission Electron Microscopy
WBDF	Weak Beam Dark Field

Symbols

$\Delta\varepsilon_{in(p)}/2$	Inelastic (plastic) strain amplitude
$\Delta\varepsilon_{e}/2$	Elastic strain amplitude
$\Delta\varepsilon_{t}/2$	Total strain amplitude
$\Delta\sigma/2$	Stress amplitude
N	Number of cycles
N_f	Number of cycles to failure (or Fatigue lifetime)
b (b_p)	Burgers vector of a full dislocation (partial dislocation)
g	Diffraction vector
K'	Cyclic strength coefficient
n'	Cyclic work hardening exponent
ε'_f	Fatigue ductility coefficient
c	Fatigue ductility exponent
ε_{cum}	Cumulative inelastic strain to failure
F	Force
ε_{true}	True strain
σ_{eng}	Engineering stress
σ_{true}	True stress
d_{act}	Dissociation width or stacking fault width
G	Shear Modulus

Table of contents

1 Introduction

1.1 Motivation & objectives

Strength and ductility are key mechanical properties of conventional metallic materials used in developing energy-efficient structural components for a wide variety of industries, including automotive, power plant, and aerospace. Unfortunately, improving strength often leads to the degradation of ductility, which is known as the strength-ductility trade-off (see Fig. 1.1 [1]). This trade-off has been a long-standing dilemma for material scientists. Therefore, it is urgent to develop engineering materials with a good combination of strength-ductility through new design and processing methods.

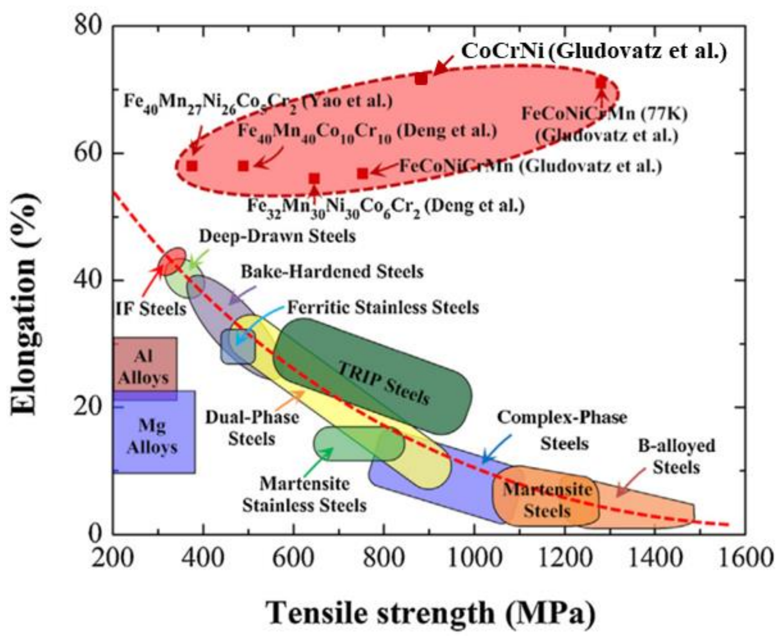

Fig. 1.1: Strength *versus* ductility trade-off for some common conventional alloys compared to that for several common MPEAs [1].

Since 2004, a newly emerged class of alloys, namely ‘high-entropy alloys, HEAs’ (or so-called ‘concentrated complex alloys, CCAs’ or ‘multi-principal element alloys, MPEAs’) has created an enormous and worldwide drive for the alloy design community [2-5]. In contrast to the conventional alloys having one or two principal elements, the MPEAs consist of three or more principal elements in a significant proportion (5 to 35 at. %). In the community, several names have been proposed, such as MPEAs, CCAs, and HEAs. In this thesis, the name of MPEAs will be used hereafter, as it might be more accurate to describe the characteristics of these alloys [6].

These MPEAs are of great interest, mainly due to two reasons. Firstly, the dramatic increase in freedom, arising from multiple elements, has provided the community with more opportunities to explore a huge variety of alloys. Secondly, many superior mechanical properties are being uncovered in these alloys, for example, tailorable strength, ductility, fatigue and fracture resistance (*e.g.*, see Fig. 1.1 [1]). For these reasons, MPEAs have been regarded as promising candidates for next-generation structural materials.

The MPEAs have been reported in various phase compositions, *e.g.*, face-centered cubic (FCC), body-centered cubic (BCC), hexagonal closed packing (HCP), and FCC-BCC dual-phase crystal structure. Among them, FCC is the most explored crystal structure in MPEAs so far. In the large pool of FCC MPEAs, the equiatomic CoCrFeMnNi and CoCrNi alloys, often regarded as model FCC MPEAs, have received the most rigorous and thorough investigations due to their good combination of mechanical properties, *i.e.*, high strength and excellent ductility [7, 8], *e.g.*, see Fig. 1.1 [1].

To date, comprehensive studies have shed light on the monotonic mechanical properties and deformation mechanisms for CoCrFeMnNi and CoCrNi alloys [7-14]. However, in service, engineering alloys are usually not only loaded monotonically but also cyclically, which leads to fatigue failures. From time to time, fatigue failures have caused catastrophic accidents, such as an explosion of a pressure vessel, a collapse of a bridge, or other complete failures of large structures/components [15]. Although exact numbers are not available, it is expected that fatigue failures take up at least half of all mechanical failures [16].

While there are many engineering design practices aimed at managing the risk of fatigue failure [2], the search or development of highly fatigue-resistant materials is also an area of active practice. In the last few decades, fatigue properties of many advanced alloy systems, such as ODS steels [17-20] and nickel-based super-alloys [21], have been investigated for their engineering applications, *e.g.*, in power plants, aerospace and automobile. Therefore, if these MPEAs (*i.e.*, CoCrFeMnNi and CoCrNi) are to be foreseen as next-generation engineering alloys, the understanding of their fatigue behavior becomes mandatory.

So far, for the CoCrFeMnNi and CoCrNi MPEAs, several studies have shed light on their fatigue crack growth behavior and high-cycle fatigue (HCF) behavior [22-26], with their low-cycle fatigue (LCF) behavior yet to be addressed. Furthermore, it is also important to compare the LCF response of the FCC MPEAs to those of conventional steels as well as another type of MPEAs (*e.g.*, dual-phase MPEAs). Such comparisons would help not only to identify the uniqueness of MPEAs' LCF behavior, but also to explore strategies for enhancing their fatigue resistance.

Therefore, the objectives of this work are:

- To elucidate the LCF deformation and damage behavior of CoCrFeMnNi alloy.
- To uncover the LCF deformation and damage behavior of CoCrNi alloy and compare it to CoCrFeMnNi alloy.
- To compare the LCF behavior of the CoCrFeMnNi and CoCrNi alloys to those of conventional steels and dual-phase MPEAs.

1.2 Structure of thesis

The thesis is organized into seven chapters.

Chapter 1 presents a general introduction, including the motivation and objectives of this work. Then the structure of this thesis is given.

Chapter 2 outlines the state of research from literature. This chapter includes detailed review of the core effects of MPEAs, monotonic mechanical properties and deformation mechanisms of CoCrFeMnNi and CoCrNi alloys, fatigue behavior of metallic materials, and fatigue behavior of MPEAs.

Chapter 3 provides details about the processing of the investigated materials (CoCrNi and CoCrFeMnNi). Then, the applied experimental procedures (including LCF-test conditions and microstructural characterization methods) are described.

Chapter 4 systematically characterizes the LCF deformation behavior (including cyclic stress response and lifetime) of CoCrFeMnNi for two different grain sizes at room temperature (RT) and 550 °C. Afterwards, extensive microstructural evidence is presented to uncover the detailed deformation-induced features. Based on the evidence, the effects of testing parameters (including strain amplitudes, cycle number, and temperature) and material parameters (such as grain orientation and size) on the operating deformation mechanisms are documented. Some interesting phenomena such as serrated flow and segregation are also discussed in this chapter. In addition, the damage mechanisms are revealed by examining fracture surfaces and crack growth profiles.

Chapter 5 showcases the LCF response of CoCrNi at RT and compares it to CoCrFeMnNi alloy. Then the microstructural evidence is given to reveal the origins of the difference in their LCF behavior. Furthermore, the observed difference is correlated to their distinct SFEs. Besides, the damage mechanisms are investigated and compared to CoCrFeMnNi alloy.

Chapter 6 compares the LCF response of CoCrFeMnNi to a conventional FCC steel, which identified potential features contributing to the peculiar fatigue properties of MPEAs. Afterwards, the LCF data of the present FCC MPEAs are compared to dual-phase MPEAs to explore strategies to improve fatigue resistance.

Chapter 7 summarizes important findings from this work and puts forward proposals for future investigations.

2 State of research

This chapter reviews several key aspects that are closely relevant to the objective of this work. These include core effects of MPEAs, monotonic mechanical properties and deformation mechanisms of CoCrFeMnNi and CoCrNi MPEAs, as well as fatigue behavior of conventional metallic materials, CoCrFeMnNi and CoCrNi MPEAs.

2.1 Core effects of multi-principal element alloys (MPEAs)

Before going into details about the mechanical properties and deformation mechanisms of MPEAs, the present introduction briefly reviews the four 'core effects' of MPEAs, namely, high-entropy effect, lattice distortion effect, sluggish diffusion, and 'cocktail' effect, which are regarded as their peculiarities and have attracted many interests [4, 27].

The first effect is the claim that MPEAs would have a strong tendency to form simple solid solutions due to high configurational entropy. This has been argued to not always hold, as the potential effects of vibrational, electronic and magnetic terms cannot be ignored. For example, Otto et al [28] investigated the possibility of forming solid solution in different equiatomic MPEAs, consisting of five similar-sized elements to ensure similar configurational entropy. They considered CoCrFeMnNi as the base and explored the effect of Ti, Mo, V and Cu (each as an alternative, respectively, *e.g.*, CoCrFeMnCu) on the phase stability of these MPEAs [28]. Results show that multi-phase occurs in all alloy systems except for CoCrFeMnNi, suggesting that high configurational entropy alone does not determine solid solution formation by counteracting the driving force of secondary phase formation [28].

The second effect postulates that these alloys are inherently strong because of the large lattice distortion caused by the mixing of different elements (with different atomic radius). This idea is misleading, as each system needs to be evaluated individually before drawing any conclusions regarding lattice distortion and solid solution strengthening. In other words, the strength of a MPEA is not determined by the sheer number of alloying elements; rather the type of element matters. For instance, the ternary CoCrNi alloy has a higher strength than the quinary CoCrFeMnNi alloy and three quaternary alloys (FeNiCoCr, NiCoCrMn, FeNiCoMn) [9].

The third effect is that these MPEAs would have a lower diffusion coefficient due to atomic level variation of the individual jump barriers induced by the mixture of different elements. Although this was reported to be true in some conditions, *e.g.*, in Ref [29], others claimed that diffusion should not be assumed sluggish in MPEAs due to the mere increase of the number of elements; in fact, the type of elements plays a more pronounced role [30]. Therefore, the low diffusivity seems to be dependent on the system and there is no fundamental reason to relate it to entropy alone.

The fourth 'cocktail effect' in fact is not a 'novel core' effect but rather a reminder pointing towards non-linear and unexpected property accomplishment in MPEAs, primarily owing to unusual microstructures and elemental compositions. This effect is more abstract than others and needs careful analysis on highlighting the synergistic improvement in properties.

Overall, the four 'core effects' are still under passionate debate; nevertheless, they provide initial insights and motivation for the development of novel structural materials.

2.2 Monotonic mechanical properties and deformation mechanisms of CoCrFeMnNi and CoCrNi MPEAs

The mechanical properties and deformation mechanisms of FCC CoCrFeMnNi and CoCrNi alloys under monotonic loading have been extensively investigated [7, 9-13, 31-35], which is beneficial for understanding their cyclic deformation behavior and mechanisms.

For CoCrFeMnNi, at RT, and for a mean grain size of ~ 4−6 μm, it shows a tensile yield strength of ~ 370 MPa and an elongation to failure of ~ 60% [10]. It is often asserted that the high strength of this alloy is due to improved solid solution strengthening from multiple constituent elements, as compared to conventional alloys [3, 36, 37]. Besides, at RT, the Hall-Petch slope of the CoCrFeMnNi alloy was determined to be 494 MPa√μm, which is higher than that of conventional FCC metals, ~ 90-230 MPa√μm [38]. This suggests the MPEA's larger grain boundary strengthening. The increase in the ductility is due to a delayed onset of necking instability, which originates from high and steady work hardening that persists to higher strains at lower temperatures due to the onset of deformation twinning [31].

As a ternary derivative from the Co-Cr-Fe-Mn-Ni system, the FCC CoCrNi alloy exhibits an even better combination of mechanical properties [7, 9-13]. For instance, at RT, a tensile yield strength of ~ 430 MPa and an elongation to failure of ~ 70% have been reported for a non-uniform grain size of 5−50 µm [8]. The main reasons for the superior mechanical properties of CoCrNi are 1) its higher shear modulus (most likely coming from the higher Cr content and the large volumetric mismatch between Cr (as the largest atom in the system), and Ni and Co (both comparably small) [6, 36]) and 2) an earlier onset of deformation twinning (resulting in dynamic Hall-Petch strengthening, due to its lower (~ 25%) stacking fault energy, SFE, as compared to CoCrFeMnNi [12, 39, 40]).

The understanding of operating deformation mechanisms is critical to tune the mechanical properties of MPEAs. In terms of CoCrFeMnNi alloy, the early-stage plasticity is characterized by planar slip of 1/2<110> dislocations on {111} planes at a wide temperature range of 77−873 K [10]. Some of the dislocations split into 1/6<112> Shockley partials bounding stacking faults [32, 40], while others remain as full 1/2<110> dislocations [10]. At larger strain levels, the dislocations reorganize themselves into cell structures [32].

Similar to the deformation mechanisms of CoCrFeMnNi [10], the early-stage plasticity of CoCrNi is also characterized by the glide of 1/2<110> dislocations, which mostly dissociated into 1/6<112> Shockley partials on {111} planes [12]. Moreover, with increasing strain/stress until a critical resolved shear stress (of about 260 MPa) is reached, numerous deformation twins (DTs) are triggered in CoCrNi [12]. These DTs could impede dislocation motion and lead to an enhanced work-hardening, which delays the onset of necking; hence together, resulting in enhanced strength and ductility [12].

Note here, all the slip systems and dislocation reactions in FCC crystals can be represented by the well-known Thompson tetrahedron (see Fig. 2.1a). Moreover, an example of dislocation reactions (*i.e.*, 1/2<110> full (or perfect) dislocations splitting into two 1/6<112> Shockley partials with in-between stacking faults) is illustrated in Fig. 2.1b. The dissociation width (d_{act}) between two partials can be approximately expressed by the following equation [41]:

$$d_{\mathrm{act}} = \frac{Gb_{\mathrm{p}}^{2}}{4\pi SFE} \qquad \text{Eq. 1}$$

Here, G is shear modulus, b_p is Burgers vector of partial dislocations, and SFE is the stacking fault energy of a material. Accordingly, the d_{act} is inversely proportional to the SFE of the material.

Furthermore, DTs in FCC crystals are generally thought to be formed by planar glide of Shockley partials with the same Burgers vector on the successive {111} planes [41].

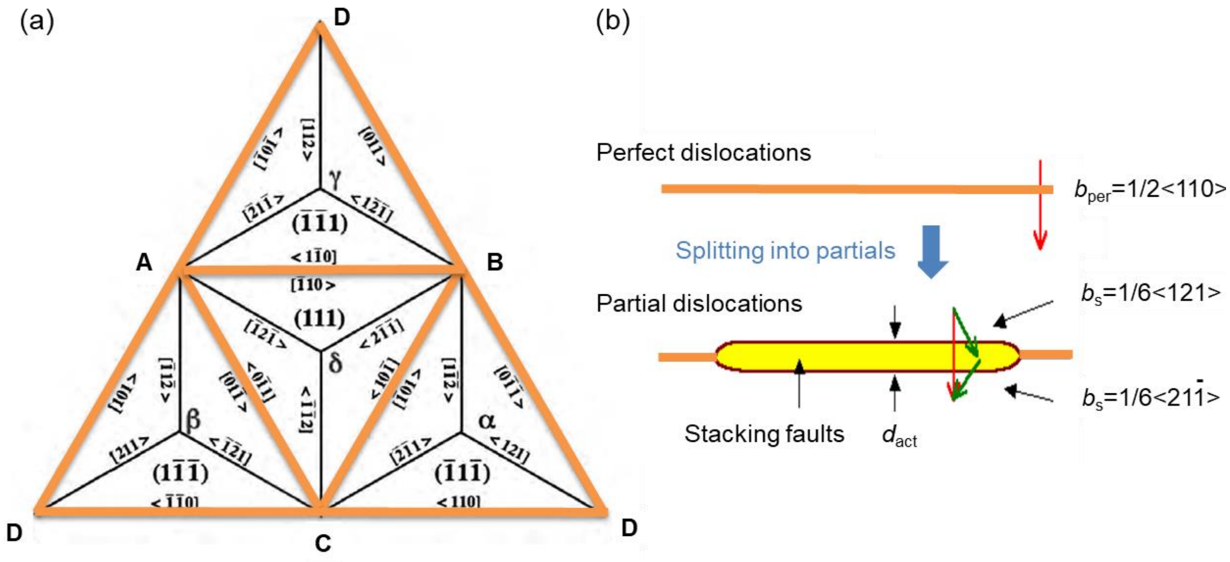

Fig. 2.1: (a) a 2-D view of Thompson tetrahedron [42]. The orange lines indicate Burgers vectors for full dislocations and the black lines refer to Burgers vectors of Shockley partials. The four {111} slip planes are indicated by α, β, γ and δ, respectively. (b) A schematic showing dislocation reaction: the dissociation of a 1/2<110> full dislocations into two 1/6<112> Shockley partial dislocations.

2.3 Fatigue behavior of conventional metallic materials

To understand the fatigue behavior of MPEAs, it is important to introduce the key perspectives of fatigue behavior for conventional metallic materials.

2.3.1 Low-cycle fatigue

For an engineering designer, fatigue analysis is mainly concerned with the evaluation of potential fatigue lifetime (N_f). Depending upon the testing conditions, *e.g.*, stress or strain amplitude, fatigue life varies significantly and accordingly can be classified. In detail, when the strain (or stress) amplitude exceeds 0.2% (or yield strength), the N_f is usually less than 10^4 cycles, lying in the so-called low-cycle fatigue (LCF) regime. In contrast to LCF regime, when strain/stress amplitude falls within elastic limit (*i.e.*, < 0.2% offset strain or yield strength), the N_f lies in comparatively higher regime ($10^5 < N_f < 10^7$, referred to as high-cycle fatigue (HCF) regime).

In laboratory conditions, fatigue tests are usually carried out under constant stress or strain conditions. Generally, stress-controlled tests are used in evaluating the components or materials that are deformed primarily elastically (*i.e.*, in the HCF stage). In this case, the strength of the material determines its fatigue resistance, with the crack initiation being the life-determining event. While, strain-controlled tests are preferably used in examining fatigue properties in the LCF stage, during which plastic deformation dominates. Here, the lifetime depends more on the ductility of the material, as the crack propagation determines its fatigue resistance [16].

2.3.2 Cyclic stress response

Fatigue failure is not a sudden event that occurs unexpectedly. Rather, it is the final event that has been preceded by a sequence of cyclic deformation and fatigue processes. For ductile metals, different stages of cyclic deformation and fatigue processes can be discerned, involving cyclic hardening/softening, cyclic saturation, the evolution of fatigue damage led by cyclic slip irreversibility, initiation and subsequent propagation of macrocrack up to failure [43].

Among these stages, cyclic hardening/softening and saturation behaviors can be examined by recording the peak stress at each cycle. For example, during strain-controlled LCF tests, if the peak stress increases (or decreases) with number of cycles, then it is referred to as cyclic hardening (or softening) (see Fig. 2.2a-b [44]). If the peak stress remains (nearly) constant, it is termed as (near-) saturation stage or steady-state.

In materials that do not deform appreciably (*e.g.*, brittle materials) and that contain defects acting as pre-exiting cracks, stages I and II can be largely absent upon cycling. While in ductile materials, initial cyclic hardening and/or softening stage show up, depending on the material's initial microstructure. For instance, annealed materials usually undergo initial hardening, while pre-deformed materials usually experience initial softening. Afterwards, a (near-) saturation stage can be reached in both cases, reflecting a balance between hardening and dynamic recovery events. At this stage, cyclic strain localization frequently sets in, leading to transgranular cracking at the surface [45]. Detailed descriptions of this behavior can be found in several review works [43-45].

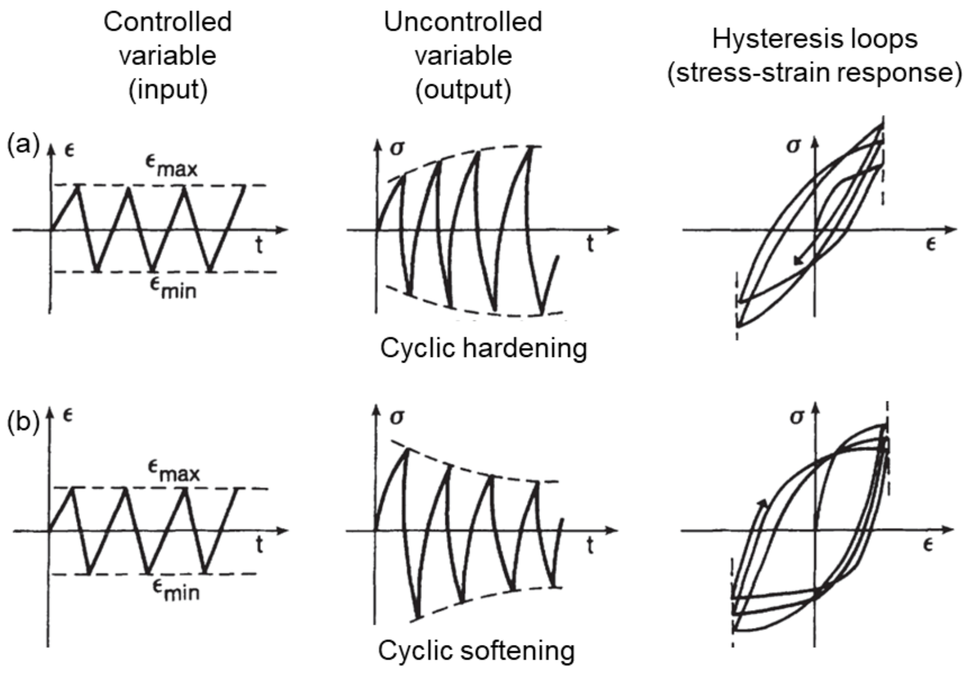

Fig. 2.2: Schematic illustration of materials response to cyclic strain-controlled input [44].

2.3.3 Microstructural features upon cycling

Fatigue is characterized by a series of forward and reverse loading. Under LCF loading, plasticity is induced in each cycle. In ductile FCC materials, the plasticity is carried by the multiplication and accumulation of defects, mainly in the form of dislocations. This behavior results in an increase in dislocation density, which forms unique structures to minimize the total elastic strain energy of the system [45]. Hence, the cyclic deformation behavior of ductile FCC materials is strongly associated with microstructural evolution, particularly dislocations movement and forming structures.

The dislocation's motion can be classified into planar slip (two-dimensional) and cross/wavy slip (three-dimensional, *i.e.*, by which a screw dislocation changes its slip plane). It has been well-accepted that the ease of cross slip mainly depends on the SFE of materials [41]. Generally, FCC materials with higher SFE have a larger tendency to cross slip. This is because: the higher SFE and hence lower separation distance promote partial dislocations constriction into full dislocations, among which screw ones have the potential to cross slip. On the other hand, for low-SFE materials, cross slip is more difficult to achieve. This is because: the low-SFE leads to easy dissociation of full dislocations into Shockley partial ones. When dissociation occurs, a 1/6<112> vector lies in only one {111} plane and so an individual Shockley partial cannot cross slip [41] (see Fig. 2.1a). Nevertheless, it is possible to form a constriction in the screw dislocation and then the full dislocation at the constriction can glide in another {111} plane. Hence, more energy is required to form a constriction to allow for cross slip in low-SFE materials.

Therefore, depending on the prevalent slip mode, dislocations could arrange into different low-energy structures upon cyclic loading. In specific, due to the easy cross slip of screw dislocations in materials with high-SFEs, dislocations can easily arrange themselves into substructures (*e.g.*, veins, persistent slip bands (PSBs), labyrinth, walls and cells) to localize plastic deformation [16, 41, 46-50]. In contrast, in materials with low-SFEs, slip bands (SBs), partial dislocations, stacking faults and deformation twins are prominent dislocation structures [16, 51, 52].

It is also of interest to note that, apart from the SFE, chemical short-range ordering (SRO), if existed, also plays an important role in determining dislocations' slip mode. For instance, Gerold and Karnthaler reported that the SRO could promote planar slip [53].

Notably, in comparison to wavy slip, planar slip is believed to effectively enhance slip reversibility of dislocations, which contributes to less strain localization and thus plays a positive role in delaying the fatigue crack initiation and increasing the resistance to fatigue crack growth [54].

2.3.4 Fatigue crack initiation and growth

In FCC ductile materials, the above-mentioned microstructural features (*e.g.*, PSBs and SBs) are generally related to the localization of cyclic slip (*i.e.*, unreversed slip steps) at the sample surface; thereby, are precursors to crack initiation. Upon further loading, these features could form so-called persistent slip markings (PSMs) including intrusions and extrusions, see Fig. 2.3 [48]. These intrusions and extrusions act as local stress concentration raisers that favor the nucleation of microcracks [48, 55, 56]. Hence, understanding the microstructural evolution (*e.g.*, dislocation motion and forming substructures) upon cycling is of great significance for evaluating the fatigue initiation behavior of materials.

After initiation, the microcracks will grow as a result of further cyclic loading. In ductile materials, crack growth is regarded as a process of intense localized deformation in slip bands near the crack tip, generating new crack surfaces by shear decohesion [44].

In the beginning, crack growth occurs predominantly by single shear in the direction of primary slip system (termed as stage I crack growth) [44]. The crack growth rate of stage I is generally very low and the fracture surface is practically featureless [44]. During stage I, grain boundaries often act as strong barriers to crack growth. The length of the stage I crack is generally in the order of several grain sizes, depending on materials and loading amplitudes [44].

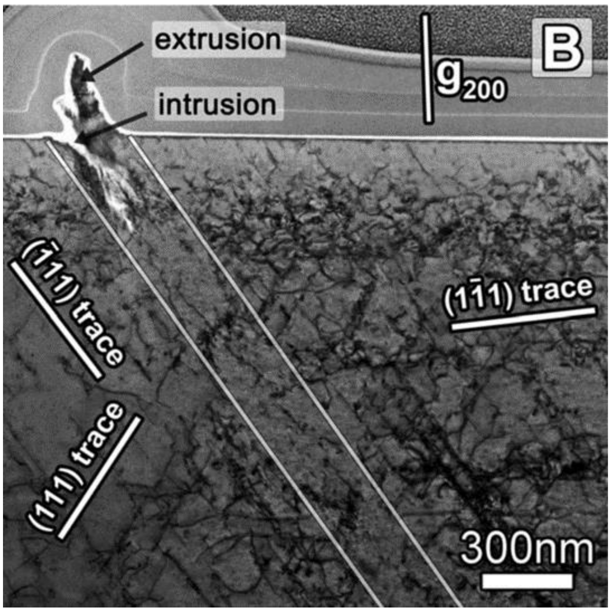

Fig. 2.3: A TEM micrograph showing the persistent slip markings in austenitic Sanicro 25 steel consisting of extrusion and intrusion, and a crack starting from the tip of the intrusion [48]. Dislocation arrangement in the persistent slip band is ladder-like [48].

Thereafter, with further cyclic loading, the crystallographic crack (stage I) changes direction and propagates in a non-crystallographic plane. This plane is approximately perpendicular to the loading direction (called stage II crack growth). Stage II crack growth is often called a continuum crack propagation, which is due to more constrained interior grains having more than one slip plane activation [44]. Stage II is characterized by ductile features called 'striations' on fracture surfaces, which are ascribed to crack-tip blunting and resharpening due to cyclic plasticity.

Additionally, the general nature of fatigue crack growth in metallic materials can be described by fracture mechanics in terms of the variation in crack growth rate ($\frac{da}{dN}$) as a function of the nominal stress intensity range[1] (ΔK). The fatigue crack growth rate for most ductile materials displays the following characteristics: 1) a region at low values of ΔK and da/dN ($< \sim 10^{-9}$ m/cycle) in which fatigue cracks appear dormant below the

[1] Stress intensity range: $\Delta K = Y \cdot \Delta\sigma \cdot (\pi a)^{0.5}$, where Y is a geometric factor, $\Delta\sigma$ is the stress range and a is the crack length.

fatigue threshold, ΔK_{TH}; 2) an intermediate region (~ 10^{-9} to 10^{-6} m/cycle) of power-law behavior described by the Paris equation [2] [57]; 3) an upper region of accelerating crack growth (> ~ 10^{-6} m/cycle) [58].

Taking together, fatigue life generally is divided into two stages, namely, fatigue crack initiation lifetime and growth lifetime. However, the reliable definition of the transition from crack initiation to growth has always been difficult. The main difficulties lie in 1) the limited resolution of observations, and 2) the definition of the crack length that terminates initiation [43].

2.4 Fatigue behavior of CoCrFeMnNi and CoCrNi MPEAs

2.4.1 Fatigue behavior of CoCrFeMnNi alloy

So far, for the CoCrFeMnNi alloy, several studies have shed light on their fatigue crack growth behavior and HCF behavior [22-25]. For instance, Thurston et al. [22] examined fatigue-crack propagation behavior of CoCrFeMnNi alloy at RT (293 K) and 198 K, and found it comparable to austenitic steels and TWIP steels. They reported that the threshold stress intensity factor range, ΔK_{TH}, increased from ~ 4.8 MPa√m to ~ 6.3 MPa√m with decreasing temperature from 293 K to 198 K [22]. Moreover, crack paths indicate transition from predominantly transgranular at RT to intergranular-dominant at 198 K [22].

Kim et al. [23] investigated the HCF behavior of CoCrFeMnNi with a coarse grain size of around 245 μm at RT. They found that initially present Cr-Mn based oxides act as crack sources [23]. Chlup et al. [25] studied three-point bending HCF behavior of two ultra-fine-grained (0.4 μm and 0.6 μm) CoCrFeMnNi alloys. They revealed that the CoCrFeMnNi with smaller grain size reached slightly better fatigue properties [25]. Besides, the formation of nano-twins together with the localized extensive slip activity in abnormally large grains acted as the fatigue crack initiation sites [25]. Furthermore, Suzuki et al. [59] revealed that dislocation planarity leads to slip localization, which

[2] Paris law: $\frac{da}{dN} = C(\Delta K)^m$, where *C* and *m* are both material constants.

causes slip-plane cracking in CoCrFeMnNi during HCF loading. In addition, Tian et al. [24] reported that the fatigue strength of the CoCrFeMnNi could be ameliorated by refining grain size. These studies provide important information on the fatigue crack growth behavior and the HCF behavior of CoCrFeMnNi MPEA.

Recently, an increasing number of investigations have also been dedicated to unraveling the LCF behavior of CoCrFeMnNi [60-64]. For example, Wang et al. [60] studied the LCF cracking behavior of CoCrFeMnNi. They found a transition from slip band (SB) cracking to twin boundary cracking with an increase in the difference in Schmid factors between matrix and twins [60]. During the course of this work, Shams et al. [61] found that CoCrFeMnNi alloy shows longer LCF life at high strain amplitudes (> 0.4%) compared to SS304 steel. At the same time, Picak et al. [64] investigated the LCF behavior of both coarse and ultrafine grained CoCrFeMnNi. They reported that ultrafine grained samples demonstrated a superior fatigue life at the lower strain amplitudes [64]. The above works offer initial insights into the LCF response of CoCrFeMnNi alloy. Nevertheless, several other important questions still remain open:

- What are the cyclic stress responses of CoCrFeMnNi alloy? What are the underlying microstructural origins for these responses, *i.e.*, dislocation motion and forming substructures?

- The applied strain amplitude often acts as a dominating role in determining the fatigue lifetime. How does it affect the underlying microstructural evolution (*i.e.*, deformation mechanisms)?

- Temperature influence on the LCF deformation behavior of MPEAs is a fundamental question and also is essential for their applications at various temperature conditions. How does the temperature affect the LCF behavior and corresponding deformation mechanisms?

- Reducing grain size is usually an effective way to improve materials' fatigue performance [65, 66]. As a previous study [60] concerning the grain size effect was only limited to LCF crack initiation behavior in CoCrFeMnNi at low strain amplitudes, what would be the grain size effect on LCF deformation behavior for a wider strain amplitude range?

- The relation between grain orientation and distinct dislocation structures is a fundamental scientific issue and has been well-documented for FCC single crystals (*e.g.*, copper, nickel) [67, 68]. For instance, dislocation wall and labyrinth structures dominate in near [011] and [001]-oriented grains, respectively [67]. Can this trend be extended to FCC polycrystalline MPEAs?

These questions will be addressed in Chapter 4.

2.4.2 Fatigue behavior of CoCrNi alloy

In contrast to the above-mentioned extensive studies on CoCrFeMnNi alloy, far too little attention has been paid to the cyclic deformation behavior of CoCrNi alloy. During the course of this work, Rackwitz et al. [26] revealed a superior fatigue crack propagation resistance of CoCrNi compared to CoCrFeMnNi. However, it remains open how CoCrNi alloy would perform under LCF loading? Furthermore, CoCrNi has shown a better combination of mechanical properties compared to CoCrFeMnNi [12]. Further work is needed to verify whether this trend also holds for the LCF behavior.

Moreover, as introduced in Section 2.3.3, the LCF behavior of FCC materials is strongly associated with their dislocation slip mode, which is significantly affected by the SFE [69]. With CoCrNi and CoCrFeMnNi, these are two model MPEAs that differ in their SFEs (*e.g.*, CoCrNi 22 ± 4 mJ/m^2 [12] *versus* CoCrFeMnNi 30 ± 5 mJ/m^2 [40]). Hence, it is also essential to identify whether the observed difference in their LCF behavior is driven by the SFE? This would help explore a potential SFE-based strategy for improving fatigue resistance of MPEAs.

These questions will be addressed in Chapter 5.

2.4.3 Comparisons to conventional steels and dual-phase MPEAs

For MPEAs' safety-related engineering applications, it is significant to compare the LCF response of FCC MPEAs with conventional FCC steels, particularly those already in engineering use (*e.g.*, 316L steels). Generally, austenitic stainless steels show an initial hardening, followed by a softening and finally a subsequent near-steady response, before failure [70]. Increasing strain amplitude tends to accelerate the formation of more complex and dense substructures [70]. Therefore, it is of interest to specify the following question, *i.e.*, how would their cyclic responses and microstructural evolutions differ? This would also help the alloy design community to identify the potential features contributing to peculiar fatigue properties of MPEAs; and hence, allow for tuning them more efficiently.

In addition, dual-phase (*e.g.*, FCC matrix and BCC precipitates) MPEAs have been reported to exhibit higher strength, sufficient ductility and better HCF resistance compared to single-phase FCC MPEAs [71-76]. For example, Shukla et al. [74] investigated the HCF behavior of $AlCoCrFeNi_{2.1}$ alloy with hard BCC phase and soft FCC phase in lamellar morphology. Such a duplex microstructure is found to delay crack initiation as BCC phase blocks PSBs path [74]. Liu et al. [75] reported on the $Al_{0.3}CoCrFeNi$ HEA (with FCC, hard B2 and sigma phases) which exhibited excellent fatigue resistance due to the formation of deformation twins and the matrix's large dislocation accumulation capability. Furthermore, Zou et al. [77] addressed that the Al addition into CoCrFeMnNi thin foils (with FCC and BCC phases) can effectively decrease cyclic strain localization and improve bending fatigue resistance. However, concerning the LCF behavior, the comparison between FCC and dual-phase MPEAs is limited. Hence, it is also necessary to compare the LCF response of FCC MPEAs to that of dual-phase MPEAs, which would help further explore potential strategies for tailoring MPEAs with enhanced fatigue resistance.

The above aspects will be covered in Chapter 6.

3 Materials & methods

This chapter provides details on the processing of investigated materials. Afterwards, experimental procedures such as fatigue testing and microstructural characterization are presented.

3.1 Synthesis of materials

In general, for the investigated CoCrFeMnNi and CoCrNi alloys, the synthesis route involves five typical steps: arc/induction melting, casting, homogenization[3], cold-working[4] and annealing, see Fig. 3.1. The corresponding details for both materials are provided in the following subsections.

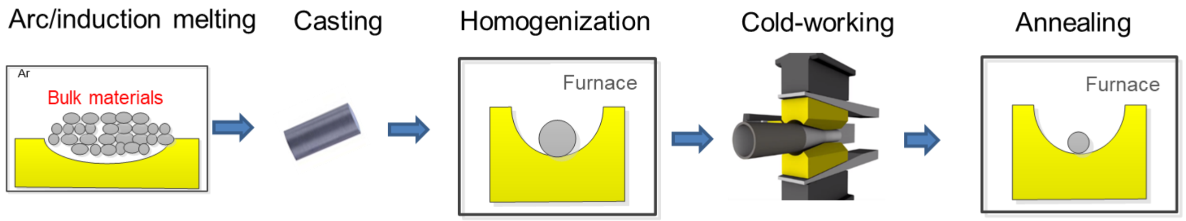

Fig. 3.1: A schematic illustration showing synthesis route for CoCrFeMnNi and CoCrNi alloys.

3.1.1 CoCrFeMnNi alloy

The investigated CoCrFeMnNi was synthesized from high purity elemental bulk materials (with at least 99.95 wt.% purity). Initially, Co, Cr, Fe, Mn, and Ni elements were arc melted five times and then drop cast under pure Ar atmosphere in rod-shaped water-cooled Cu mold. Thereafter, the ingot was homogenized at 1473 K for 72 h and subsequently water quenched. The homogenized material was then subjected to rotary swaging with which the diameter was reduced from 14 mm to 6 mm with an areal

[3] The procedures including arc/induction melting, casting and homogenization for the investigated CoCrFeMnNi and CoCrNi alloys were carried out in the laboratories of Prof. Dr. M. Heilmaier in KIT and Prof. Dr. G. Laplanche in Ruhr University of Bochum, respectively.

[4] The cold-working (rotary-swaging) was carried out in the laboratory of Prof. Dr. J. Freudenberger in Leibniz Institute for Solid State and Materials Research Dresden.

reduction per pass of strain of $\varepsilon \approx 0.19$ (*i.e.*, a diameter reduction per pass of strain of $\varepsilon \approx 0.1$).

The LCF specimens (see Fig. 3.2 and Fig. 3.3 for their shape and size) were fabricated from the cold-worked rod along the swaging direction. Before LCF tests, two batches of fabricated specimens were annealed at 1073 K and 1273 K for 1 h, respectively, to obtain fully recrystallized microstructures with two distinct grain sizes (*fine-grained*, ~ 6 μm and *coarse-grained*, ~ 60 μm) differing by one order magnitude.

3.1.2 CoCrNi alloy

The investigated CoCrNi alloy was synthesized from pure metals (with at least 99.9 wt.% purity) by vacuum induction. The CoCrNi melt was poured in a cylindrical steel mold with a 45 mm diameter that was coated with zirconia slurry. The as-cast ingots were homogenized at 1473 K for 48 h and water-quenched. Subsequently, the alloys were rotary swaged to ~ 6 mm in diameter with an areal reduction per pass of $\varepsilon \approx 0.19$.

The same-type of LCF specimens were machined out from the rotary-swaged rod along the swaging direction. Finally, to ensure a fair comparison to CoCrFeMnNi, LCF specimens of CoCrNi were annealed for 1 h at 1098 K to obtain a recrystallized microstructure and similar fine grain sizes (~ 6 μm).

Additionally, it is worth noting that previous EDS and XRD analyses confirmed that both investigated CoCrFeMnNi and CoCrNi alloys contain uniform distribution of equiatomic elements and single-phase FCC structure [12, 33]. The lattice parameter is 3.597 Å for CoCrFeMnNi [33] and 3.567 Å for CoCrNi [12].

3.2 Low-cycle fatigue testing

All cyclic pull-to-push LCF-tests were carried out in air on an MTS 810 servo-hydraulic testing machine equipped with a radiative furnace and a high-temperature extensometer (having a 7 mm gauge length, from MAYTEC with model PMA-12/V7/1), see Fig. 3.2 [78].

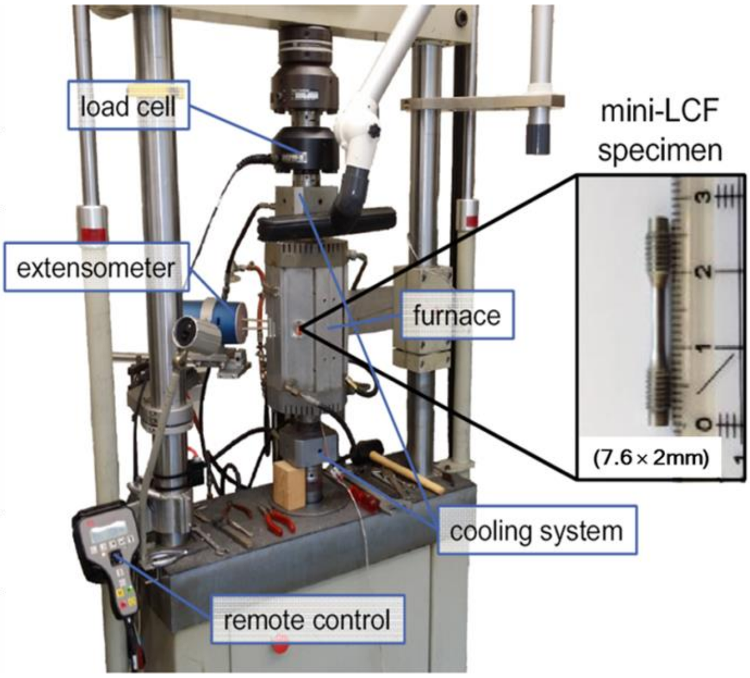

Fig. 3.2: MTS testing setup with miniaturized specimen [78].

Due to the limited quantity of material (as it was produced in a laboratory scale), the miniaturized specimen with a gauge diameter of 2 mm and length of 7.6mm, was used, see Fig. 3.3. The specimen design was developed within the framework of irradiation programs at Karlsruhe Institute of Technology (KIT), Germany [79].

LCF-tests (up to failure) were conducted at RT and 550°C under a nominal strain rate of 3×10^{-3} s^{-1} using a symmetrical triangular waveform. The applied total strain amplitude ranged from 0.2% to 0.8%. In specific, at RT, the applied total strain amplitude includes 0.3%, 0.5%, (0.6%), and 0.7% (with two tests per condition) for CoCrFeMnNi and CoCrNi; whereas, at 550 °C, it is 0.2%, 0.3%, 0.4%, 0.5%, 0.75%, and 0.8% (with one test per condition, due to limited amount of material) for CoCrFeMnNi. These strain amplitudes were chosen to ensure that the lifetime is within the LCF regime.

Additionally, interrupted LCF-tests (up to 20 and 500 cycles, respectively) were performed at RT and 0.5% strain amplitude, which was used to characterize the microstructural evolution for CoCrFeMnNi. The reason for choosing these numbers of cycles will be given in Section 4.4.1.2.

During the high-temperature testing (*i.e.*, 550 °C), the furnace temperature variation was controlled within ± 2 °C by Pt-PtRh thermocouple attached directly to the shoulder of the specimens. The testing temperature of 550°C is chosen, as it lies within the proposed operating temperature range for advanced nuclear reactors and/or power plants [78]. The dwell time before starting the test was at least 30 min after reaching the target temperature.

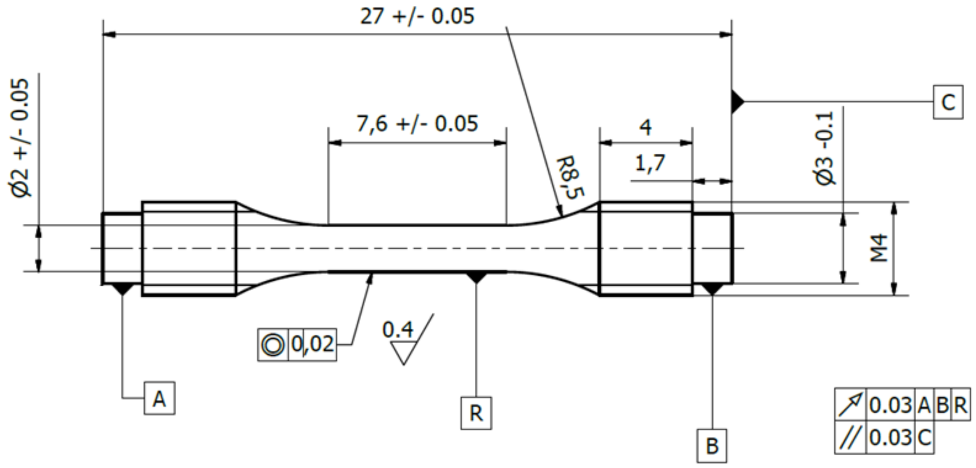

Fig. 3.3: Technical drawing of the LCF specimen [78].

To protect the testing machine and the extensometer, the fatigue test was terminated before the specimen was completely broken using a simple procedure in the commercial MTS software. The data from each test, including time, number of cycles (N), force (F) and true strain (ε_{true}, based on the measured elongation and initial gauge length) were stored in a text file using the MTS software. Thereafter, the engineering stress (σ_{eng}) at each cycle was calculated based on the recorded force and initial cross-section. Then it was conveyed into the true stress (σ_{true}) for further analysis.

Additionally, the inelastic strain amplitude ($\Delta\varepsilon_{in}/2$) and stress amplitude ($\Delta\sigma/2$) per cycle were determined from the hysteresis loop using MATLAB script coded by Dr. Ankur Chauhan [78]. Among them, the $\Delta\varepsilon_{in}/2$ is approximately regarded as the half-width of the hysteresis loops at zero stress, $\Delta\varepsilon_p/2$, as they are almost equivalent herein (with difference of ~ 3%) (see Fig. 3.4a). The lifetime (N_f) was defined as the number of cycles at which the peak stress (σ_{max}) dropped by a specific percentage (X%=10%) in relation to the linear stage, using the ASTM Standard E2714-13 [80] (see Fig. 3.4b).

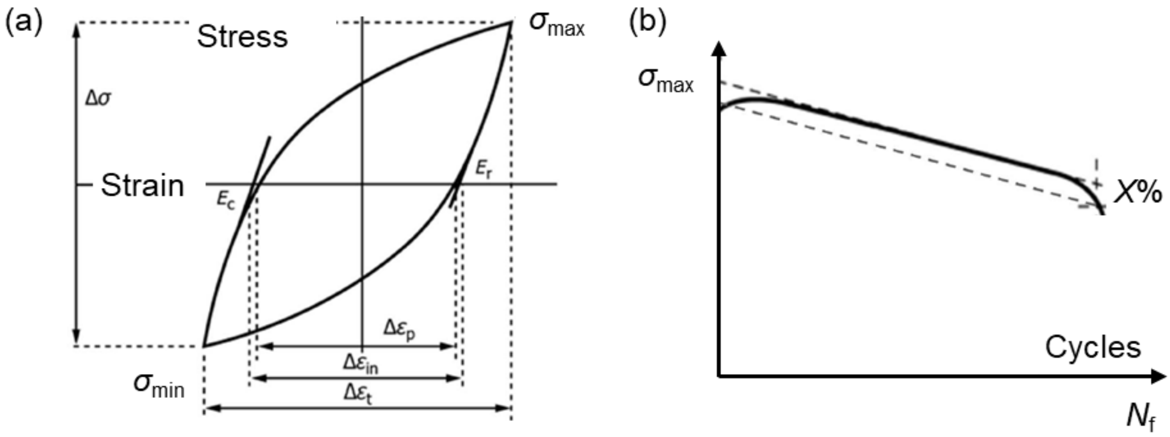

Fig. 3.4: Schematic representation showing (a) several stress/strain parameters (peak stress σ_{max}, stress amplitude $\Delta\sigma/2$, inelastic strain amplitude $\Delta\varepsilon_{in}/2$, and total strain amplitude $\Delta\varepsilon_t$) from hysteresis loop, and (b) fatigue life (N_f) according to ASTM standard E2714-13 [80].

3.3 Microstructural characterization methods

Microstructural evolution (including recrystallized and post-fatigued microstructures) was characterized by using electron backscatter diffraction (EBSD) and transmission electron microscopy (TEM).

3.3.1 Sample preparation for microstructural investigations

For EBSD investigations, the specimens were prepared by cutting thin strips from the gauge section of deformed samples, parallel to the loading direction (// LD), using a Well's diamond wire saw. These strips were then mechanically ground (with P600-4000 SiC abrasive papers) and polished (with 9 μm, 3 μm and 1 μm water-based diamond suspensions using MD/DP-Pan, MD/DP-Mol, and MD/DP-Nap polishing clothes, respectively, from Struers company), with each steps taking 5 to 10 mins. Finally, the strips were polished on a Buehler vibratory polisher (with a 50 nm colloidal suspension of silica and a MicroCloth polishing cloth (Item 42-3712, from Buehler company) for 12 to 24 h.

TEM specimens were taken from the above-mentioned strips. These specimens were further ground to a thickness of ~ 100 μm, and then 3 mm discs were punched out of them. Thereafter, the discs were further thinned by electro-polishing using a Tenupol

5 twin-jet device with a 1.8mm holder. Electro-polishing was carried out using an electrolyte consisting of 10 vol. % perchloric acid, 20 vol. % glycerin, and 70 vol. % methanol at ~ (-20 to 0) °C and ~ 13 V with a flow rate of 50. The polishing process was shut off automatically (taking from 30 s to 2 mins) as soon as a hole appears in the center of the sample (see Fig. 3.5).

After electro-polishing, the electron-transparent zone in the sample was examined by optical microscopy (OM) and TEM to identify the loading direction or axis (LD or LA) of the sample for grain orientation analysis [81] (see Fig. 3.5).

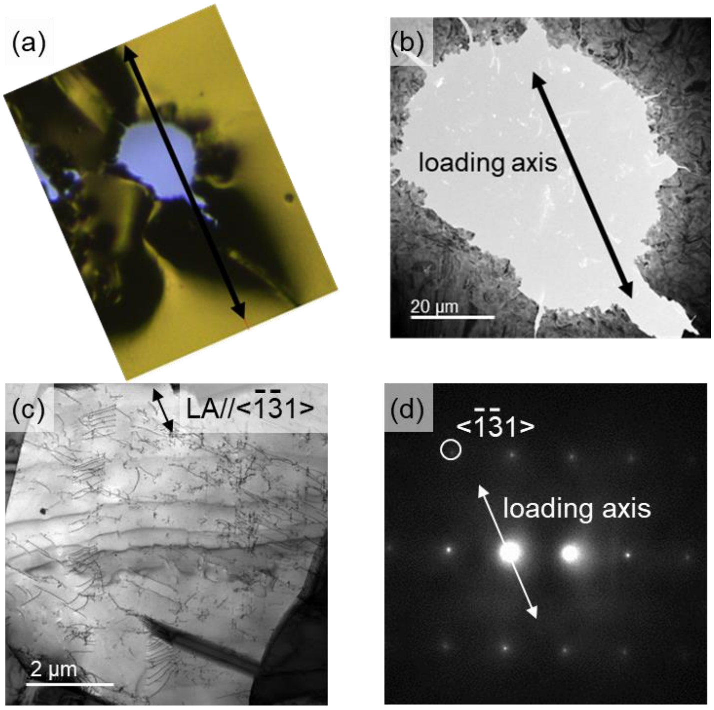

Fig. 3.5: An example to show the electron-transparent zone in an electro-polished sample: (a) an OM micrograph with marked loading axis, and (b) corresponding low magnification TEM micrograph. (c) A TEM micrograph of CoCrFeMnNi and corresponding (d) diffraction pattern, which is obtained at untitled condition to identify grain orientation of the grain in (c).

3.3.2 Scanning and transmission electron microscopy (SEM/TEM)

EBSD investigations were carried out using an FEI 200 Dual-Beam SEM/FIB equipped with an HKL EBSD detector. EBSD scans were acquired at an accelerating voltage of 20 kV, a beam current of 1.7 nA, a working distance of 10 mm, and a step size of 200 nm. The acquired EBSD data were processed using EDAX's OIM software (version 9.0), such as to obtain kernel average misorientation (KAM) maps for evaluating the intragranular misorientation after cycling.

In KAM maps, the average misorientation between a point and its neighboring points (up to 1st nearest neighbors) was calculated. The kernel exclusion criterion which excludes points with misorientation exceeding 5° was applied during this estimation. The calculated values can be visualized in the form of a color-coded map. As KAM considers only misorientations in a small local neighborhood within a grain, it also provides a good estimation of the local geometrically necessary dislocation (GND) density [82]. In specific, higher KAM values correspond to higher local misorientations (*i.e.*, higher GND density) and vice versa.

To further analyze the microstructural evolution at a higher resolution, scanning TEM (STEM) and conventional TEM analyses were performed. For this purpose, an FEI Tecnai F20 TEM equipped with a high-angle annular dark-field (HAADF) detector and energy dispersive spectrometry (EDS) system was employed operating at an accelerating voltage of 200 kV with a double-tilt holder.

Selected area diffraction patterns (SADPs) were used to identify the zone axis and potential deformation twins. Besides, the orientation of an investigated grain is also determined by capturing the diffraction pattern, which then corresponds to the loading axis [81] (*e.g.*, see Fig. 3.5c-d).

Both the bright-field (BF) and '$\boldsymbol{g}$-3$\boldsymbol{g}$' weak beam dark-field (WBDF) modes were used to examine the dislocation structure in different two-beam diffraction conditions. At two-beam conditions, the crystal is tilted to a large and positive value of excitation error $\boldsymbol{s}$.

In FCC materials, a pair of dislocations can be either a pair of dislocation dipoles or Shockley partial dislocations with in-between SF. To identify the nature of a pair of dislocations, the two-beam BF-mode micrographs are obtained at $+\boldsymbol{g}$ and $-\boldsymbol{g}$ conditions. If the spacing between the pair dislocations in the two micrographs (at $+\boldsymbol{g}/-\boldsymbol{g}$ conditions) varies, then the pair is dipole (comes from diffraction theory [83-85]).

Otherwise, the pair is a pair of partial dislocations. In addition, the partial dislocations (along with bounding SFs) can be visualized by the WBDF imaging technique.

To determine the Burgers vector (***b***) of perfect dislocations, the '***g***·***b***' invisibility criteria was employed (see Table 3.1), where the ***g*** vector is obtained from a two-beam condition.

Table 3.1: Values of ***g***·***b*** for perfect dislocations in FCC crystals to identify the Burgers vector (***b***) at different two-beam diffraction conditions (***g***). The value 0 means that the dislocation with the Burgers vector ***b*** is invisible at the ***g*** condition.

Plane of dislocations	***g*** / ***b***	$1\bar{1}1$	$11\bar{1}$	$\bar{2}00$
$(1\bar{1}1)$ or $(1\overline{11})$	½$[110]$	0	1	$\bar{1}$
$(1\overline{11})$ or $(11\bar{1})$	½$[101]$	1	0	$\bar{1}$
$(1\bar{1}1)$ or $(11\bar{1})$	½$[011]$	0	0	0
(111) or $(11\bar{1})$	½$[1\bar{1}0]$	1	0	$\bar{1}$
(111) or $(1\bar{1}1)$	½$[10\bar{1}]$	0	1	$\bar{1}$
(111) or $(\bar{1}11)$	½$[0\bar{1}1]$	1	$\bar{1}$	0

4 Low-cycle fatigue behavior of CoCrFeMnNi alloy

In this chapter, LCF behavior and operating mechanisms of CoCrFeMnNi alloy are systematically described. The contents of this chapter are organized as follows.

Section 4.1 presents the as-recrystallized microstructures, which were annealed at different temperatures to obtain two distinct grain sizes. Section 4.2 provides the LCF behavior including cyclic stress response and lifetime at both RT (with emphasis on grain size effect) and 550 °C. Section 4.3 provides damage mechanisms of CoCrFeMnNi alloy. Section 4.4 shows the microstructural evolution upon cycling at RT and 550 °C. Based on these observations, Section 4.5 discusses the operating cyclic deformation mechanisms of CoCrFeMnNi alloy at RT and 550 °C. In this section, the influences of strain amplitude, cycle number, grain orientation and temperature on the operating deformation mechanisms are clarified. Finally, Section 4.6 briefly summarizes the main findings of this chapter.

4.1 Initial microstructure

Fig. 4.1a-b show representative inverse pole figure (IPF) maps for the investigated CoCrFeMnNi after annealing at 1073 K and 1273 K, respectively. As evident, at both annealing conditions, CoCrFeMnNi exhibits equiaxed grains with a high density of annealing twins and no significant texture. The average grain sizes at the two conditions were determined to be ~ (6 ± 3) μm and ~ (60 ± 30) μm, respectively (see insets of Fig. 4.1a-b). These two variants are termed hereafter as FG and CG CoCrFeMnNi, respectively.

Furthermore, both FG and CG CoCrFeMnNi bear a low dislocation density, confirming the recrystallized state (*e.g.,* see a typical KAM map and BF-TEM micrograph in Fig. 4.1c-d for FG material).

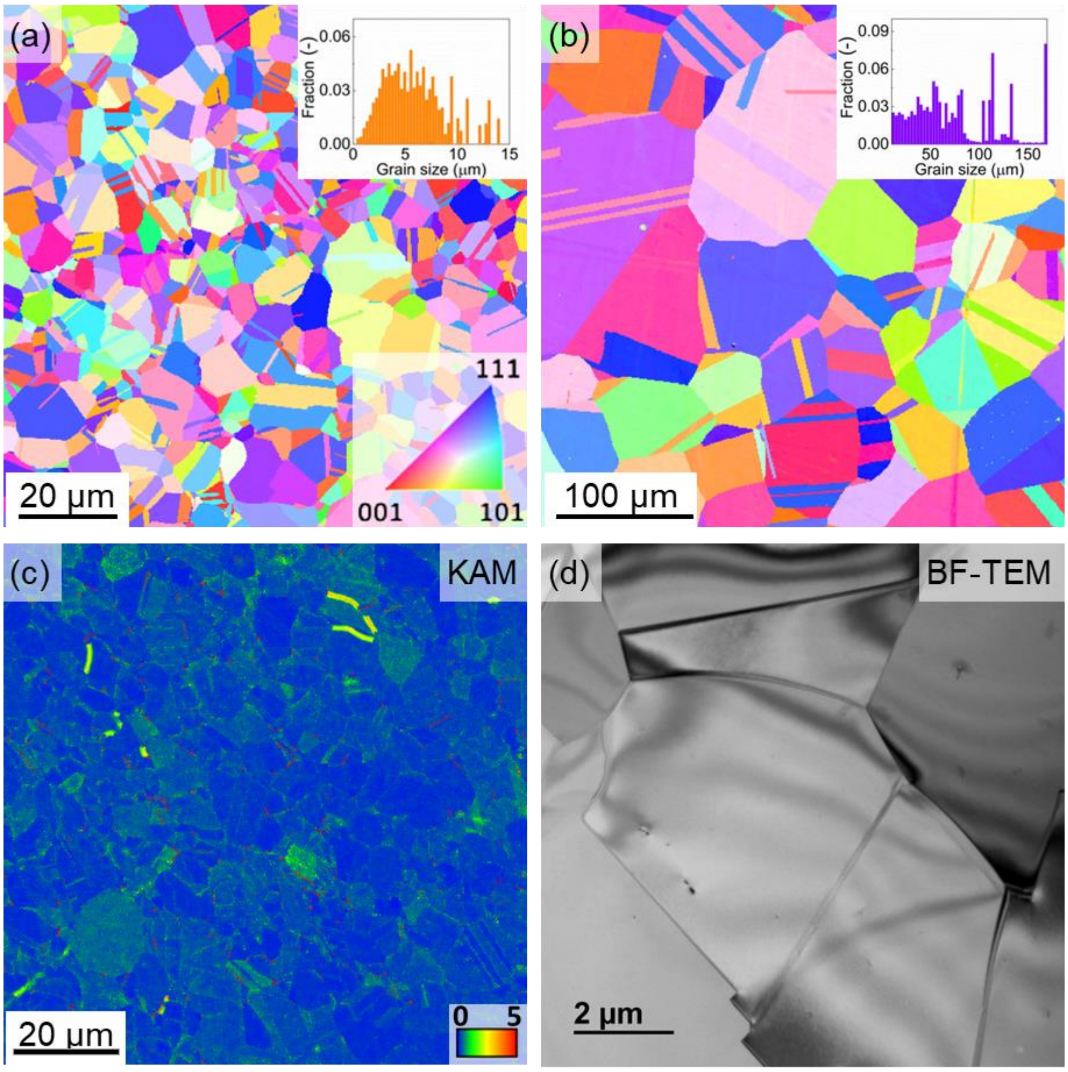

Fig. 4.1: Microstructures of CoCrFeMnNi annealed at (a, c-d) 1073 K and (b) 1273 K. Figures (a) and (b) are representative IPF maps [86]. The grain size distributions of each state are provided in the insets. Figures (c) [62] and (d) [86] are representative KAM map and BF-TEM micrograph, respectively, illustrating low initial dislocation density after annealing.

4.2 Low-cycle fatigue response

4.2.1 Low-cycle fatigue response at RT

4.2.1.1 Cyclic stress response

The cyclic response of both grain-sized materials is displayed in Fig. 4.2a-b, where tensile peak stress and inelastic strain amplitude are plotted against the *normalized* number of cycles (N/N_f), respectively. Similar curves showing these evolutions with the number of cycles (N) can be found in the supplementary material (Fig. 4.2c-d).

As shown in Fig. 4.2a and c, both FG and CG materials, in general, bear a similar cyclic stress response. Initially, the tensile peak stresses increase rapidly (cyclic hardening), followed by their rapid decrease (cyclic softening) and, finally, minor changes in their level (with either minor softening for CG or ‘near-steady state’ for FG counterpart) are observed until failure (crack nucleation and propagation).

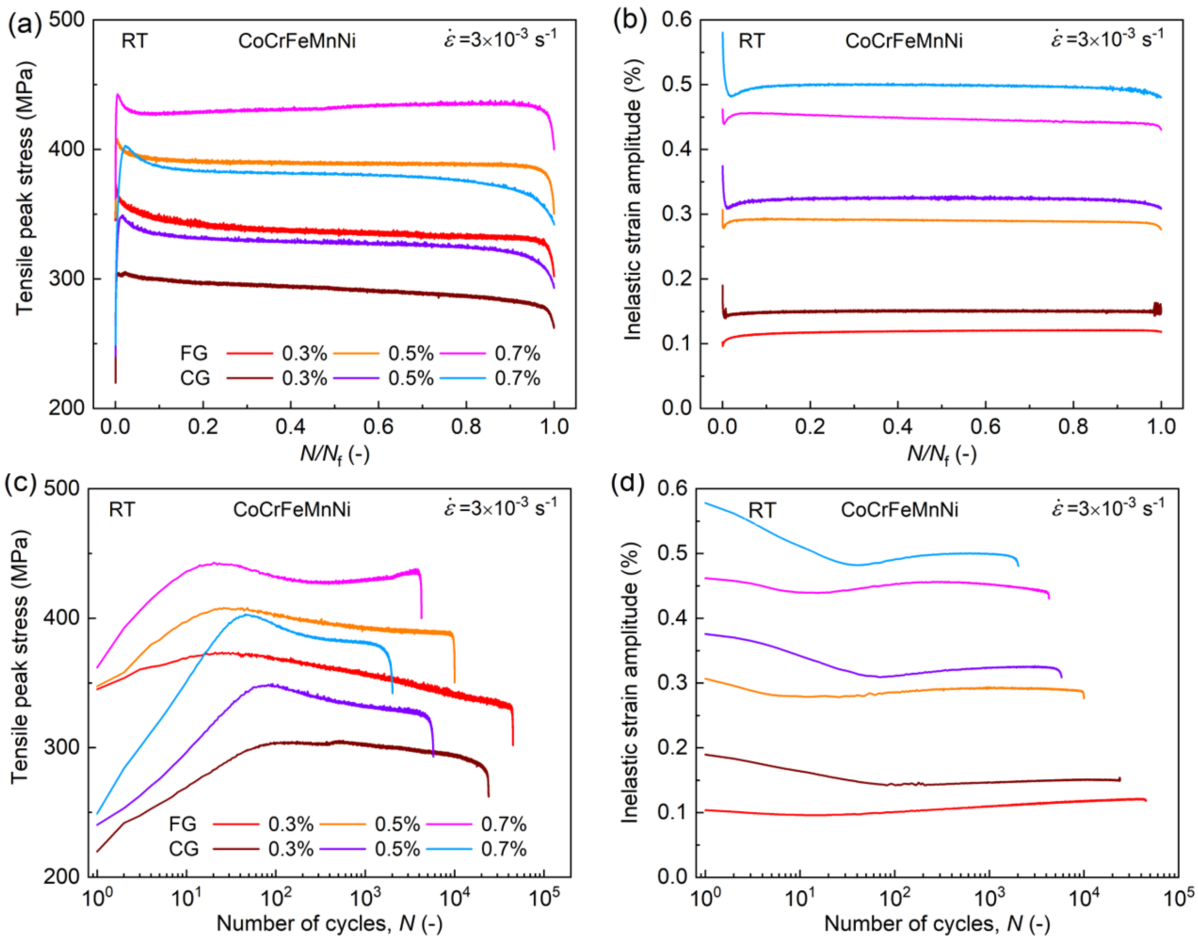

Fig. 4.2: (a) Tensile peak stress and (b) inelastic strain amplitude *versus* the *normalized* number of cycles (N/N_f) curves, (c) tensile peak stress and (d) inelastic strain amplitude *versus* the number of cycles (N) curves, for FG and CG CoCrFeMnNi under different strain amplitudes at RT [86]. The color bar in (a, c) is also valid for (b, d).

Also evident, the majority of the lifetime (~ 90%) is occupied by the last stage with a minor change in the stress levels. With respect to the influence of the applied strain amplitude, the rate and amount of the initial hardening both increase with increasing strain amplitude. Furthermore, there is an indication of secondary hardening after the near-steady state at the highest applied strain amplitude (0.7%) for the FG sample (Fig. 4.2a and c).

In comparison, FG material shows a higher cyclic strength and a lower cyclic hardening than the CG material (Fig. 4.2c). The amount of cyclic hardening is determined to be ~ 30−80 MPa and ~ 80−150 MPa for FG and CG materials, respectively (see Fig. 4.2c).

Consistent with the variation of peak stresses, the inelastic strain amplitudes in Fig. 4.2b exhibit an initial rapid decrease followed by a gradual increase and near saturation stage until failure. Moreover, the inelastic strain amplitudes of FG material are lower than those of the CG material. The lower inelastic strain in FG material is related to its higher elastic strain, ε_e, due to its higher cyclic/yield strength, as compared to CG material at comparable Young's modulus (*e.g.*, see half-life hysteresis loops in Fig. 4.3a).

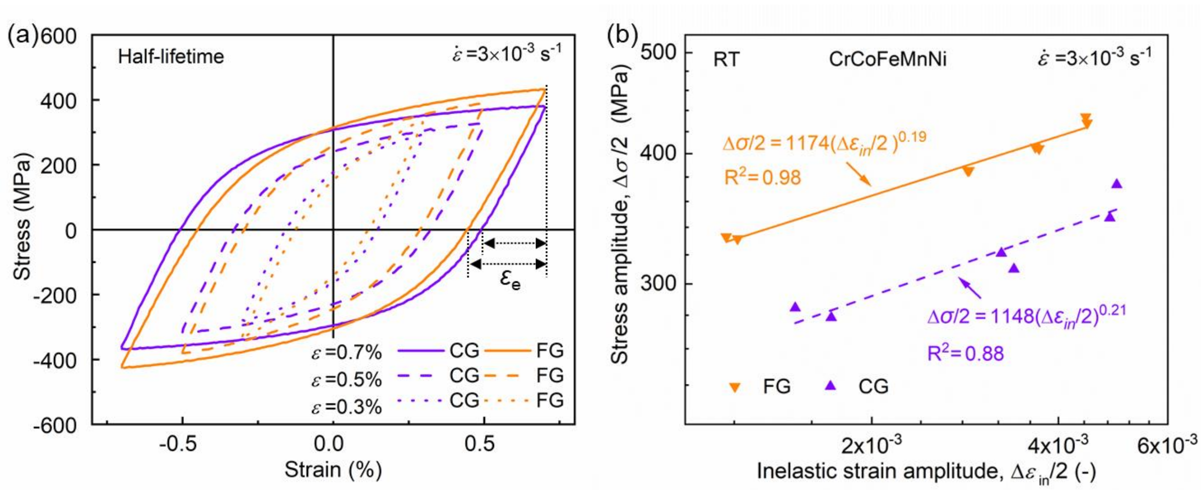

Fig. 4.3: (a) Typical hysteresis loops at half-life, and (b) the stress amplitude ($\Delta\sigma/2$) *versus* inelastic strain amplitude ($\Delta\varepsilon_{in}/2$) plots of FG and CG CoCrFeMnNi at RT [86]. FG CoCrFeMnNi shows higher cyclic strength and lower induced inelastic strain than CG versions.

The cyclic stress-strain response can be visualized by plotting the saturated stress amplitude $\Delta\sigma/2$ against the inelastic strain amplitude $\Delta\varepsilon_{in}/2$, both acquired at half-life, see Fig. 4.3b. This relation could be expressed by a power-type relation [87]:

$$\Delta\sigma/2 = K'(\Delta\varepsilon_{\mathrm{in}}/2)^{n'} \qquad \text{Eq. 2}$$

Here, K' is the cyclic strength coefficient and n' is the cyclic work hardening exponent. The corresponding fitted curves/parameters for both grain sizes at half-life are plotted in Fig. 4.3b. The fitted parameters are also given in Table 4.1.

Clearly, the slope of the curves (or n' values) of both FG and CG CoCrFeMnNi are comparable (0.19 *versus* 0.21, respectively). This indicates their similar cyclic hardening rates with respect to strain amplitude. As suggested in Refs. [88, 89], the noticeable difference in n' value of different FCC alloys could reflect their different slip modes. Therefore, their similar n' values imply that they likely show similar slip mode of dislocations. This behavior will be confirmed by later TEM investigations, see Section 4.4.1.4.

Table 4.1: Values of the parameters obtained by fitting the LCF data from Eq. 2 for fine-grained (FG) and coarse-grained (CG) CoCrFeMnNi at RT

Material	Cyclic strength coefficient, K' (MPa)	Cyclic strain hardening exponent, n'
FG	1174	0.19
CG	1148	0.21

4.2.1.2 *Low-cycle fatigue life*

Fig. 4.4a shows the saturated stress amplitude ($\Delta\sigma/2$) *versus* the lifetime (N_f) plot (*i.e.*, Wöhler curve) for both FG and CG CoCrFeMnNi. Evidently, at similar $\Delta\sigma/2$, the FG material exhibits a longer lifetime than the CG material, indicating a better cyclic stress resistance with grain refinement. Fig. 4.4b presents $\Delta\varepsilon_t/2$ *versus* $2N_f$ plot. Though experimental scatter convolutes the comparison, the FG material's higher fatigue life is still apparent for a given total strain amplitude when compared to the CG counterpart (Fig. 4.4b).

In Fig. 4.4c, the saturated inelastic strain amplitude ($\Delta\varepsilon_{in}/2$) *versus* $2N_f$ plots for both grain sizes are shown. The data for both versions are lying almost on top of each other. The plots are fitted by the known Manson-Coffin equation [90, 91]:

$$\Delta\varepsilon_{\mathrm{in}}/2 = \varepsilon'_{\mathrm{f}}\,(2N_{\mathrm{f}})^{c} \qquad \text{Eq. 3}$$

Here $\varepsilon'_{\mathrm{f}}$ is the fatigue ductility coefficient and c is the fatigue ductility exponent. The fitted parameters are also listed in Fig. 4.4c and Table 4.2. Similar fitted curves/parameters (*e.g.*, c values: −0.53 *versus* −0.49) suggest that the Manson-Coffin relation is independent of the grain size within the investigated micrometer range.

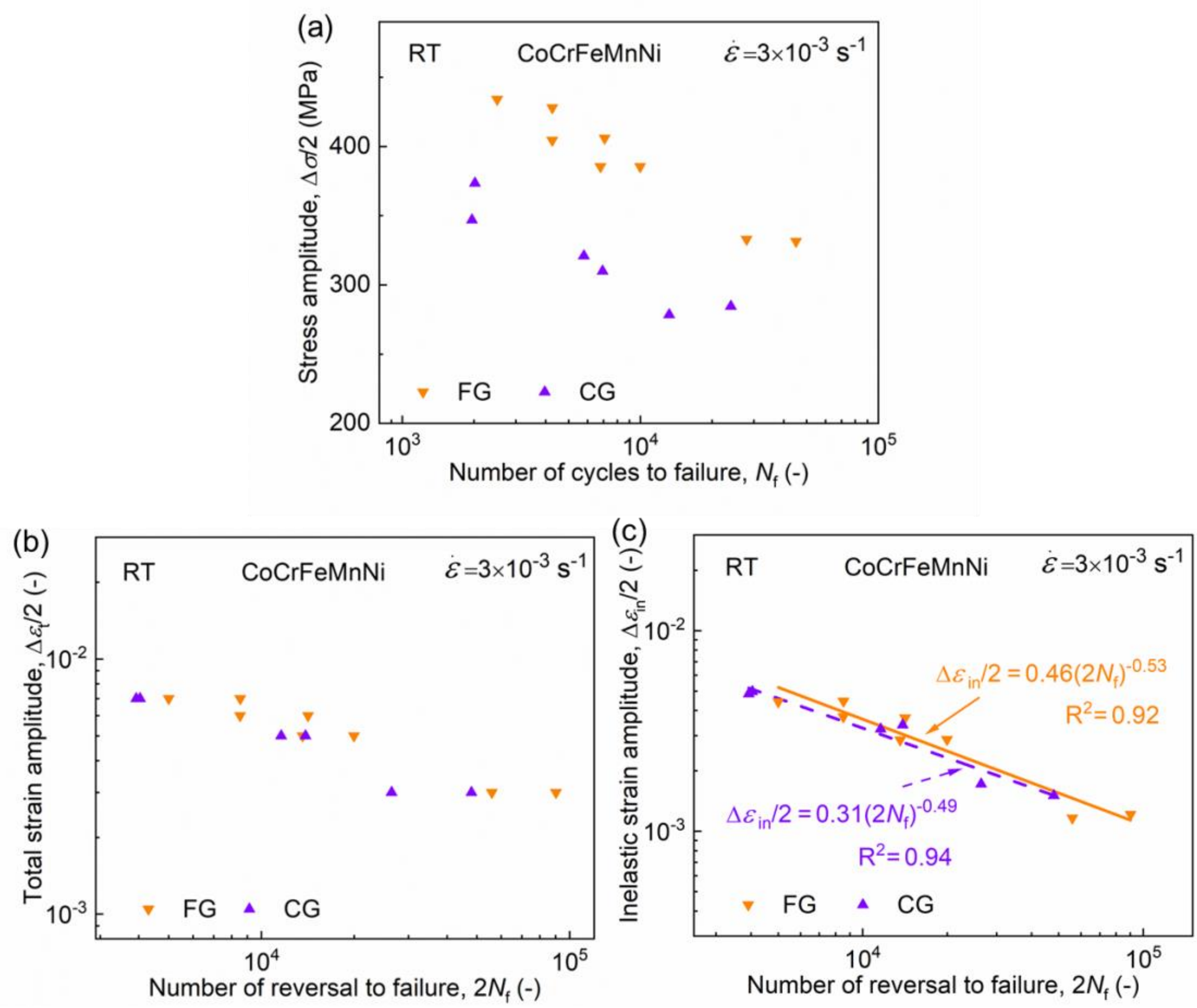

Fig. 4.4: Plots of (a) saturated stress amplitude ($\Delta\sigma/2$) *versus* the number of cycles to failure (N_f), (b-c) total and inelastic strain amplitude ($\Delta\varepsilon_t/2$ and $\Delta\varepsilon_{in}/2$) *versus* $2N_f$, respectively, for FG and CG CoCrFeMnNi at RT [86]. Notably, though (a) Wöhler curves are usually plotted in stress-controlled fatigue tests, they were shown here and later to reveal the relation between saturated stress amplitude and lifetime.

Table 4.2: Values of the parameters obtained by fitting the LCF data from Eq. 3 for fine-grained (FG) and coarse-grained (CG) CoCrFeMnNi at RT

	Fatigue ductility coefficient, ε'_f	Fatigue ductility exponent, c
FG	0.46	-0.53
CG	0.31	-0.49

4.2.2 Low-cycle fatigue response at 550 °C

4.2.2.1 Cyclic stress response

The cyclic stress response curves (*i.e.*, tensile peak stress *versus* the number of cycles) of the FG CoCrFeMnNi at 550 °C are shown in Fig. 4.5a. Generally, the material's cyclic stress response can be divided into two distinct stages before failure:

Stage 1: Exemplifies rapid cyclic hardening with a rise in the tensile peak stresses for about the first 20 to 120 cycles ($N/N_f < 0.05$) depending on the applied strain amplitude (see Fig. 4.5a). As obvious from Fig. 4.5a, apart from the observed minor (or almost no) initial hardening under strain amplitudes below 0.4% (*i.e.*, 0.2% and 0.3%), the rate and the amount of cyclic hardening increase with the increase in applied strain amplitude. This initial hardening was determined to be 30 MPa and 55 MPa for 0.4% and 0.5% strain amplitudes, respectively. However, for strain amplitudes of 0.75% and 0.8% the hardening is estimated to be about 90 MPa, indicating an onset of saturation in hardening.

Stage 2: Represents quasi-stable cyclic response (Fig. 4.5a) with almost no pronounced change in the peak stresses. This stage occupies the majority of the cyclic lifetime ($0.05 < N/N_f < 0.95$).

In addition, the above cyclic stress response is also consistent with the variation in the inelastic strain. As seen in Fig. 4.5b, the inelastic strain amplitude initially decreases followed by a near-steady state, confirming an initial cyclic hardening followed by near-steady state.

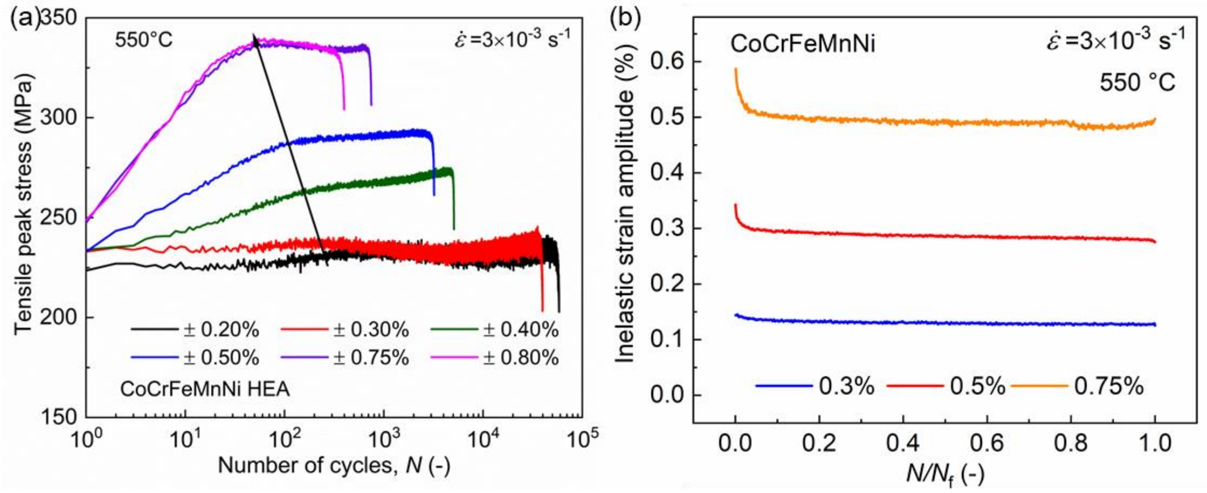

Fig. 4.5: (a) Tensile peak stress *versus* the number of cycles (N) [62] and (b) inelastic strain amplitude *versus* the normalized number of cycle (N/N_f), curves for FG CoCrFeMnNi tested at 550 °C and various strain amplitudes. For the sake of brevity, the curves of other strain amplitudes (0.2%, 0.4% and 0.8%) are not shown in (b).

Another interesting phenomenon at 550 °C is the discontinuity in plastic flow stress, called serrated flow, which can be observed from the hysteresis loops (Fig. 4.6a-b). As shown in Fig. 4.6, the serrated flow occurred in both tensile and compression branches of the loading regime. Moreover, the serration magnitude or amplitude appears to decrease progressively with the number of cycles (see Fig. 4.6). For example, the serration amplitude decreased continuously from ~ 10 MPa initially to almost zero under 0.75% strain amplitude.

In comparison to that at RT, the difference of cyclic stress response between RT and 550 °C can be noticed. The main differences lie in the absence of cyclic softening (Fig. 4.5a) and the presence of serrated plastic flow (Fig. 4.6) at 550 °C.

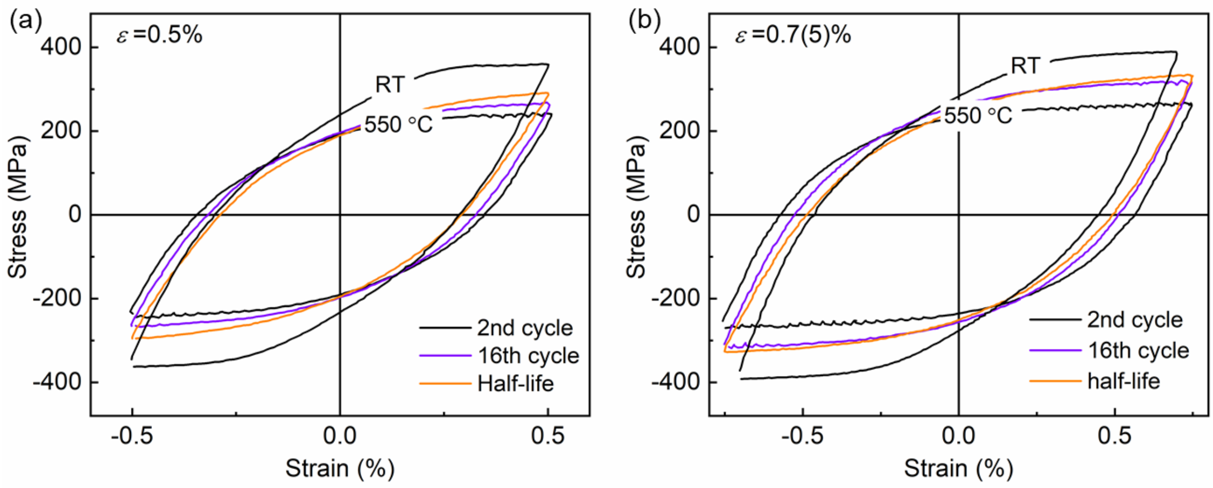

Fig. 4.6: Hysteresis loops of several cycles at strain amplitude of (a) 0.5% and (b) 0.7(5)%, for FG CoCrFeMnNi tested at 550 °C [92]. For comparison, the hysteresis loops at RT and 2nd cycle are also included showing no serrated flow at RT [92].

To understand the cyclic stress-strain response, the saturated stress amplitude ($\Delta\sigma/2$) *versus* inelastic strain amplitude ($\Delta\varepsilon_{in}/2$) plots at 550 °C are shown in Fig. 4.7. As evident, the data points exhibit a linear trend, which can be fitted by Eq. 2. The fitted values of parameters (K' and n') are shown in Fig. 4.7 and Table 4.3, which also include the results at RT for comparison. Clearly, the slope of each curve (*i.e.*, n' value) at 550 °C (0.14) is lower than that at RT (0.19), suggesting different cyclic hardening rates with respect to strain amplitude. As different n' values indicate different slip modes of dislocations [22], different slip modes at different temperatures could be anticipated and will be confirmed by TEM investigations (see Section 4.5.2.1).

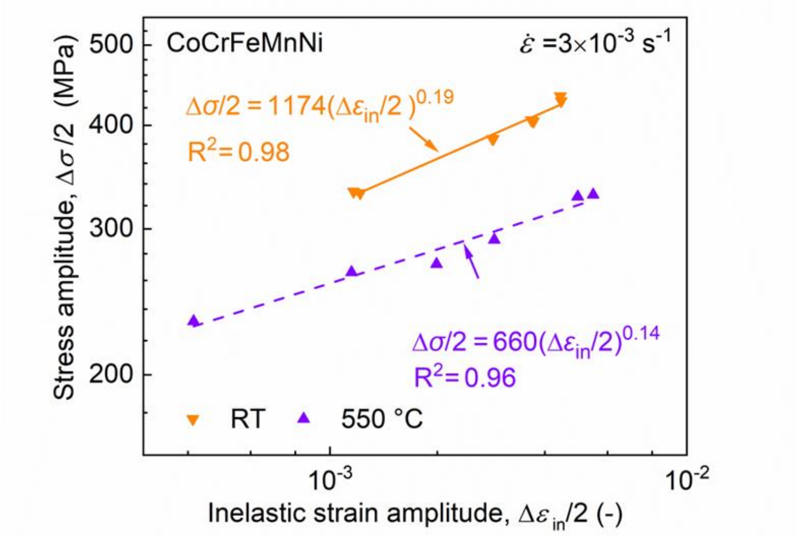

Fig. 4.7: Comparison of cyclic stress-strain response for FG CoCrFeMnNi tested at RT and 550 °C [92].

Table 4.3: Values of the parameters obtained by fitting the LCF data from Eq. 2 for FG CoCrFeMnNi at 550 °C and RT

Temperature	Cyclic strain hardening coefficient, K' (MPa)	Cyclic strain exponent, n'
550 °C	660	0.14
RT	1174	0.19

4.2.2.2 *Low-cycle fatigue life*

The Manson-Coffin curve (*i.e.*, $\Delta\varepsilon_{in}/2$ versus $2N_f$) of the CoCrFeMnNi at 550 °C is shown in Fig. 4.8a. Evidently, fatigue life decreases with an increase in applied strain amplitude. Besides, the fatigue life of CoCrFeMnNi can be accurately predicted by using the Manson-Coffin model. The values of LCF parameters (*i.e.*, ε'_f and c) determined from the linear fit (Eq. 3) of the experimental data are listed in Table 4.4.

For comparison, the corresponding curves at RT are also given in Fig. 4.8a. Upon comparison to that at RT, the lifetime is shorter at 550 °C under similar strain conditions

(Fig. 4.8a). The shorter lifetime at 550 °C also holds for similar stress conditions (seeFig. 4.8b).

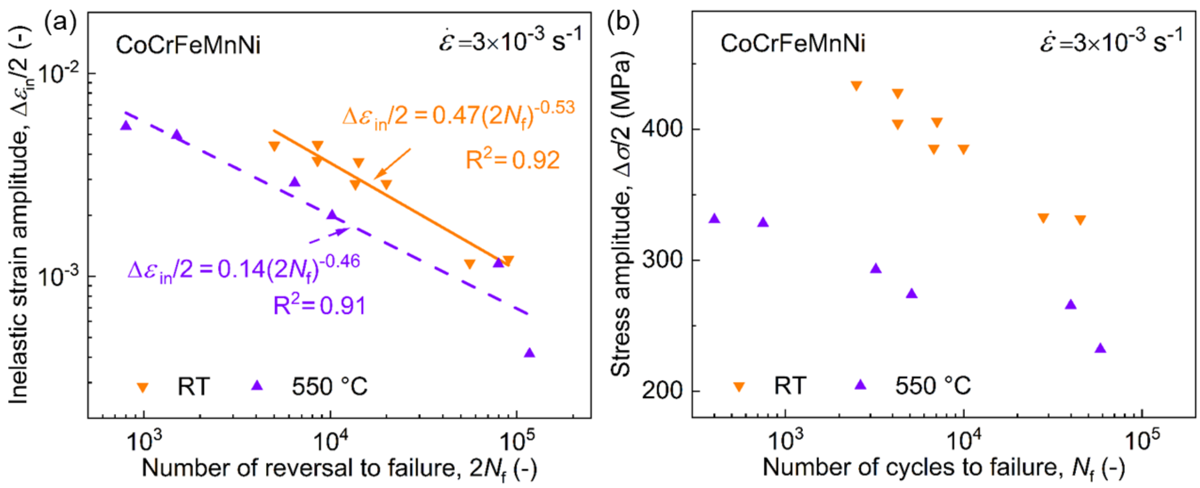

Fig. 4.8: Plot of (a) inelastic strain amplitude ($\Delta\varepsilon_{in}/2$) *versus* the number of reversals to failure ($2N_f$), and (b) stress amplitude ($\Delta\sigma/2$) *versus* number of cycles to failure (N_f), of FG CoCrFeMnNi at 550 °C and RT [92]. The fitted Manson-Coffin curves and parameters are also plotted in (a).

Table 4.4: Values of the parameters obtained by fitting the LCF data from Eq. 3 for FG CoCrFeMnNi at 550 °C and RT

Temperature	Fatigue ductility coefficient, ε'_f	Fatigue ductility exponent, *c*
550 °C	0.14	-0.46
RT	0.47	-0.53

4.3 Damage characteristics

To discern damage mechanisms, the cross-section (having microcracks) and fracture surfaces were examined. Firstly, the crack-growth profile of the cross-section from both FG and CG CoCrFeMnNi samples, tested at 0.5% strain amplitude and RT, were scanned via EBSD. Then EBSD data were post-processed into IPF and KAM maps (see Fig. 4.9a-d). Fig. 4.9e shows the schematic position of the investigated crack on the cross-section.

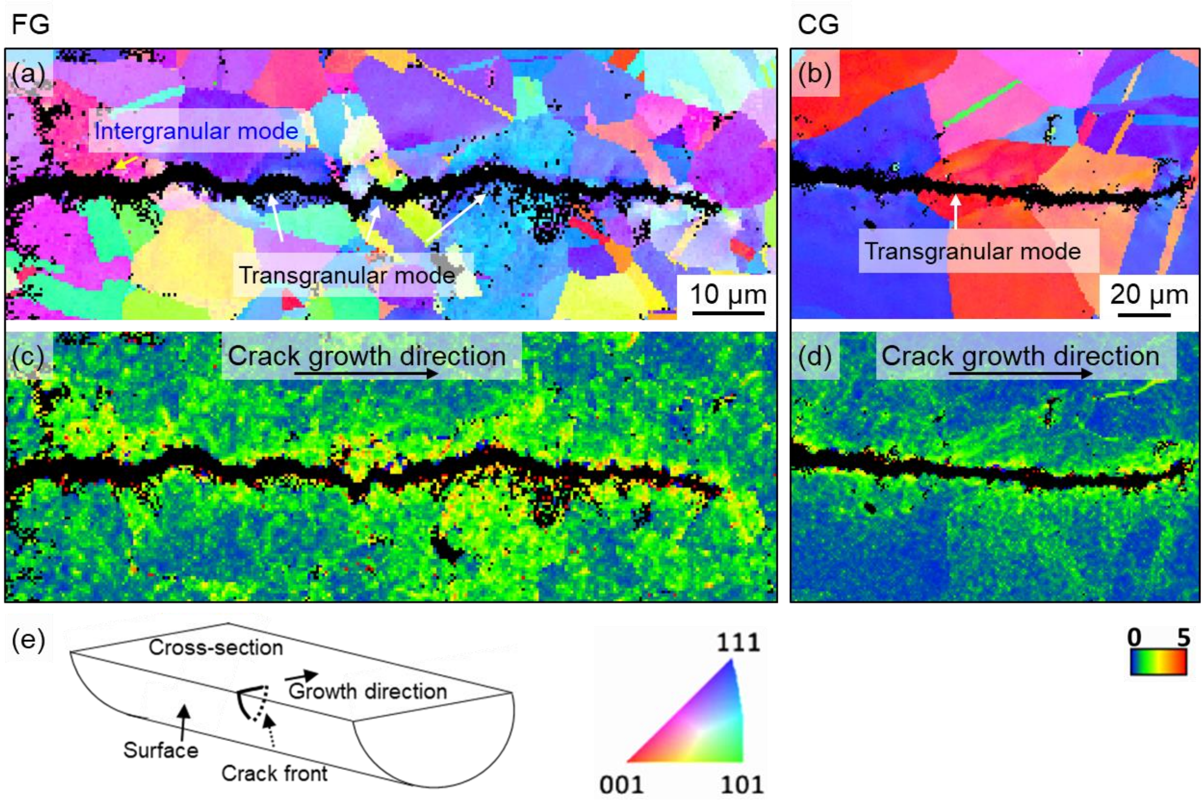

Fig. 4.9: EBSD scans of fatigue crack profiles in (a, c) fine-grained (FG) and (b, d) coarse-grained (CG) CoCrFeMnNi tested at 0.5% strain amplitude. (e) A schematic drawing shows the position of these investigated cracks.

The IPF maps in Fig. 4.9a-b indicate that, for both FG and CG materials, cracks mainly propagate through the grains and occasionally along the GBs. This observation reveals predominant transgranular propagation behavior in CoCrFeMnNi. The corresponding KAM maps in Fig. 4.9c-d show larger KAM values in the grains close to the crack flanks. This larger KAM reflects a significant amount of plastic deformation (accommodated by GNDs) emitted from the crack tip upon cyclic loading. Additionally, deformation-twins were not observed near the crack tip by EBSD for both FG and CG samples. Generally, the above findings (such as predominantly transgranular crack propagation) are in line with the observation from previous fatigue crack propagation tests [22].

Fig. 4.10 presents typical fracture surfaces of (a-c) FG and (d-f) CG samples tested at 0.5% strain amplitude and RT. The overview of fracture surfaces for both samples exhibits similar damage characteristics. Generally, fatigue cracks initiated at the sample surfaces (see Fig. 4.10a-b and Fig. 4.10d-e). In the crack growth region, both

FG and CG samples manifest mainly classical fine-scale transgranular ductile features, namely striations (see Fig. 4.10c, f). The striations are known to be formed during repeated crack blunting and re-sharpening due to cyclic plasticity during crack propagation [16]. Moreover, the average striation spacing increased with the increase in both strain amplitude and the distance from the initiation site (not shown here), indicating an increase in crack growth rate.

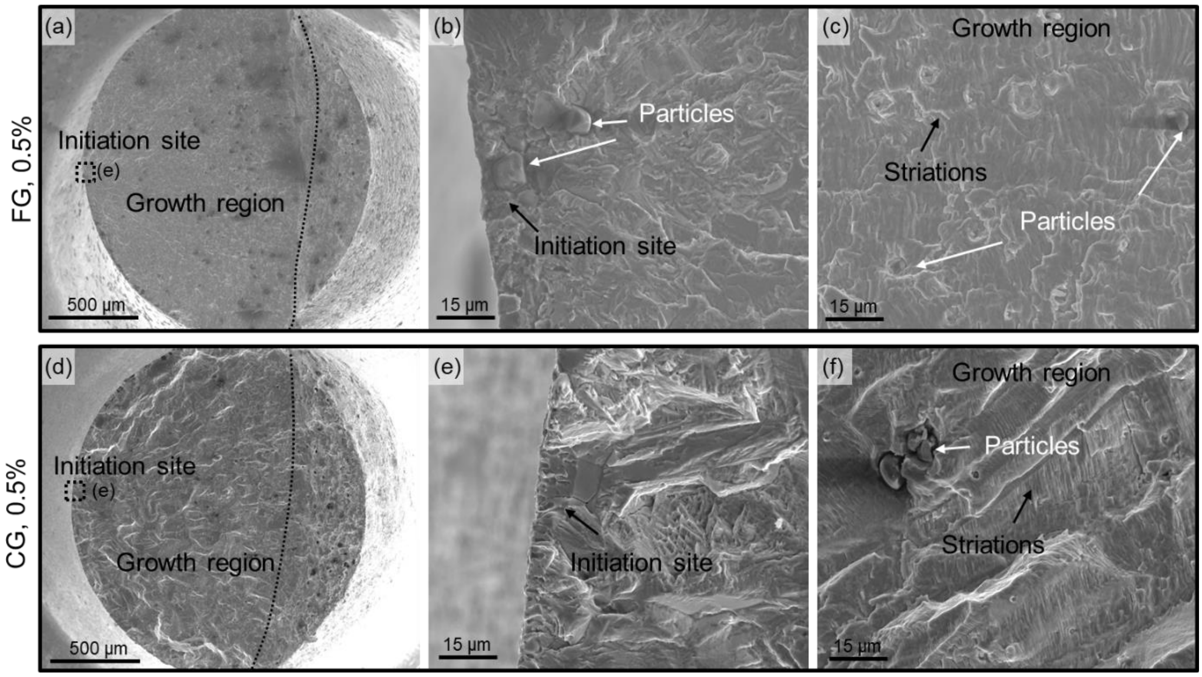

Fig. 4.10: SEM micrographs revealing fracture surface morphologies of (a-c) fine-grained (FG) and (d-f) coarse-grained (CG) CoCrFeMnNi tested under 0.5% strain amplitudes at RT.

Furthermore, micro-particles are observed on the fracture surface of both FG and CG materials (see Fig. 4.10b-c, f). These particles are proved to be Cr-enriched oxides (*e.g.*, see later Fig. 4.11c), which formed during material processing [62]. Notably, the particles lying in surface grains acted as stress raisers and hence crack initiation sites (see Fig. 4.10b), leading to earlier failure. This could cause the observed scatter in the lifetime (Fig. 4.4). Therefore, by improving processing strategies that eliminate impurities such as Cr-O oxides, fatigue properties of MPEAs can be enhanced.

Fig. 4.11 displays a typical fracture surface for FG CoCrFeMnNi tested at 550 °C. Similar to that at RT, the fracture tomography at 550 °C exhibits crack initiation from the surface (Fig. 4.11a) and transgranular crack growth (including striation features Fig.

4.11b). Furthermore, micro-particles were also detected herein and identified to be Cr-O enriched (see EDS elemental maps in Fig. 4.11c). In addition, the oxide layer was also found on both the sample surface and fracture surface (*e.g.*, see Fig. 4.11d).

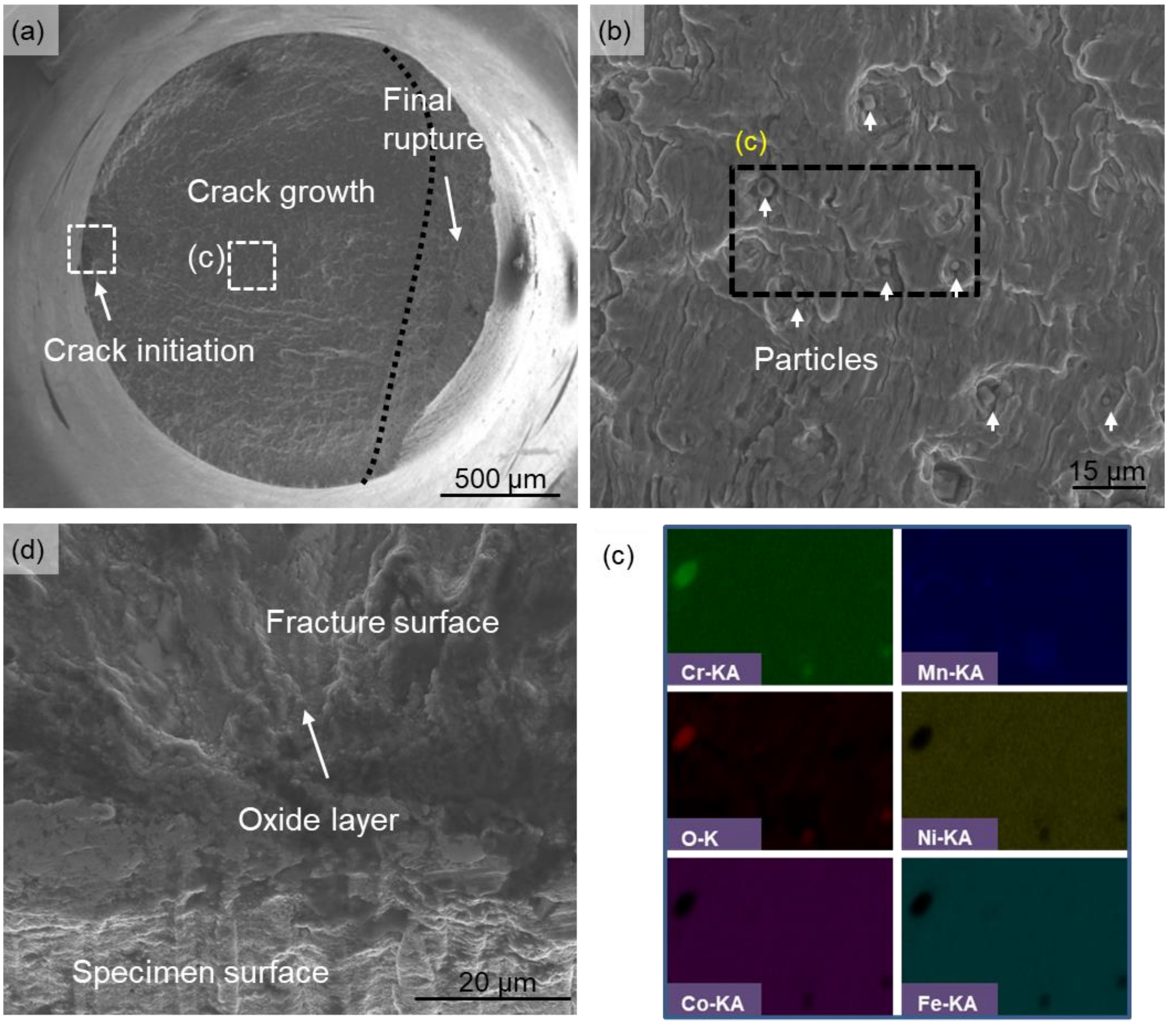

Fig. 4.11: SEM micrographs on fracture surface of a fine-grained CoCrFeMnNi sample tested at 550 °C under 0.3% strain amplitude [62].

4.4 Microstructure after cyclic loading

To understand the operating deformation mechanisms, the post-fatigued microstructures of CoCrFeMnNi tested at both RT and 550 °C were characterized via EBSD and TEM.

4.4.1 Microstructural evolution at RT

At RT, EBSD investigations for both post-fatigued FG and CG materials show no significant change in texture, average grain size, and twin fraction (see IPF figures in Fig. 4.12a-b) in comparison to the annealed state (Fig. 4.1a-b).

Fig. 4.12c-d present the corresponding KAM maps. Upon comparison to the values of the as-recrystallized specimen (Fig. 4.1), higher KAM values were achieved after cycling, suggesting higher GND density. This can also be seen from the KAM distribution plots in Fig. 4.12e. In addition, KAM distributions of FG and CG CoCrFeMnNi seem to be comparable, which is indicated by the similar green-color distributions in Fig. 4.12c-d and overlapped curves in Fig. 4.12e. This suggests their similar GND density and distribution.

In addition to these EBSD investigations, TEM investigations could provide high-resolution information on the accumulation and distribution of plastic deformation for both materials, such as distinct dislocation configurations and occasional deformation twinning. In the following sections, TEM results are shown to reveal the typical RT-fatigued microstructures for both FG CoCrFeMnNi (in Sections 4.4.1.1, 4.4.1.2, and 4.4.1.3 for strain amplitude of 0.3%, 0.5% and 0.7%, respectively) and CG CoCrFeMnNi (in Section 4.4.1.4).

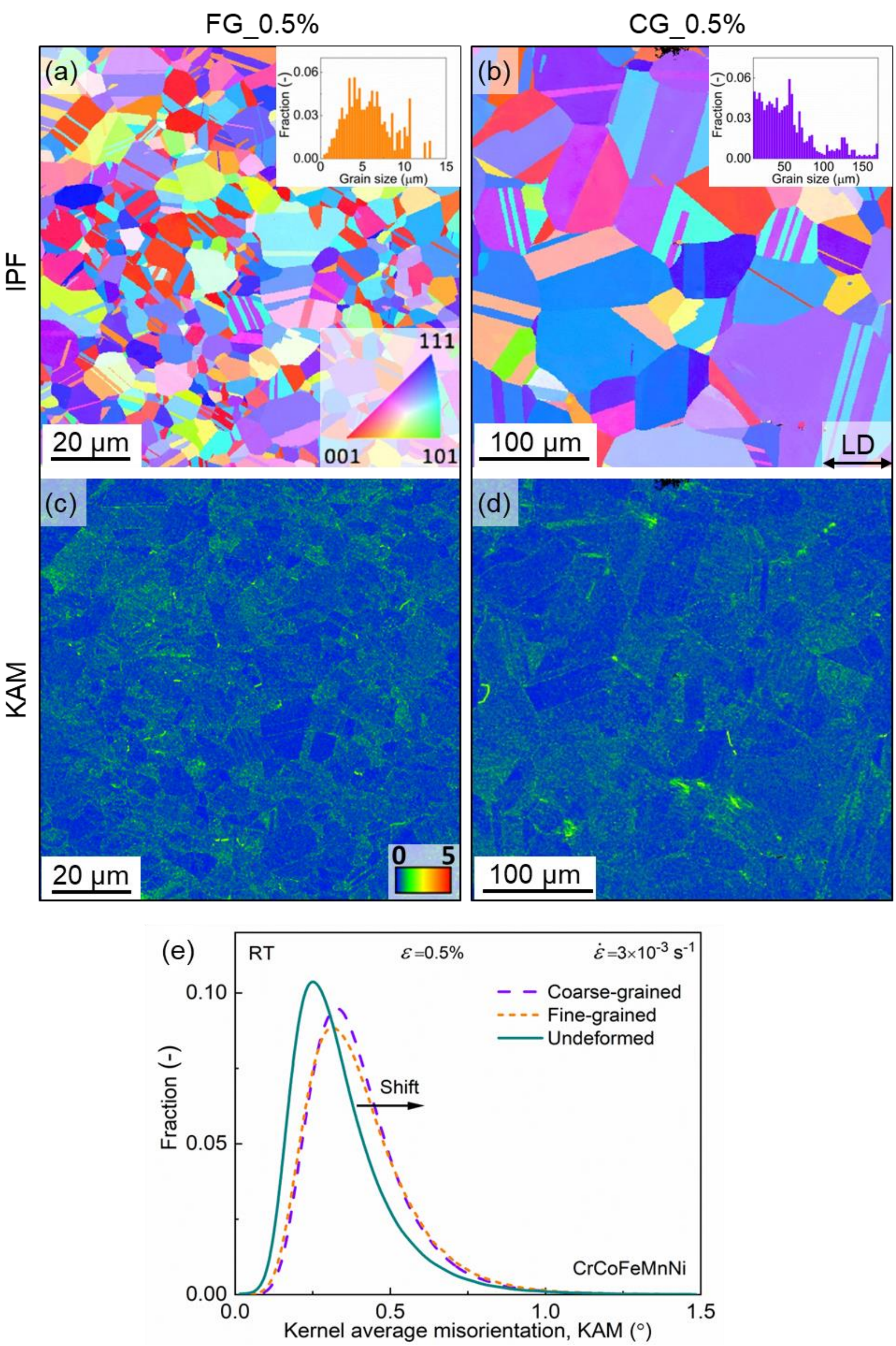

Fig. 4.12: Representative IPF and corresponding KAM maps for (a, c) fine-grained (FG) and (b, d) coarse-grained (CG) CoCrFeMnNi tested at 0.5% strain amplitude at RT. The grain size distributions of each state were provided in the inset of (a, b) [86]. The color

keys in the left column are also valid for the right. (e) shows the KAM distribution at different conditions.

4.4.1.1 Microstructure upon cycling at 0.3% strain amplitude

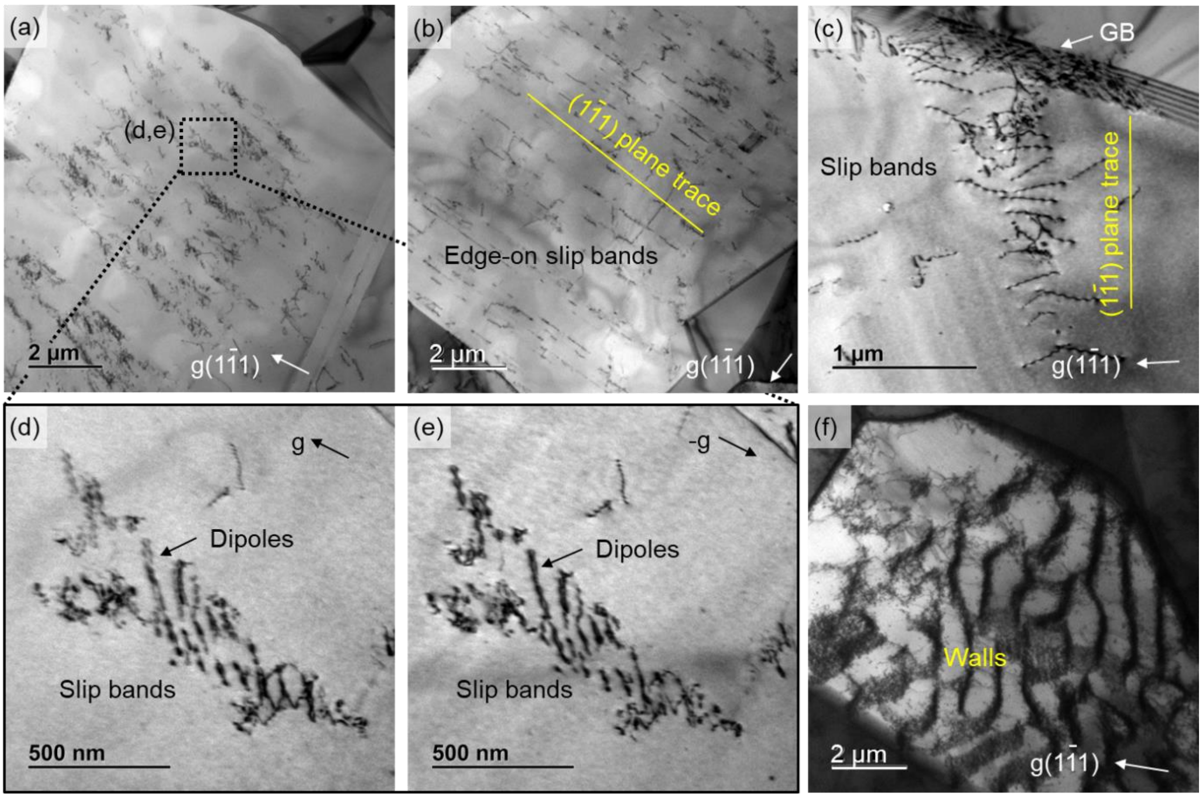

Fig. 4.13: BF-TEM micrographs revealing dislocation structures in FG CoCrFeMnNi tested at 0.3% strain amplitude until failure [86]. Planar SBs are the main observed microstructural features. (a-e) Planar SBs consisting of dislocations with (c) the same Burgers vector, and (d-e) a pair of opposite Burgers vectors. (f) Dislocation wall structure.

Fig. 4.13 presents BF-TEM micrographs of the post-fatigued FG samples tested at 0.3% strain amplitude until failure. Here, planar slip bands (SBs) are recognized to be the main deformation-induced microstructural features (Fig. 4.13a-e). As evident in Fig. 4.13a-c, high dislocation density is observed. The dislocations are arranged on {111} planes inside bands, surrounded by apparently dislocation-free regions. In some SBs, dislocations are proven to be dipoles having +***b***/-***b*** Burgers vectors (see Fig. 4.13a, and enlarged micrographs in Fig. 4.13d-e). The dipole character of the dislocation pairs was confirmed by performing tilting experiments using +***g***/-***g*** diffraction conditions according to [83-85]. Apart from these planar SBs, dislocation walls are occasionally observed (Fig. 4.13f).

4.4.1.2 *Microstructure evolution upon cycling at 0.5% strain amplitude*

Fig. 4.14 presents BF-TEM micrographs of an FG sample tested at 0.5% strain amplitude until failure. In general, due to the higher induced inelastic strain than at 0.3% strain amplitude, significantly higher density of dislocations is observed herein. Furthermore, the planar dislocation arrangements (SBs) became less frequent; by contrast, well-developed dislocation substructures, such as parallel walls, irregular veins, and cells, became more prevalent (Fig. 4.14a-c).

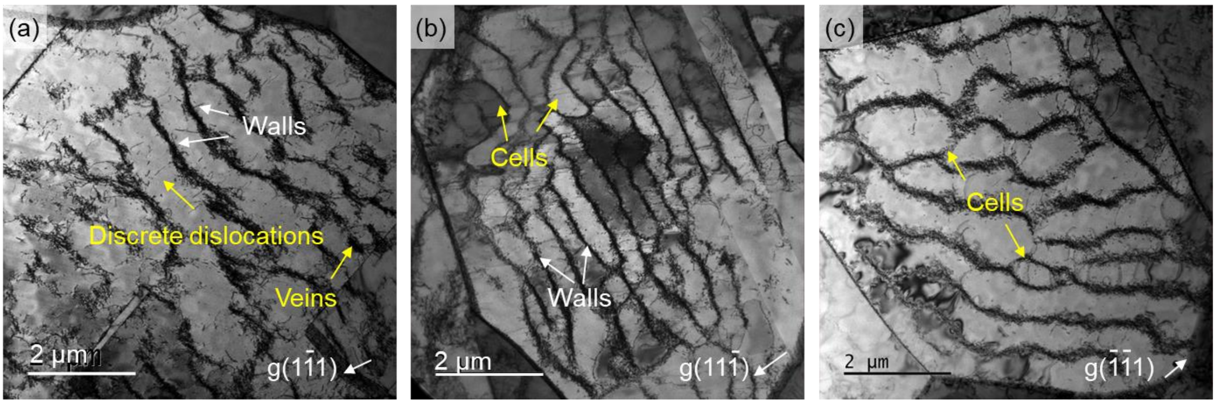

Fig. 4.14: BF-TEM micrographs revealing dislocation structures in FG CoCrFeMnNi tested at 0.5% strain amplitude until failure [86]. Well-defined dislocation substructures, such as parallel walls, irregular veins and cells are prevalent. (a) Wall and vein structures. (b) Wall and cell structures. (c) Cell structures.

To establish how these dislocation structures evolved at different cyclic stages, the interrupted samples (up to 20 and 500 cycles, respectively) were investigated by TEM. The 20th and 500th cycles were chosen, as they correspond to cyclic hardening and softening stages, respectively (see Fig. 4.15).

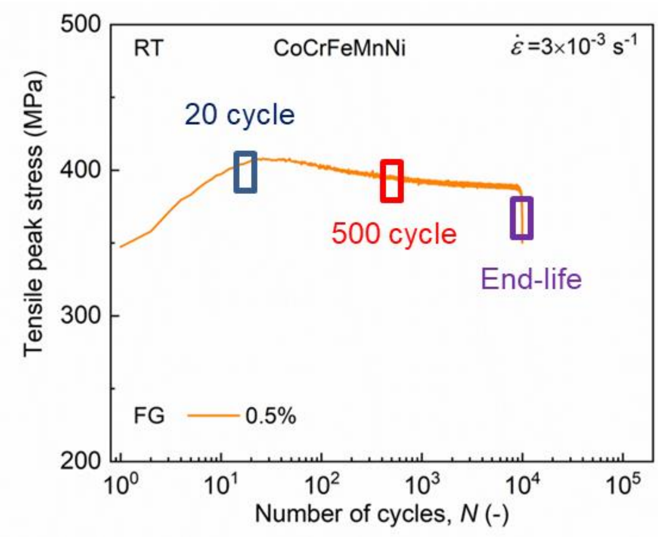

Fig. 4.15: A schematic for the number of cycles for the interrupted (*i.e.*, up to 20 and 500 cycles, respectively) specimens for TEM investigations. The 20th and 500th cycles correspond to cyclic hardening and softening stages, respectively.

Fig. 4.16 shows TEM micrographs of an FG specimen fatigued up to 20 cycles. As evident, dislocations are mainly arranged in the form of tangles (Fig. 4.16a-b) and planar SBs (Fig. 4.16c-f). In the tangles, different dislocations are found to have different ***b*** by using several different two-beam diffraction conditions. For instance, from ***g***·***b*** invisibility analysis, the white-arrow marked dislocations in Fig. 4.16a-b have ***b*** of ½$[0\bar{1}1]$, while others, such as black-arrow marked ones, have other ***b*** (than ½$[0\bar{1}1]$), suggesting multiple slip systems activation.

In addition, the planar SBs are found to consist of arrays of dislocations with ***b*** ½$[0\bar{1}1]$ on the primary slip system (see dislocations indicated by white arrows in Fig. 4.16c). Additionally, the dislocations indicated by black arrows in Fig. 4.16c have the same ***b*** ½$[0\bar{1}1]$. Since the parts of these dislocations (black arrows in Fig. 4.16c) are approximately parallel to the direction of ***b*** (see the yellow arrow), these portions are of screw nature, which is an indication of cross slip. In other planar SBs, dislocations are found to be dipole pairs (Fig. 4.16d-e).

Lastly, partial dislocations with bounding stacking fault (SF) are sporadically recognized by the WBDF technique (*e.g.*, see Fig. 4.16f). It is noteworthy that the dislocation substructures (*i.e.*, walls, veins, and cells) were not observed at this hardening stage.

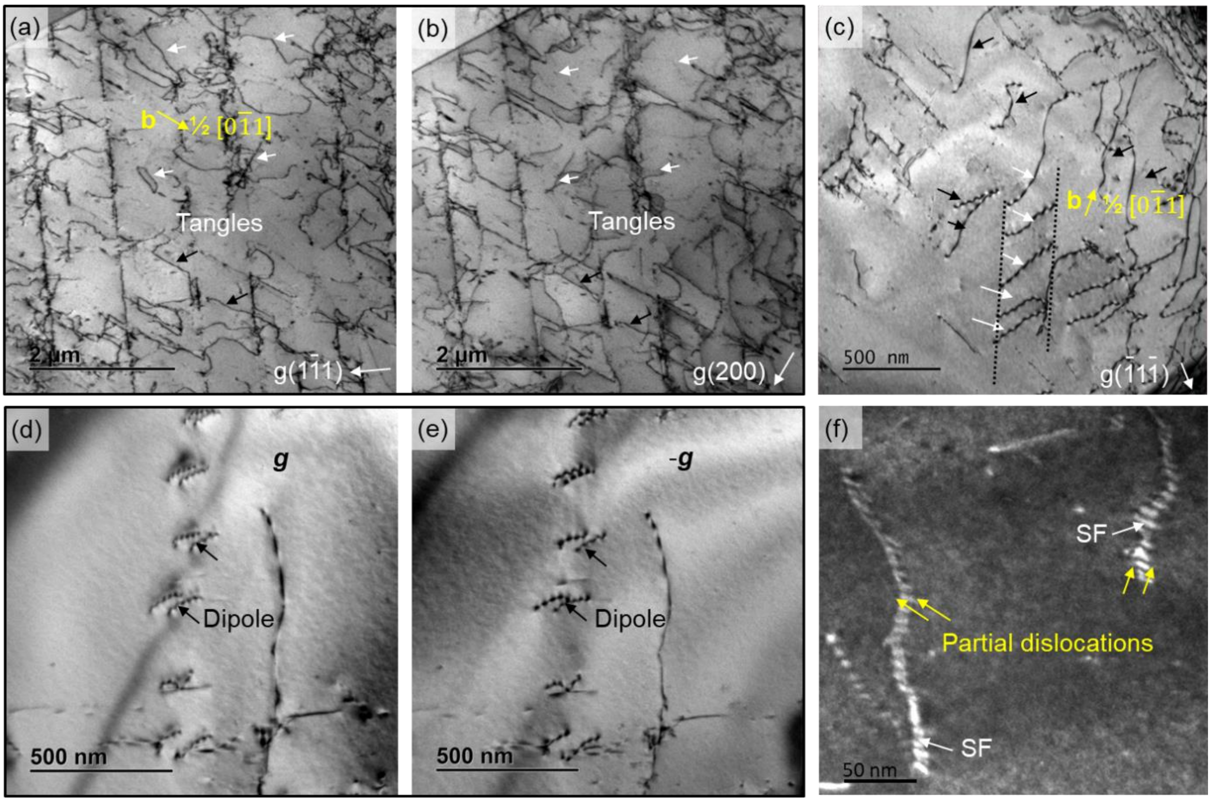

Fig. 4.16: (a-e) BF- and (f) WBDF-TEM micrographs revealing dislocation structures in FG CoCrFeMnNi tested at 0.5% strain amplitude after 20 cycles, representing cyclic hardening [86]. Dislocation tangles and planar slip bands are common features. (a-b) Multiple slip systems activated dislocations and tangles. (c-f) Planar slip bands, consisting of (c) primary dislocations, (d-e) dislocation dipoles, and (f) occasionally partial dislocations with bounding SFs.

Fig. 4.17 presents the microstructure of the FG specimen which was interrupted at 500 cycles. At this stage, dislocations rearranged into substructures, such as veins and walls. Nevertheless, in comparison to the well-defined dislocation substructures observed at the end of the lifetime (Fig. 4.14), these structures are relatively ill-defined (*e.g.*, top right corner of Fig. 4.17a, and right side of Fig. 4.17b). By using ***g·b*** analysis, dislocations in ill-defined walls and veins (*e.g.*, the red-square indicated region) are found to have different ***b*** (see enlarged Fig. 4.17d-f, where walls and veins are simultaneously visible under $1\bar{1}1, \bar{1}11, \bar{2}00$ diffraction conditions), which suggests domination of multiple slip. In-between walls or veins (*i.e.*, in channels), only few single dislocations are observed. These discrete dislocations were identified to be of screw type, such as ½[$0\bar{1}1$] primary dislocations (indicated by white arrows in Fig. 4.17d-f). Besides, partial dislocations along with SFs are still occasionally observed (*e.g.*, see Fig. 4.17c).

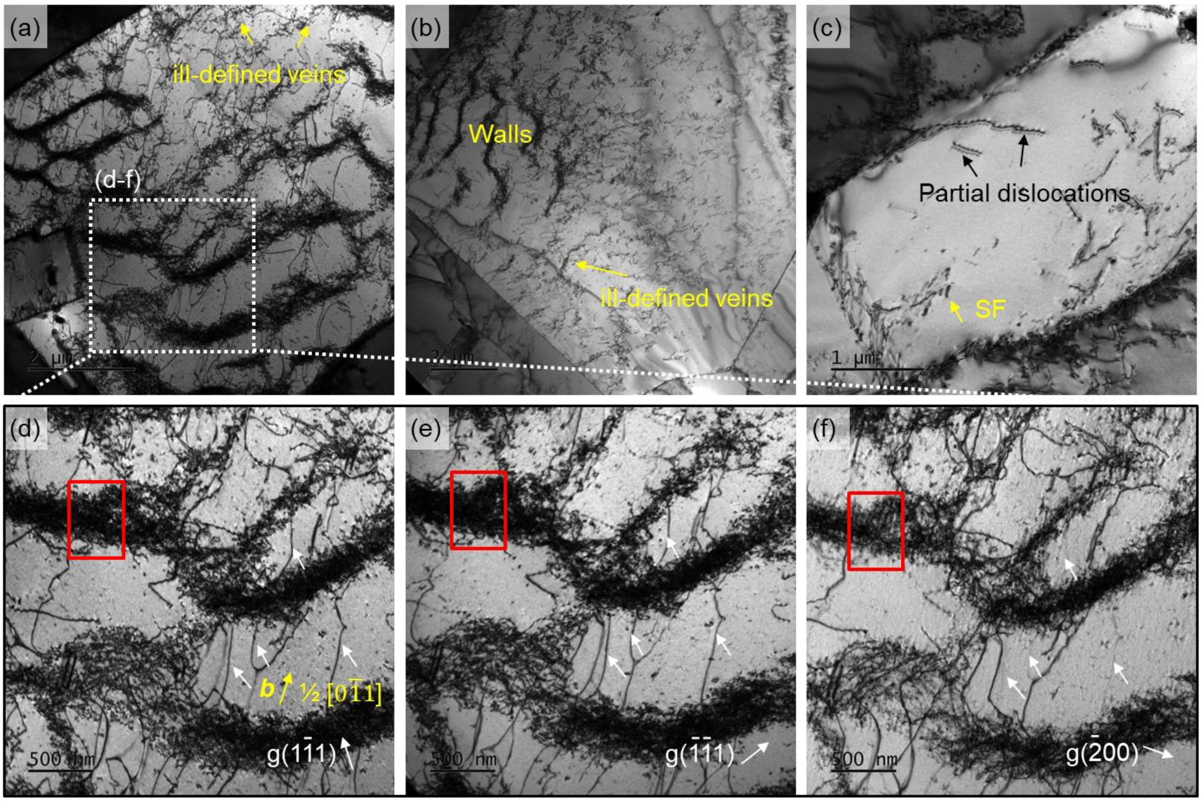

Fig. 4.17: BF-TEM micrographs revealing dislocation structures in FG CoCrFeMnNi tested at 0.5% strain amplitude after 500 cycles representing cyclic softening stage [86]. (a-b) Weak- (or ill-) defined wall and vein substructures. (c) Sporadically observed partial dislocations and SFs. (d-f) Dislocations in the walls (*e.g.*, the red-square indicated region) having different Burgers vectors, and those in the channels having screw character, which are confirmed by micrographs taken at three different two-beam diffraction ***g*** conditions.

4.4.1.3 Microstructure upon cycling at 0.7% strain amplitude

Fig. 4.18 shows typical dislocation structures in post-fatigued FG CoCrFeMnNi tested at 0.7% strain amplitude. Similar to 0.5% strain amplitude, well-developed substructures (including wall, vein, cell and labyrinth structures) are the main microstructural features (Fig. 4.18a-f). However, at 0.7% strain amplitude, these structures appear to be more condensed (indicating an increase in dislocation density), labyrinth and cell structures appear to become more prominent as well.

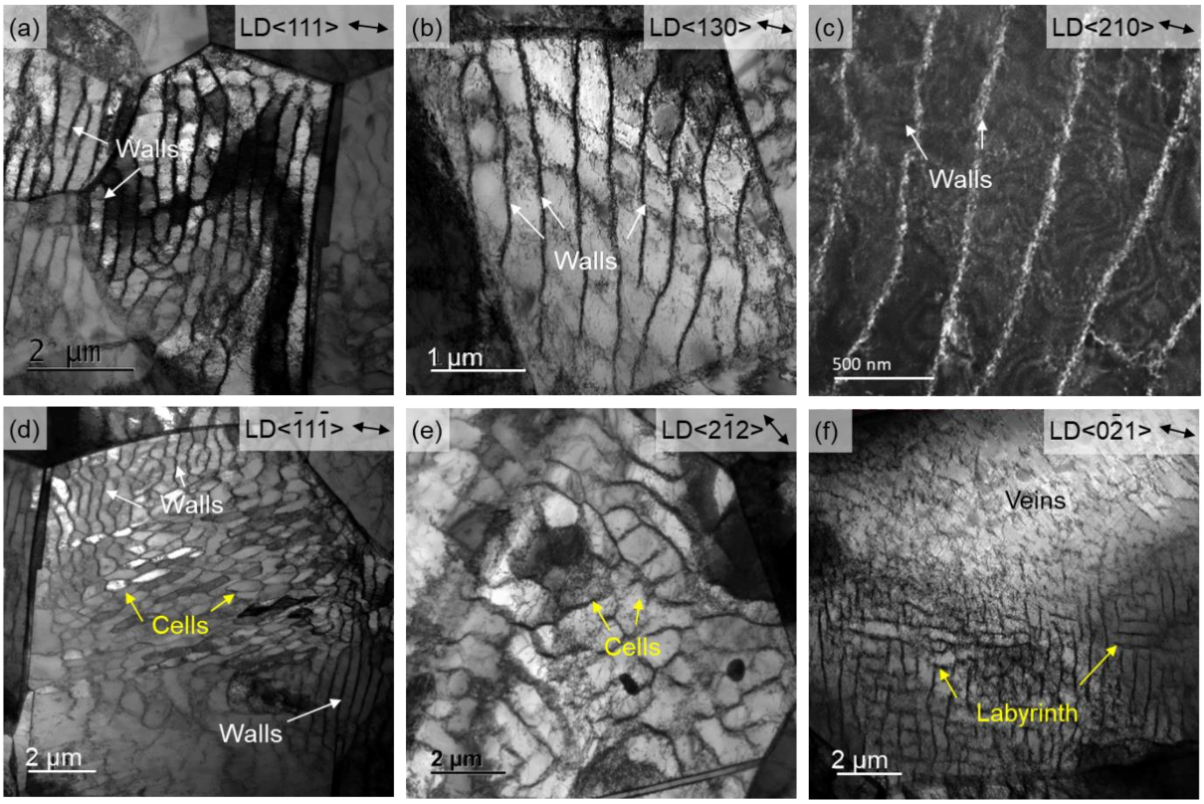

Fig. 4.18: (a-b, d-f) BF- and (c) WBDF-TEM micrographs revealing dislocation structures in FG CoCrFeMnNi tested at 0.7% strain amplitude until failure [86]. Well-developed substructures (*i.e.*, walls, veins, cell and labyrinth) are the main dislocation features. (a-c) Wall structure. (d) Wall and cell structures. (e) Cell structure. (f) Labyrinth and vein structures.

Furthermore, the grain orientation dependence of distinct dislocation substructures was investigated for FG CoCrFeMnNi tested at 0.5% and 0.7% strain amplitudes. Apart from some expected observations (*e.g.*, a similar type of dislocation structures was formed in grains with similar orientations, not shown here), other unexpected results can be summarized as follows:

- In grains with similar orientations, dislocations were rearranged into different substructures. For instance, as in Fig. 4.18a and Fig. 4.18d, dislocations in grains oriented in <111> parallel to the loading direction (// LD) were arranged into wall and cell structures, respectively.

- The same type of dislocation structure was occasionally formed in grains of different orientations. For example, as in Fig. 4.18a-c, the wall structure was observed in grains with the <111>, <120> and <130> directions // LD, respectively.

- In a single grain, various dislocation structures were observed. For instance, walls, veins, and cells coexisted in the same grain (Fig. 4.18d).

Additionally, no preferred orientation for specific dislocation structure formation was noticed for samples tested at low strain amplitude of 0.3%. These results suggest no significant relation between grain orientation and distinct dislocation structure at all investigated strain amplitudes. The reason will be discussed in Section 4.5.1.4.

4.4.1.4 Microstructure upon cycling coarse-grained CoCrFeMnNi

In general, CG material exhibits similar microstructural evolution as FG material. Typical dislocation substructures (*i.e.*, wall, vein, and labyrinth structures) developed in CG CoCrFeMnNi tested at strain amplitude of 0.7% are shown in Fig. 4.19. Besides, ladder-like PSB substructures are also apparent (Fig. 4.19b). Likewise, it is confirmed that dislocations in the PSB-walls also have different ***b***, see Fig. 4.19c-e. Additionally, in CG material, different dislocation structures also formed in a single grain (Fig. 4.19a-b), which is more frequently observed than in FG samples. In such a manner, larger plastic strain can be accommodated in a single grain.

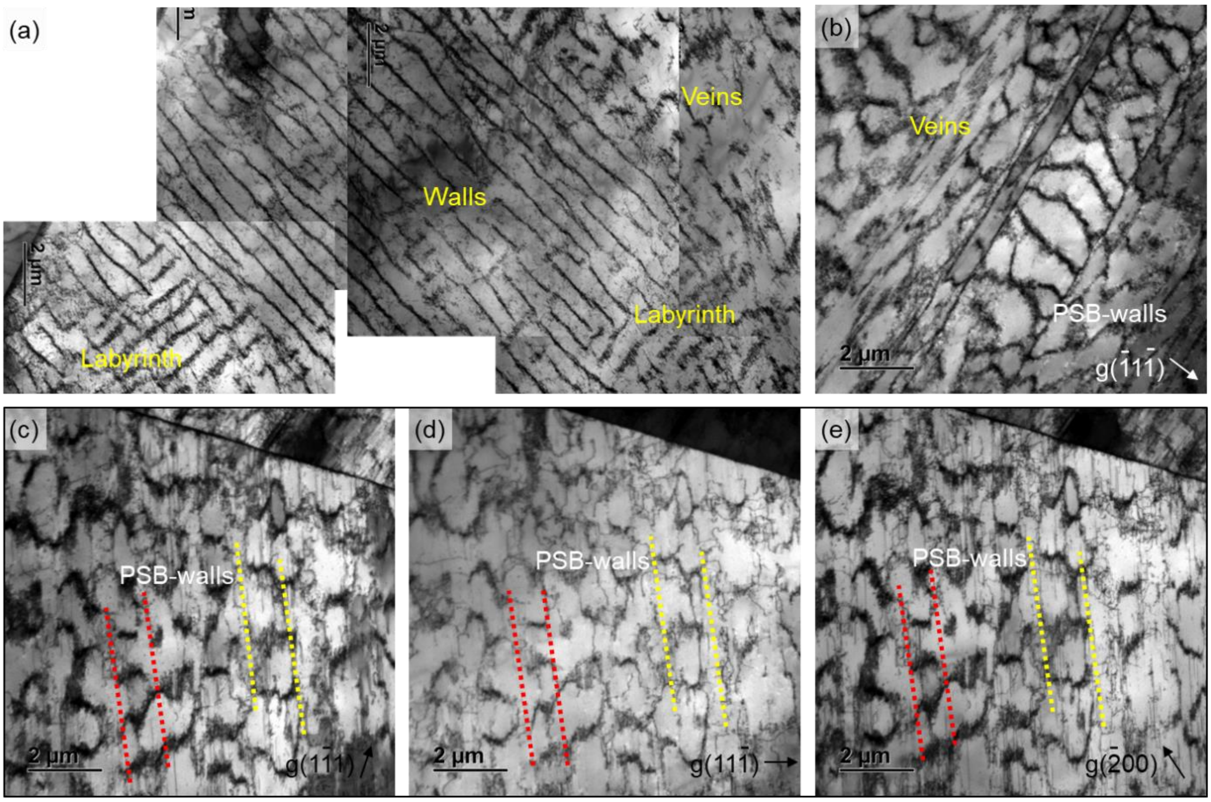

Fig. 4.19: BF-TEM micrographs revealing dislocation structures in CG CoCrFeMnNi tested at 0.7% strain amplitude until failure. (a-b) Various dislocation structures (walls, veins, and labyrinth) formed in a single grain [86]. (b-e) Ladder-like PSB-walls containing dislocations with different Burgers vectors, with (c-e) acquired from different diffraction conditions.

Furthermore, as a peculiar feature of CG CoCrFeMnNi at 0.7% strain amplitude, the deformation twinning (DT) in several near <111> // LD oriented grains was observed, see Fig. 4.20. Since the CG sample tested at 0.7% strain amplitude manifests mainly dislocation substructures (Fig. 4.18) and maintains the trend of the cyclic stress response as other testing conditions (Fig. 4.2), the presence of DT appears to have no significant influence on the mechanical response. Contrary to the above observation for CG material, no DT was observed in FG samples. The reason will be discussed more in Section 4.5.1.3.

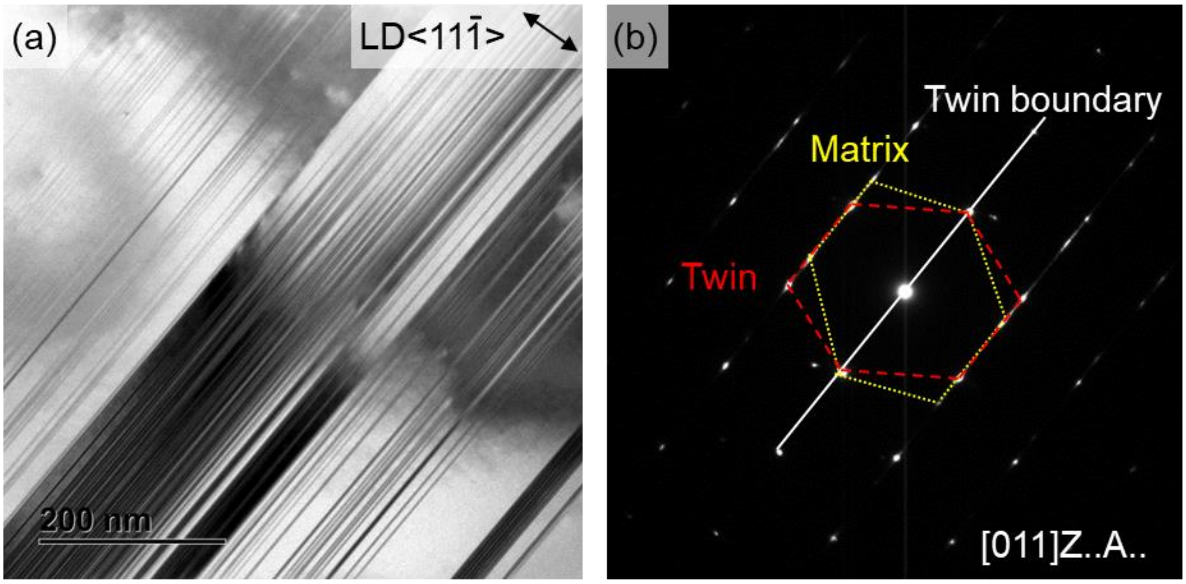

Fig. 4.20: (a) TEM micrograph and corresponding (b) SADP taken along a [011] zone axis, revealing deformation twinning for CG CoCrFeMnNi tested at 0.7% strain amplitude until failure [86].

4.4.2 Microstructural evolution at 550 °C

To understand deformation mechanisms at elevated temperatures, typical IPF and KAM maps (acquired via EBSD) after cyclic straining at 550 °C and 0.5% strain amplitude are shown in Fig. 4.21a-b. Upon comparison with the recrystallized state (Fig. 4.1a), IPF map shows no noticeable change in its texture, grains size and twin fraction after cycling at 550 °C (Fig. 4.21a). This observation is similar to that observed at RT (Fig. 4.12a-b), and also valid for other strain amplitudes (see the average grain size and twin fraction in Table 4.5).

Nevertheless, by comparing to the recrystallized state, KAM value increases after cycling, indicated by more green data points in Fig. 4.21b than in Fig. 4.1c. The KAM values increase further with increasing the applied strain amplitude (see KAM distribution plots at different strain amplitudes in Fig. 4.22). This suggests an increment in the GND density after cycling, which increases further with increasing applied strain amplitude at 550 °C.

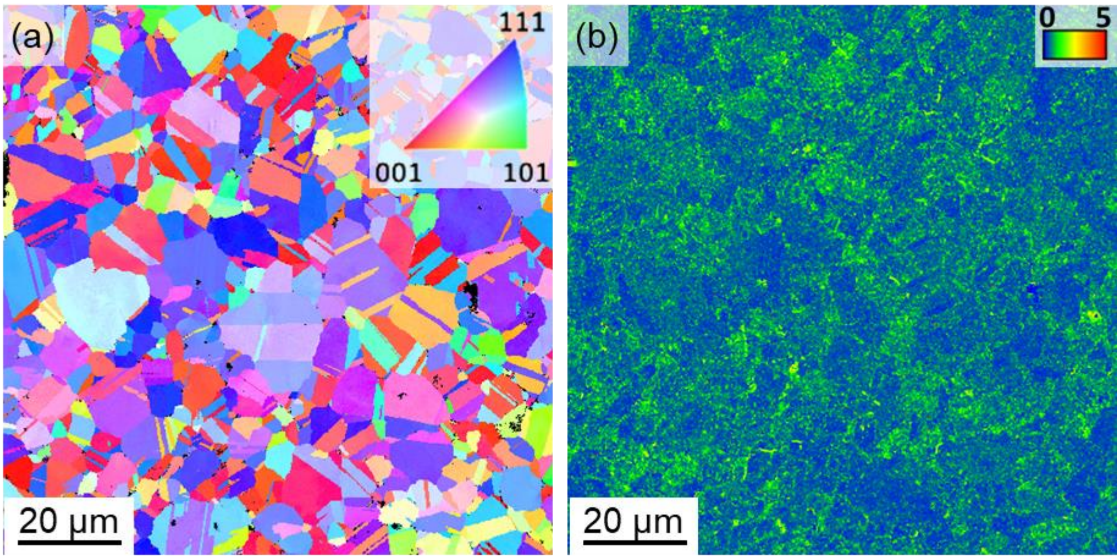

Fig. 4.21: (a) IPF map and (b) KAM map tested at 0.5% strain amplitude and 550 °C [62].

Table 4.5: Average grain size and twin area fraction measured via EBSD after cycling under various strain amplitudes at 550 °C [62]. The data at recrystallized state is also provided for comparison.

Condition	Average grain size (µm)	Twin area fraction
Recrystallized	6.4	35%
0.3%	6.7	34%
0.5%	6.5	34%
0.75%	6.4	36%

By comparing to the KAM tested at RT and the same 0.5% strain amplitude (Fig. 4.12c), the KAM value at 550 °C appears to be higher (see more green data points in Fig. 4.21b). This indicates a higher GNDs density at elevated temperatures than at RT.

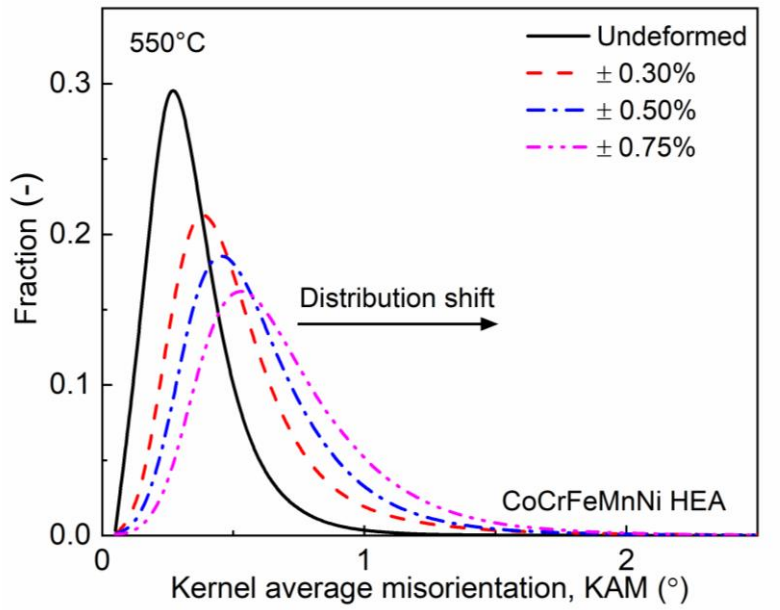

Fig. 4.22: KAM distribution plots obtained by analyzing EBSD scans taken before (as-recrystallized/undeformed) and after cyclic straining under various strain amplitudes at 550 °C [62]. The average KAM values increase upon cycling and further increase with applied strain amplitude.

In order to delineate microstructural evolution at higher resolution, TEM investigations were carried out for samples tested at 550 °C and different stain amplitudes (see, Fig. 4.23 tested at 0.2%/0.3% and Fig. 4.24 tested at 0.5%/0.75%). By comparing with that at the recrystallized state (Fig. 4.1d), the fatigued specimens show a high density of dislocations. Furthermore, the dislocation density varies from grain to grain, and increases with increasing the applied strain amplitude (Fig. 4.23 and Fig. 4.24), confirming EBSD results.

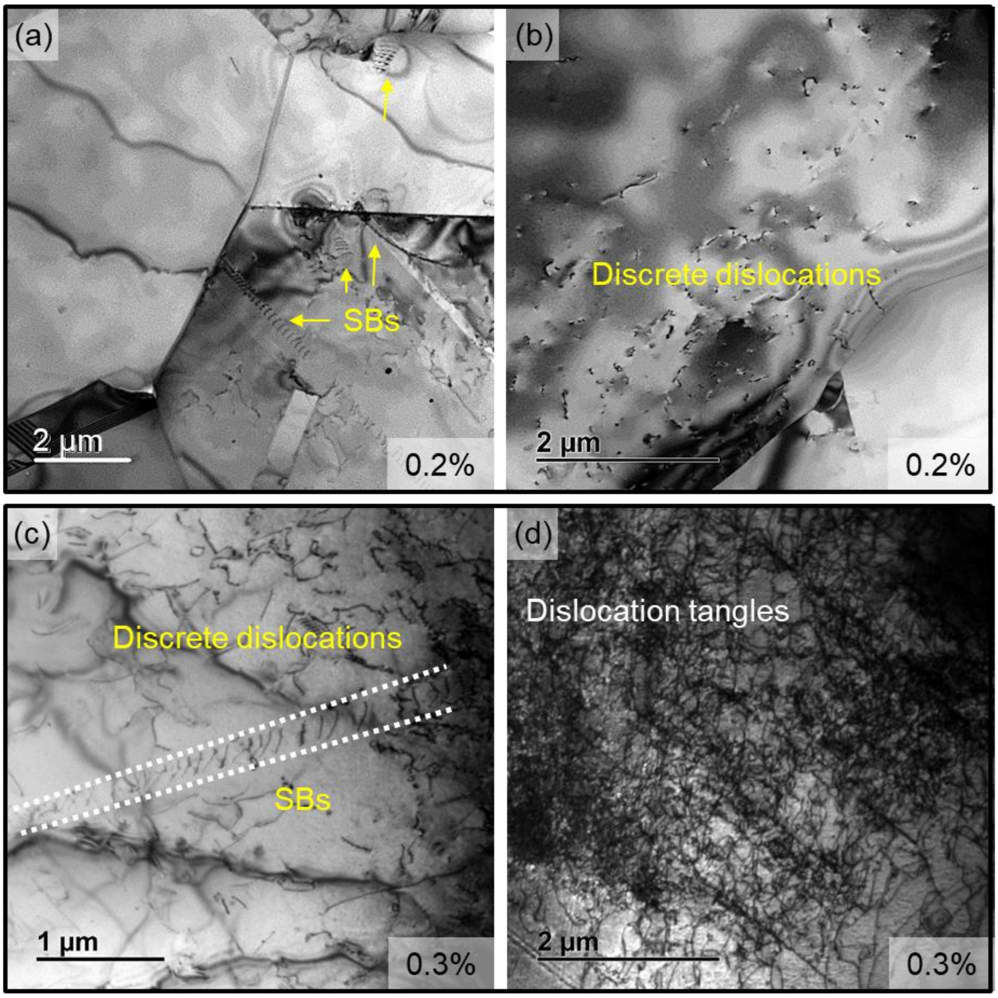

Fig. 4.23: BF-TEM micrographs of FG CoCrFeMnNi samples tested under low strain amplitudes of (a-b) 0.2% and (c-d) 0.3% at 550 °C [62]. At low strain amplitudes, most grains are manifested by planar slip band (SB) and discrete dislocations, except for few grains showing dislocations tangles.

Furthermore, the applied strain amplitude also changes the formed dislocation structures. Specifically, at low strain amplitudes (*i.e.*, 0.2% and 0.3%), most grains manifest low-density of planar SBs (in the form of pileups) and discrete dislocations (see Fig. 4.23a-c). In addition, few grains also reveal a relatively high density of dislocations, forming tangles (Fig. 4.23d). The prevalent SBs herein are similar to those observed at RT under low strain amplitudes (see Fig. 4.13a-c).

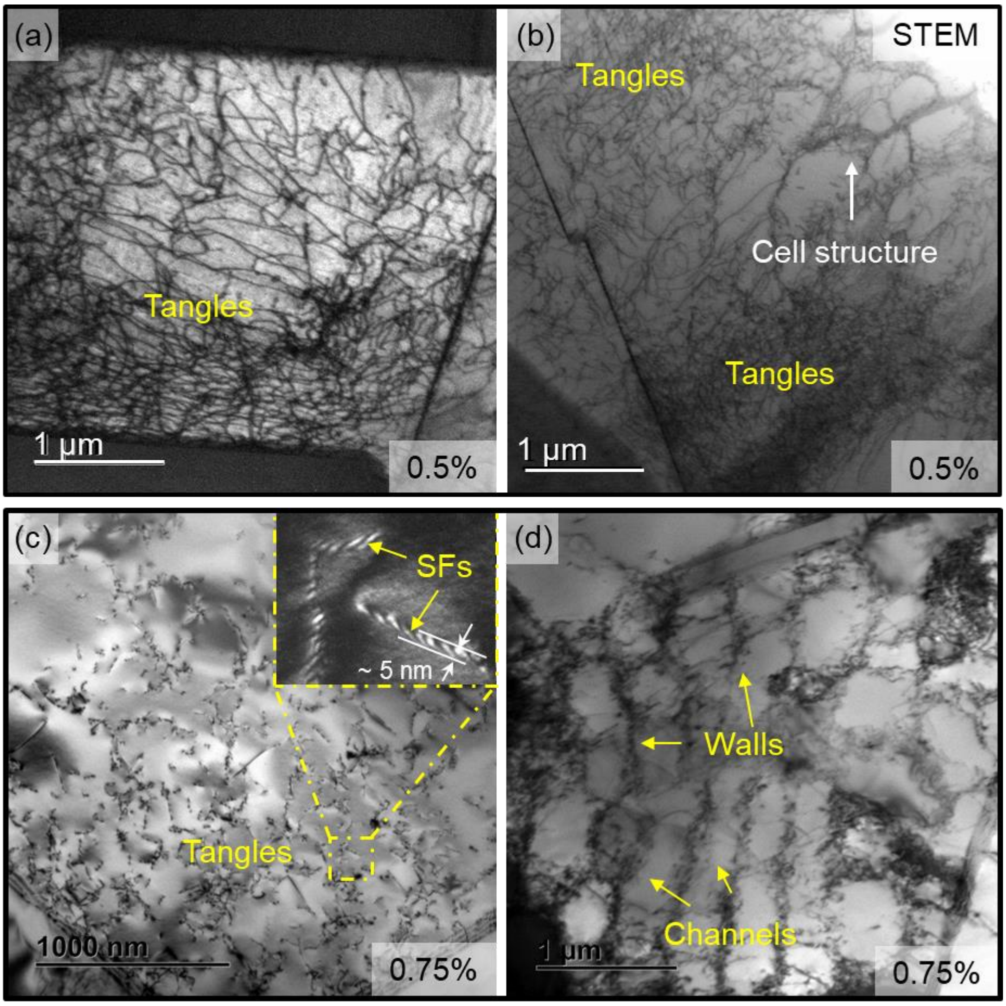

Fig. 4.24: TEM micrographs of FG CoCrFeMnNi samples tested under low strain amplitudes of (a-b) 0.5% and (c-d) 0.75% at 550 °C [92]. At these medium-to-high strain amplitudes, most grains are manifested by dislocation tangles band and substructures (*i.e.*, walls and cells separated by channels). (c) Dislocation tangles consisting of partial dislocations with stacking faults (SFs) in-between. The SF width in the inset of (c) is estimated to be ~ 5 nm. (a, c-d) are BF-TEM micrographs, (b) is HAADF-STEM micrograph, and the inset of (c) is WBDF-TEM micrograph.

At medium-to-high strain amplitudes (*i.e.*, 0.5% and 0.75%), both dislocation tangles and dislocation substructures (*e.g.*, cells and walls separated by channels) are recognized at 550 °C (Fig. 4.24). Among them, the substructures at 550 °C (Fig. 4.24d) are analogous to the main features at RT (*e.g.*, wall, cells in Fig. 4.14). Nevertheless, the tangles are distinct from the RT observations. Furthermore, the tangles are found to consist of partial dislocations with in-between SFs (see Fig. 4.24c), suggesting active planar slip.

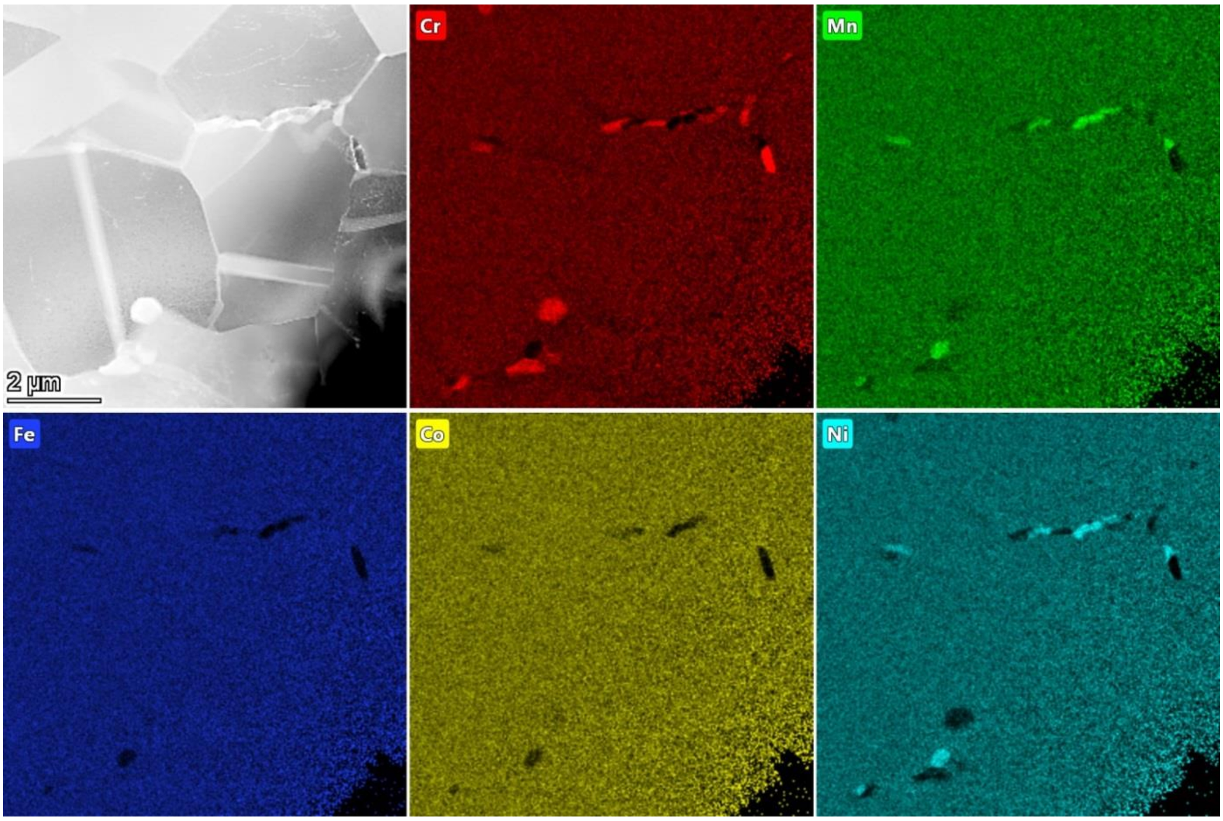

Fig. 4.25: HAADF-STEM micrograph along with corresponding EDS maps show two kinds of secondary phases at grain boundaries: 1) Cr-enriched and 2) NiMn-enriched in the sample tested under 0.5% strain amplitude at 550 °C [62].

After cycling, another striking observation at 550 °C is the segregation of alloying elements near grain boundaries in the form of sub-micron sized precipitates (see secondary phases in Fig. 4.25). Based on the chemical analysis, these precipitates are found to be of two types: 1) Cr-enriched and 2) NiMn-enriched (see EDS elemental maps in Fig. 4.25). Additionally, the segregation volume fraction was found to be higher at smaller strain amplitudes, as these tests led to longer temperature exposure (the fatigue tests last from about 1 to 47 hours for strain amplitudes ranging from 0.8% to 0.2%). Careful investigation on the recrystallized and RT-fatigued samples revealed no sign of such segregation.

4.5 Discussion

4.5.1 Cyclic deformation mechanisms at RT

4.5.1.1 Influence of strain amplitude on dislocation structures

TEM investigations on distinct dislocation features obtained at different strain amplitudes (Sections 4.4.1.1-4.4.1.3) uncovered the influence of strain amplitude on the deformation mechanisms.

At a low strain amplitude of 0.3%, planar SBs, in some cases along with dislocation dipoles, are predominantly observed (Fig. 4.13). The formation of dipoles is related to the loading on reversal that may activate dislocation sources in the opposite directions [93]. These dislocation structures suggest that at low strain amplitudes, CoCrFeMnNi deforms by planar single-slip, which is similar to that observed at low strains under monotonic loading [10]. The planar slip is attributed to the material's low-to-medium SFE [10].

Contrarily, at higher strain amplitudes (0.5% and 0.7%), dislocation-rich regions (*i.e.*, substructures, including walls (or ladders), cells, labyrinth and veins) separated by dislocation-depleted regions (*i.e.*, channels) are typically observed (Fig. 4.14, Fig. 4.18 and Fig. 4.19). Among these substructures, wall and ladder substructures have similar morphology as PSBs [46, 47, 70, 94-98]. These PSB-walls have been reported to originate from the metastable vein structures [99]. The formation of edge-multipole veins can be attributed to the effective elimination of screw dislocations by extensive cross slip. Therefore, the wavy slip mode, characterized by easy cross slip, favors the formation of the metastable veins and their transformation into PSBs. Furthermore, veins and walls have been reported to mainly contain full dislocations with the same ***b*** (*i.e.*, dislocations from primary slip system) [94]. However, in this work, veins and walls are proved to consist of dislocations with different ***b*** (*i.e.*, dislocations from multiple slip systems) (Fig. 4.17d-f). Notably, this observation is consistent with a previous report [100].

For cell and labyrinth substructures, it is well-accepted that easy cross slip and multiple slip are essential prerequisites for their formation [94, 100]. Consistently, present results confirm that multiple slip (including cross slip) contributes to their formation. Furthermore, labyrinth and then cell substructures have been considered to transform from wall substructures [101]. Since present results confirm that all of them originate from multiple slip (including cross slip), it is reasonable to conclude that dislocation walls are also metastable structures, which upon further loading could transform into labyrinth and then cell structures. Indeed, at higher strain amplitude (0.7%), more frequent labyrinth and cell structures were observed.

Together, these results suggest that increasing strain amplitude leads to a transition of slip mode from planar slip (*i.e.*, slip bands) to wavy slip (*i.e.*, walls, veins, labyrinth, and cells) in CoCrFeMnNi.

Typically, the dislocation configurations are correlated to the cumulative inelastic strain to failure (*i.e.*, $\varepsilon_{cum} = 2 \cdot \Delta\varepsilon_{in} \cdot N_f$). For both FG and CG materials, ε_{cum} was calculated and plotted against applied strain amplitude in Fig. 4.26. Evidently, at the lowest applied strain amplitude (0.3%), ε_{cum} is largest, primarily due to the highest experienced lifetime; and it decreases with increasing strain amplitude. Furthermore, due to longer fatigue life, FG material also manifests higher ε_{cum} than CG material at each investigated strain amplitude.

Another interesting observation is that, despite the experienced highest ε_{cum}, no prominent dislocation substructures formed at low strain amplitude of 0.3%. Rather, the substructures formed at higher strain amplitude (0.5% and 0.7%) with lower ε_{cum}. Therefore, these observations indicate that the saturated dislocation structures are more related to the applied strain amplitude rather than to the accumulated inelastic strain (ε_{cum}). This is because planar slip, which is more reversible as compared to cross slip, is more dominant at 0.3% strain amplitude; whereas, at higher strain amplitudes, dislocation interactions (including their annihilation) lead to the formation of dislocation substructures, due to the activation of multiple slip (including cross slip).

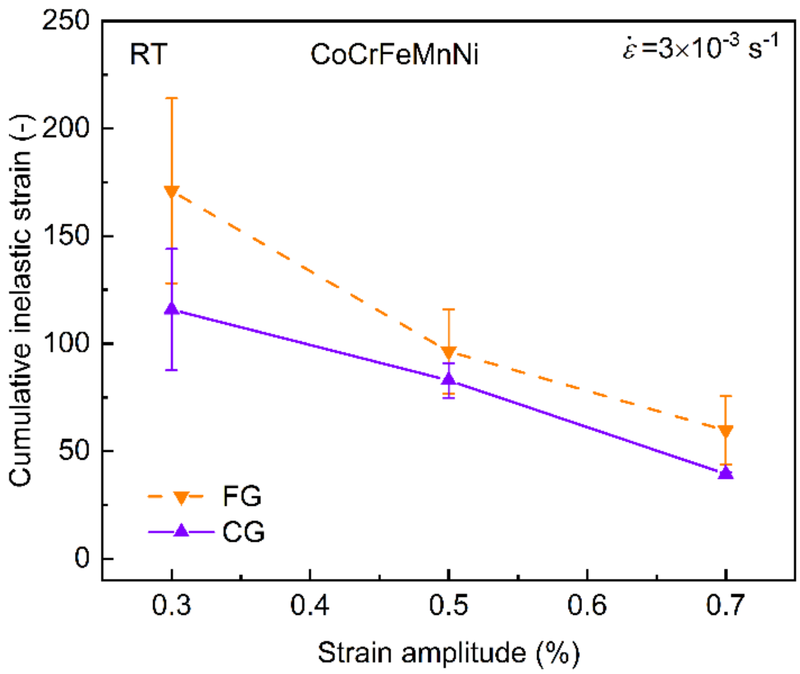

Fig. 4.26: Cumulative inelastic strain to failure of FG and CG CoCrFeMnNi is plotted against strain amplitude [86]. The lines are guidelines to the eye, only.

4.5.1.2 Influence of cycle number on dislocation structures

TEM investigation on the specimens of the interrupted test with 0.5% strain amplitude revealed the evolution of dislocation structures (Section 4.4.1.2), which can be correlated with the observed cyclic stress response.

During the initial cycles (*e.g.*, 20th cycle), dislocations nucleate/multiply and spread across grains via planar single-slip (*e.g.*, SBs, Fig. 4.16c-f). Otto et al. [10] also reported planar single-slip to dominate at small strains under monotonic loading at RT (*e.g.*, up to 2.1%). Here, dislocation multiplication and interaction with solute atoms contribute to the increased flow stress (*i.e.*, cyclic hardening, Fig. 4.2a). As the flow stress increases, the secondary/multiple slip systems are activated, leading to the formation of dislocation tangles (see Fig. 4.16a-b). Moreover, the curved morphology of dislocations (Fig. 4.16a-b) and the measured same ***b*** for dislocations in two slip bands (Fig. 4.16c) give indications of their wavy/cross slip behavior. Therefore, it can be concluded that slip is initially planar, but it quickly expands to wavy slip that is the dominant slip mode for the entire lifetime.

Upon further cycling (*e.g.*, at 500th cycles, softening stage), dislocations from multiple slip systems (*i.e.*, tangles) rearrange into ill-defined walls and veins, separated by channels (Fig. 4.17) to minimize stored dislocation strain energy [102, 103]. In dislocation-depleted channels, discrete dislocations are found to have screw character (Fig. 4.17a, d-f), consistent with previous findings on FCC metals [94]. As these screw dislocations can glide or cross slip, they could mutually annihilate with dislocations of opposite ***b*** and deposit edge segments along the walls [104]. The screw dislocation motion is also envisioned to shuffle forward and backward upon cycling and carry most of the imposed plastic strain [93, 104]. Therefore, the increased mean free path (*i.e.*, in channels) for dislocation movement contributes to the cyclic softening (Fig. 4.2a).

With further cycling (*i.e.*, at near-steady state), dislocations continue to rearrange into high-density and low-density regions, leading to the formation of well-developed substructures in most grains (Fig. 4.18). The near saturation of the dislocation configurations and densities, resulting from a dynamic equilibrium between dislocation multiplication and annihilation [16], contributes to a minor change in the flow stress until failure (Fig. 4.2a).

Though based on intermittent TEM observations at 0.5% strain amplitude, the above analyses are considered to also apply to samples tested at other high strain amplitudes (*e.g.*, 0.7%), according to their similar dislocation substructures (Fig. 4.14 and Fig. 4.18). In addition, the secondary hardening for 0.7% strain amplitude (Fig. 4.2a) can be associated with the transformation of walls into labyrinth and cell structures, which decreases the mean free path of dislocation movement.

Additionally, for the sample tested at low strain amplitude (*e.g.*, 0.3% with planar slip domination, see Fig. 4.13), the microstructural evolution is different from wavy substructures at 0.5% strain amplitude. It could be expected that dislocation multiplication and interaction (mainly along with solutes) contribute to the initial cyclic hardening. Upon further cycling, dislocations (*i.e.*, dipoles) in the planar SBs move and annihilate, leading to cyclic softening. Thereafter, as the dislocation density reaches a quasi-stable state, the flow stress tends to saturate until failure.

4.5.1.3 Role of deformation twinning and short-range ordering

It is of interest to clarify the role of deformation twinning (DT) upon cyclic loading. In this work, at the highest tested strain amplitude (0.7%), DT is sporadically observed in grains with their <111> axis along the loading direction of CG CoCrFeMnNi (Fig. 4.20). Contrarily, no DT was observed in FG samples, despite a higher stress level at similar testing conditions.

The likely reason lies in the fact that the critical stress required for twinning (CTS) is grain-size dependent [105]. Laplanche et al. [32] obtained an experimental CTS value of 720 ± 30 MPa for CoCrFeMnNi with ~ 16 μm grain size. Although the experimental CTS values for the investigated grain sizes are not yet available, present results suggest that the CTS must have been achieved upon cycling for the CG CoCrFeMnNi, while not for the FG version. Nonetheless, it is noteworthy that due to the limited volume fraction of DT, they should have a minor contribution in accumulating inelastic strain; and hence, in governing fatigue properties of CoCrFeMnNi in the investigated strain amplitude range.

Moreover, of interest to note is that the local chemical short-range ordering (SRO), if existent, could also affect the stress response. Specifically, during deformation, SRO has been linked to both hardening (as dislocations shear SRO domains) and subsequent glide plane softening (as favorable dislocation paths are introduced) [106]. Furthermore, the presence of SRO is generally believed to influence dislocations slip mode by generating pile-up stresses that destruct SRO irreversibly (*i.e.*, to create a planar path for following dislocations to glide through) [53, 89, 107, 108]. However, it still remains a scientific challenge to directly visualize SRO [106, 109].

Since the planar slip mainly dominated at low strain amplitude (0.3%) and the wavy slip prevailed at medium-to-high strain amplitudes, it is less likely that the SRO was destructed only at low strain amplitude but not at high strain amplitudes. Coupled with the fact that no strong indication of SRO in literature was reported so far for the CoCrFeMnNi alloy, it can be concluded that the role of SRO in the cyclic response is either non-existent or negligible herein.

4.5.1.4 *Influence of grain orientation on dislocation structures*

For microstructural-based modeling, the type of dislocation structure formation based on grain orientation is of particular interest. It is well-accepted that for FCC single crystals (*e.g.*, copper, nickel), PSB-wall and labyrinth structures dominate in near [011] and [001]-oriented grains (// LD), respectively [67]; while in near $[\bar{1}11]$-oriented grains, vein and cell structures are found at low and high strain amplitudes, respectively [67, 68].

In the present study, for polycrystalline CoCrFeMnNi, no significant correlation between dislocation patterns and grain orientations was observed (Section 4.4.1.3). This could be related to the different amount of constraint effects from the distinctly different neighboring grain environments. For instance, at medium and high strain amplitudes, in different regions of the same grain (*e.g.*, the core and boundary of the grain), different amount and/or types of slip systems (*e.g.*, primary, cross, and conjugate slip systems) are activated to maintain strain compatibility across the GBs (especially in large grains). Besides, for grains with similar orientations, their neighboring grains orientation might also be different, which could impose a different amount of constraint effects (or different local stress); hence, leading to the development of different dislocation structures (Fig. 4.18a, d).

Moreover, the amount of constraint effects within a single grain may also vary (especially for coarse grains). As illustrated in Fig. 4.27, regions 1 and 2 may experience a different amount of constraint effects because of different neighboring grain orientations, which give rise to the simultaneous formation of wall and cell structures in a single grain (see a similar TEM micrograph in Fig. 4.18d). Specifically, the larger amount of constraint effects (*e.g.*, see region 2 in Fig. 4.27) could promote walls to transform into cells structure.

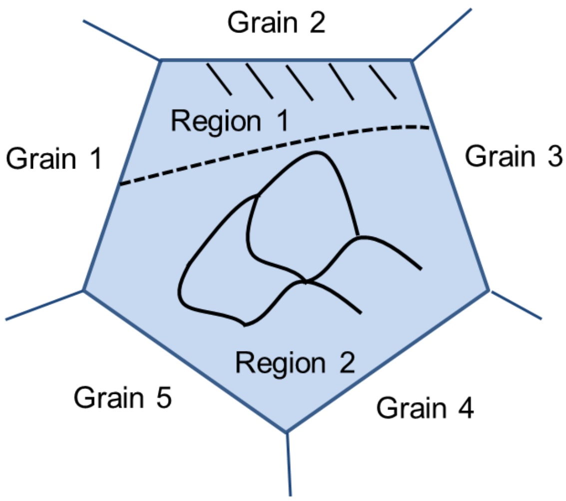

Fig. 4.27: A schematic illustration of mixed (cells and walls) structures formation in a single grain [86].

Furthermore, the above interpretation complements the rationalization provided by Ref. [64], where the simultaneous development of cell and wall mixed structures in a single grain was ascribed to the activation of cross/wavy slip and planar slip, respectively. Their rationalization is based on the description by Copley and Kear [110], *i.e.*, that reversing the sign of applied stress leads to the change of Shockley partial separation distance (and hence, the change of 'effective' SFE) for certain orientations; and thus, might cause a change in the dislocation slip mode [110]. To validate this rationalization, the orientations for the investigated grains showing cell/wall/mixed structures in the present study are plotted in the color-coded IPFs, see Fig. 4.28.

The connecting line between [102] and [113] separates the regions of extension or contraction of stacking faults confined by the partial dislocations, which is illustrated by the difference in Schmid factors on the partials (provided for tension; for compression, the sign reverses). The anisotropy becomes more pronounced with increasing distance from this line (hence, significant change between wavy/planar slip during load reversal).

Since no systematic trend of grain orientation was found for either of the assigned structures in Fig. 4.28a-b, and all dislocation substructures were confirmed to originate from multiple slip (including cross slip, see Section 4.5.1.1) rather than the planar slip, it is suggested that the formation of mixed structures in a single grain is dictated more by the constraint effects of neighboring grains.

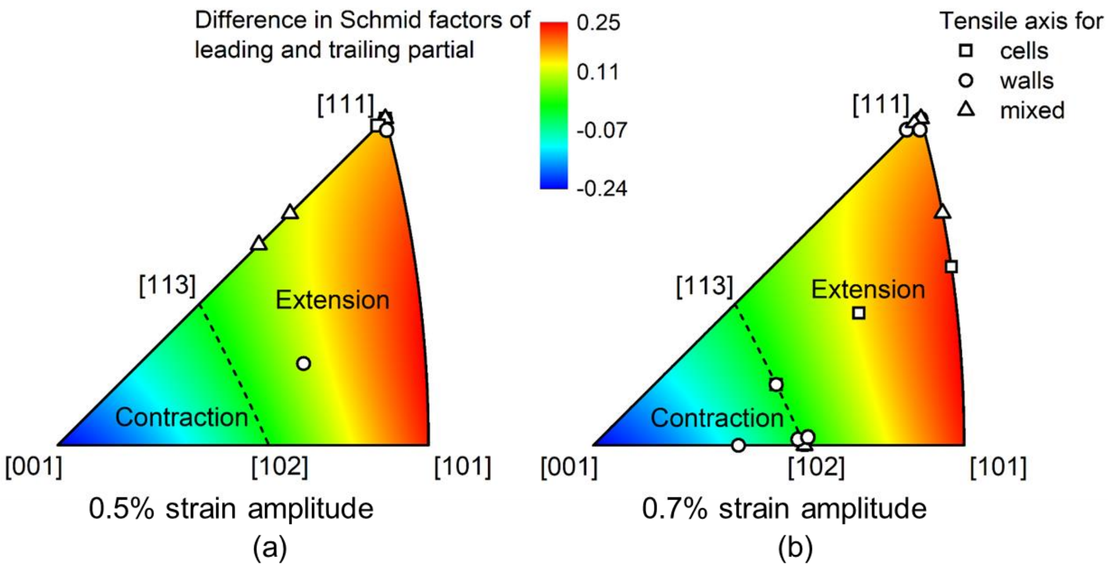

Fig. 4.28: Color-coded IPFs, showing orientations for the grains with cell/wall/mixed structures, were obtained from FG samples tested at (a) 0.5% and (b) 0.7% strain amplitude [86]. The line between [102] and [113] separates the regions of extension or contraction of partial dislocations (provided for tension; for compression, the sign reverses).

Additionally, no significant relation between grain orientation and dislocation structures for CoCrFeMnNi is consistent with those observed for other FCC polycrystalline materials (*e.g.*, copper, 316L steel), where various dislocation patterns were observed in grains with similar orientation or a single grain [96, 100]. In contrast, a study on fatigued polycrystalline nickel [111] reported that the dislocation patterns, observed via electron channeling contrast imaging (ECCI), are similar to that for a single crystal with the same orientation. This discrepancy may arise from the fact that, though ECCI could provide a larger overview of microstructures, its resolution is not as high as TEM to differentiate between cell and wall (or vein) structures. Indeed, a later study on fatigued polycrystalline nickel [112] showed mixed dislocation structures (walls and cells) in a single grain via TEM, which is consistent with the present investigations.

4.5.2 Cyclic deformation mechanisms at 550 °C

4.5.2.1 Influences of strain amplitude and cycle number on dislocation structures

Upon cycling CoCrFeMnNi at 550 °C and different strain amplitudes, the main differences lie in dislocation density (*i.e.*, increase with strain amplitude) and distinct dislocation slip mode.

At low strain amplitudes, the planar SBs and discrete dislocations indicate planar single-slip as the main active deformation mechanism at 550 °C (Fig. 4.23). This deformation mechanism is similar to that at RT and low strain amplitudes. While at medium and high strain amplitudes, the observed tangles, which consist of partial dislocations and in-between SFs, suggest dislocations planar slip (Fig. 4.24). Meanwhile, the observed dislocation substructures formation herein is analogous to that observed at RT, indicating multiple slip and wavy slip activation (Fig. 4.24).

Notably, these dislocation structures were obtained from the post-fractured (*i.e.*, end-life) samples. It is also suggested that at initial cycles, the planar slip is prevalent for CoCrFeMnNi at different temperatures [10, 86]. Taken together, the evolution of dislocation's slip mode with strain amplitude and cycle number at 550 °C can be illustrated in Fig. 4.29. In detail, with increasing cycle number at 550 °C, dislocation slip mode remains planar slip at low strain amplitudes (0.2% and 0.3%); whereas it changes from initially planar slip to coexisting planar slip and wavy slip at medium-to-high strain amplitudes (0.5% and 0.75%).

As the deformation mode of FCC ductile materials is primarily determined by the SFEs [63], the above evolution of slip mode is also believed to be applicable for other FCC MPEAs of similar SFEs.

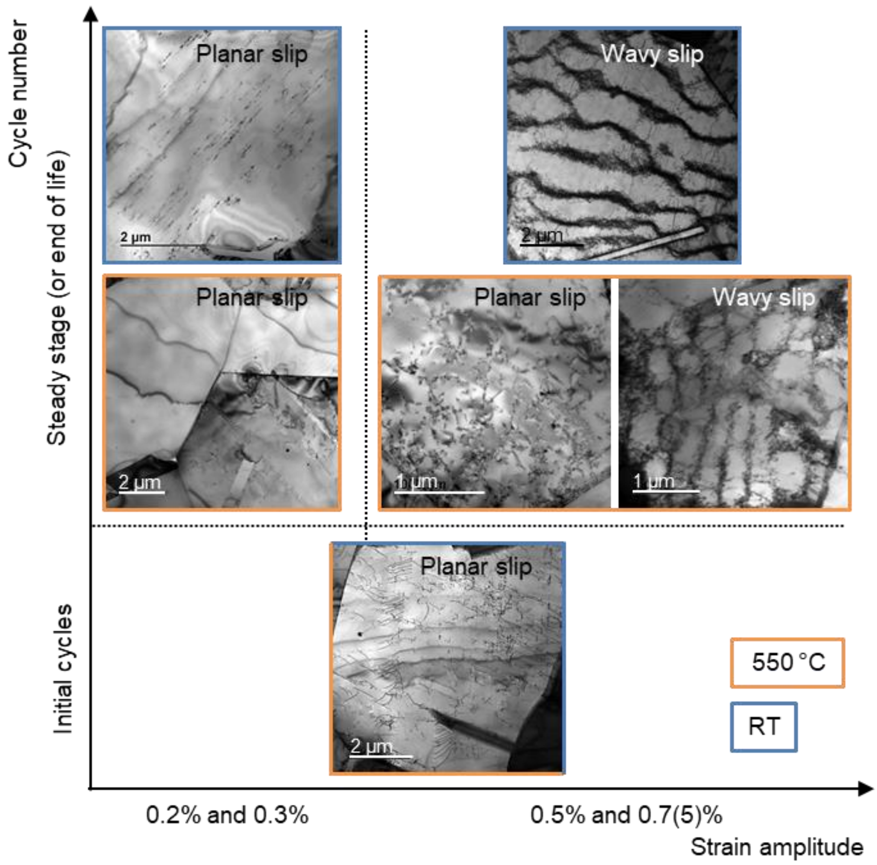

Fig. 4.29: Schematic illustration of dislocation's slip mode evolution with strain amplitude, cycle number at 550 °C and RT [92]. The planar slip at initial cycles is valid for both RT and 550 °C. The RT results are shown for later comparison (Section 4.5.2.4).

The reasons for the deformation modes at 550 °C can be interpreted as follows. Under low strain amplitudes, the dominating planar slip can be explained by limited activated slip system at lower stresses. While under medium-to-high strain amplitudes, the presence of wavy slip is expected, and is mainly associated with thermal recovery and stress-induced activation of cross slip at higher stresses [62].

However, the co-existing planar slip (with cross slip) at higher strain amplitudes is rather unexpected, which might be rationalized by the well-known Suzuki segregation [113]. The segregation is believed to increase dislocations dissociation width (or SF width) by locally decreasing SFE [114, 115]. Direct evidence on Suzuki segregation has been reported for FCC stainless steels, Ni- and Co-Ni- based superalloys [115-119]. For example, Kaneko et al. [116] found that the SF width in a stainless steel deformed at 523 K and 673 K is larger than that deformed at RT. Viswanathan et al. [117] observed segregation of Co and Cr to the SF, whilst deficiency of Ni and Al at the SF in Ni-based superalloys at 750 °C using Super-X EDS mapping.

In this study, upon cycling CoCrFeMnNi alloy at 550 °C, the observed NiMn- and Cr-enriched secondary phases along grain boundaries (*e.g.*, see Fig. 4.25) suggest elemental diffusion. Kawamura et al. [120] further observed slight enrichment of Mn element at the SF in a pre-deformed CoCrFeMnNi followed by annealing at 1073 K for 30 min. In this context, the elemental diffusion induced secondary phases in this study could be taken as an indication of possible segregation of solutes to SF. This segregation may give rise to high energy barriers for Shockley partial dislocations constriction and increase the SF width in CoCrFeMnNi [114]. The evidence of increased SF width at 550 °C can be found, *e.g.*, in Fig. 4.24c (~ 5 nm), compared to full dislocations at RT (Fig. 4.17d-f). Therefore, Suzuki segregation likely plays a key role in CoCrFeMnNi deformation provided the temperature is high enough to allow atomic diffusion to occur at a speed comparable to that of the dislocations [120]. Nevertheless, more efforts are required to provide direct evidence of Suzuki segregation and understand the corresponding driving force for CoCrFeMnNi.

It is also worth noting that, the presence of planar slip (or wavy slip) in different grains under medium-to-high strain amplitudes at 550 °C could be associated with 1) grain orientation and 2) constraints by neighboring grains. These factors might determine the velocity of dislocation motion, either favoring the extension of partial dislocations (leading to planar slip) or promoting the constriction of partial dislocations (allowing for wavy slip) in different grains.

4.5.2.2 Elemental segregation induced secondary phases

It has been reported that for CoCrFeMnNi, annealing at above 800 °C kept the alloy as a stable single-phase solid-solution, whereas annealing at below 800 °C led to the formation of secondary phases [121-123]. For example, Otto et al. [123] found the formation of NiMn-, FeCo- and Cr-enriched phases, depending upon annealing temperature (500 °C and 700 °C for 500 days). Similar observation of decomposition was also reported in the combination of deformation and shorter annealing durations

[121-124]. For instance, Schuh et al. [121] detected phase decomposition including formation of Cr-, FeCo- and NiMn-enriched phases, after annealing high-pressure torsioned CoCrFeMnNi at 450 °C for shorter durations (5 minutes to 15 hours). This phase decomposition was assisted by the presence of large number of grain boundaries that serve as fast diffusion pathways and preferential nucleation sites for the formation of secondary phases [121].

It should also be noted that the Cr-enriched phases formed during high-temperature annealing could be Cr-rich sigma phase [123, 125] and/or Cr-rich $M_{23}C_6$ [126]; whereas the NiMn-enriched phases could be tetragonal $L1_0$ NiMn phase [121, 123, 126].

Under these contexts, it is not surprising for the observed segregation-induced secondary phases (*e.g.*, Cr- and NiMn-enriched phases near grain boundaries, see Fig. 4.25) upon cycling the CoCrFeMnNi at elevated temperatures. Moreover, since these regions are depleted of Fe and Co, the Fe- and Co-enriched regions are also expected to be present. Nevertheless, the effect of cyclic straining, *i.e.*, if in-situ cyclic deformation provides additional driving force for precipitation (faster precipitation kinetics), still needs to be investigated.

4.5.2.3 Serrated flow

For the CoCrFeMnNi, serrated flow occurred during the LCF loading at elevated temperature (550 °C) (Fig. 4.6). This phenomenon has been widely reported for quasi-static deformation in various conventional alloys [127-134] and MPEAs [9, 10, 122, 135-139].

In general, the occurrence of serrated flow can be explained in terms of dynamic strain aging (DSA). McCormick [140] proposed that when mobile dislocations are arrested by a forest dislocation, solute atoms will diffuse to these arrested dislocations, leading to an increase in flow stress by impeding their movement. Once the flow stress reaches a critical value, the arrested dislocations can escape from the solute atmosphere. At this instance, comparatively lower stress is required to move dislocations until they are locked again by the next forest dislocation [140, 141].

In DSA, the competition between solute mobility and dislocation velocity plays a crucial role [142, 143]. DSA in steels has been attributed to the strong interactions between mobile planar dislocations and solute atoms, such as interstitial C or N atoms at lower temperatures (250−450 °C), or substitutional Cr atoms at higher temperatures (450−650 °C) due to different activation energy [127, 128].

The major uncertainty in the case of MPEAs has been the unclear understanding of the elements that can be considered as solute atoms to impede mobile dislocations [137]. He et al. [122] proposed that it is the diffusion of one of the constituent elements which acts as the solute atom that controls the drag of gliding dislocations and the deformation rate at lower strain rate. For $Al_{0.3}$CoCrFeNi MPEA, Yasuda et al. [136] showed that the solute atmosphere of Al atoms around moving dislocations or stacking faults is closely related to the DSA. For CoCrFeMnNi, DSA related serrations are reported to have occurred at both cryogenic temperature (4.2 K/8 K) [11, 33] and elevated temperature range (300−620 °C) [9, 135]. Wu et al. [9] and Carroll et al. [135] performed systematic studies using different compositional subsets of CoCrFeMnNi system. They reported the appearance of high temperature serrations in CoCrNi, NiCoMn, NiCoFe, NiFeMn, NiCoFeMn and NiCoFeCr alloys but not in pure Ni and its binary subsets (FeNi and NiCo) during tensile straining at 400 °C [9, 135]. Therefore, it appears that it is not one specific element, but different elements or their combined synergistic effect that leads to serrations in CoCrFeMnNi MPEA and its subsets.

In the present study, mobile planar dislocations appear to have undergone jerky motion (see Fig. 4.23). This can be taken as evidence of the locking and unlocking of dislocations from solute atoms during initial cycling, leading to an increase and decrease in flow stress, respectively. Similar to the current work, several LCF studies on FCC steels [133, 144, 145] emphasized dislocations planar slip dominance in similar testing temperature regimes (*e.g.*, 550−600 °C), where serrated flow occurred. Interestingly, unlike the prevalent planar slip in FCC steels, the present results reveal that in CoCrFeMnNi, dislocations wavy slip complements planar slip after several cycles cycling at 550 °C. Moreover, the gradually disappearing serrated flow at 550 °C might be related to the presence of wavy slip, which likely allows dislocations continuous movement and hence plastic deformation. Therefore, this work suggests that, upon cycling FCC materials at intermediate elevated temperatures (*e.g.*, 550 °C), the role of wavy slip (*e.g.*, probably to reduce the magnitude of serrated flow) should not be neglected (or should be interpreted with caution).

It is also of interest to note that the DSA may lead to reduced lifetime. For instance, for a 316LN steel cycled at 550 °C, with reducing strain rate, more planar slip bands and hence more intense DSA activity were found [146]. This caused reduced LCF life due to grain boundary cracking from slip bands [146]. Hence, a detrimental effect of DSA (*e.g.*, at lower strain rates) on the LCF life could be anticipated for CoCrFeMnNi.

4.5.2.4 Influences of temperature on deformation mode and lifetime

Upon comparison of dislocations structures at RT (from Sections 4.5.1.1−4.5.1.2) and 550 °C (Section 4.5.2.1), a temperature-dependent dislocation slip mode can be recognized (see Fig. 4.29). The main difference lies in the near-steady (or end-life) under medium-to-high strain amplitudes (0.5% and 0.75%). At these conditions, in contrast to the dominating wavy slip at RT, planar slip complements the wavy slip at 550 °C. This confirms the prediction of their different slip mode from the cyclic stress-strain curves (Fig. 4.7). As aforementioned, this temperature-dependent slip mode arises from the activation of diffusion at 550 °C, where Suzuki segregation likely played a role.

The above-mentioned temperature influence on slip mode contributed to the difference in the cyclic stress response at different temperatures (*i.e.*, the absence of cyclic softening at 550 °C, see Fig. 4.5a). Generally, the initial cyclic hardening and near-steady state at 550 °C could be explained by the rationalization for RT (in Section 4.5.1.2). Differently, the pronounced dislocation substructures formation at RT has been correlated to the observed cyclic softening (Fig. 4.2a). However, at 550 °C, the coexisting planar slip (Fig. 4.24c) suggests the reduced extent of wavy-substructures (*i.e.*, dynamic recovery). The reduced dynamic recovery can be further supported by the higher KAM values (*i.e.*, higher GND densities) at 550 °C (Fig. 4.21b) as compared to RT (Fig. 4.12c). Therefore, the reduced extent of wavy substructures might be responsible for the absence of cyclic softening at 550 °C (Fig. 4.5a).

Furthermore, the reasons for the different lifetime at two investigated temperatures should be clarified. At RT, dislocation's wavy slip induced strain localization plays a significant role in crack initiation (*i.e.*, by forming intrusions and extrusions). Compared to extensive wavy substructure formation at RT, planar dislocation configurations (*e.g.*, tangles) at 550 °C indicate that the deformation herein is more homogeneously distributed (*i.e.*, less localized). Despite less localized deformation, the lifetime is shorter at 550 °C compared to RT for the same inelastic strain amplitudes. From the microstructure perspective, these observations suggest that other factors contribute to the shorter lifetime at 550 °C.

One of the factors is the elemental segregation induced secondary phases along the GBs (Fig. 4.25). Once connected with surface grains, they may not only act as cracks initiation sites but also accelerate crack propagation, leading to earlier failure of the CoCrFeMnNi at elevated temperature. Another factor negatively affecting the lifetime is the simultaneous high-temperature oxidation, which is known to shorten the fatigue life of materials [147, 148]. Indeed, oxide layers were observed forming on the fatigued CoCrFeMnNi samples surface (Fig. 4.11d). Besides, Polak et al. [147] observed early intergranular cracking and oxidation of grain boundaries during high-temperature cyclic straining, which might also occur in the current material.

4.6 Summary

The LCF behavior of CoCrFeMnNi was investigated at different strain amplitudes and different temperatures (RT and 550 °C). Extensive TEM investigations were carried out to unravel the microstructural origins of the deformation behavior.

The key findings from RT investigations are summarized as follows:

- The CoCrFeMnNi shows initial cyclic hardening followed by softening and near-steady state before crack initiation and propagation, irrespective of the grain size. The majority of lifetime (~ 90%) is represented by the near-steady state.

- Reducing the grain size to a few micrometers leads to an enhanced LCF lifetime for CoCrFeMnNi at the investigated strain amplitudes. Nevertheless, the fine-grained and coarse-grained materials manifest similar Manson-Coffin relation (*i.e.*, inelastic strain versus lifetime), suggesting this relation to be independent of the grain size.

- The dislocation structure mainly consisted of planar slip bands at low strain amplitude (0.3%); while at larger strain amplitudes (0.5% and 0.7%), dislocation substructures including veins, walls, labyrinth, and cells prevailed. This is indicative of dislocation slip mode transition from planar slip to wavy slip with increasing strain amplitude.

- Dislocation-poor regions (*i.e.*, channels) between dislocation-rich regions (*i.e.*, veins and walls) form as a result of the extensive annihilation of the gliding and cross-slipping screw dislocations. This confirms that wavy slip contributes to their formation rather than planar slip.

- Dislocations in various substructures (*i.e.*, veins, walls, and cells) are proven to have different Burgers vectors. This indicates that, apart from wavy slip, multiple slip also contributes to their formation.

- Increasing cycle number results in dislocation structure evolution from initial tangles and planar slip bands to ill-defined wavy substructures; and then, finally to their well-defined versions. This dislocation structure evolution is linked well to the observed cyclic stress response.

- Distinct dislocation substructure formation in polycrystalline CoCrFeMnNi is dictated more by the constraints from neighboring grains rather than grain orientation. Additionally, the formation of various dislocation structures in a single grain is also linked to the constraint effects from the neighboring grains.

- Examinations on fracture surfaces and crack growth paths indicate that the crack generally initiates from sample surface, and propagates in a predominantly transgranular mode (along with striation features).

The main findings from 550 °C investigations can be summarized as follows:

- The CoCrFeMnNi shows initial cyclic hardening followed by a near-steady state before failure. In comparison to that at RT, CoCrFeMnNi exhibits the absence of cyclic softening and the presence of serrated flow at 550 °C.

- With increasing cycle number, the slip mode remains planar slip at low strain amplitudes (0.2% and 0.3%); whereas it changes from initially planar slip to coexisting planar slip and wavy slip at medium-to-high strain amplitudes (0.5% and 0.75%).

- At medium-to-high strain amplitudes, the unexpected planar slip likely arises from the increase of stacking fault width, which partly restricts cross/wavy slip at 550 °C.

- The serrated flow is ascribed to the interaction (*i.e.*, pining and unpinning) between mobile planar dislocations and diffusing solute atoms. Serrated flow seems to have a detrimental effect on the lifetime at 550 °C.

- Chemical segregation (*e.g.*, in the form of Cr- and NiMn-enriched secondary phases) was observed near grain boundaries upon cyclic straining. The formation of these phases could be taken as evidence of elemental diffusion, which contributes to serrated flow and increased stacking fault width in CoCrFeMnNi at 550 °C.

- Despite less localized deformation due to planar slip, CoCrFeMnNi exhibits reduced LCF life at 550 °C compared to RT. This is linked among others to the *in-situ* oxidation and elemental segregation induced grain boundary embrittlement at 550 °C.

5 Low-cycle fatigue behavior of CoCrNi alloy

This chapter describes the LCF behavior and underlying mechanisms of CoCrNi alloy at room temperature and compares them with those of the CoCrFeMnNi alloy. The contents of this chapter are organized as follows.

Section 5.1 introduces the received recrystallized microstructure. Section 5.2 provides the cyclic stress response and lifetime of CoCrNi alloy at different strain amplitudes and compares it to the CoCrFeMnNi alloy. Section 5.3 provides damage mechanisms of CoCrNi alloy. Section 5.4 displays the microstructural evolution with emphasis on dislocation structures. Section 5.5 discusses the deformation mechanisms (along with the comparison to CoCrFeMnNi). Furthermore, this section correlates the microstructural evolution with the cyclic stress response and lifetime. Finally, Section 5.6 summarizes the main findings.

5.1 Initial microstructure

Fig. 5.1a displays a representative IPF map of as-recrystallized CoCrNi. The IPF map confirms that the investigated material is a single-phase FCC alloy. Besides, the alloy exhibits a weak <111> and <100> texture along the rod axis, which is typical for rotary-swaged and subsequently recrystallized FCC alloys [12, 33]. Additionally, the alloy possesses equiaxed grains, with an average grain size of ~ 6 ± 3 μm, and a high density of annealing twins due to its low-to-medium SFE [12]. Furthermore, the initial dislocation density is low, as shown in a typical BF-TEM micrograph in Fig. 5.1b. These results indicate that the initial microstructure of the CoCrNi alloy is comparable to that of FG CoCrFeMnNi (Fig. 4.1). This ensures a fair comparison of the LCF response between the two alloys, *e.g.*, excluding the influences of grain size and texture on the comparison.

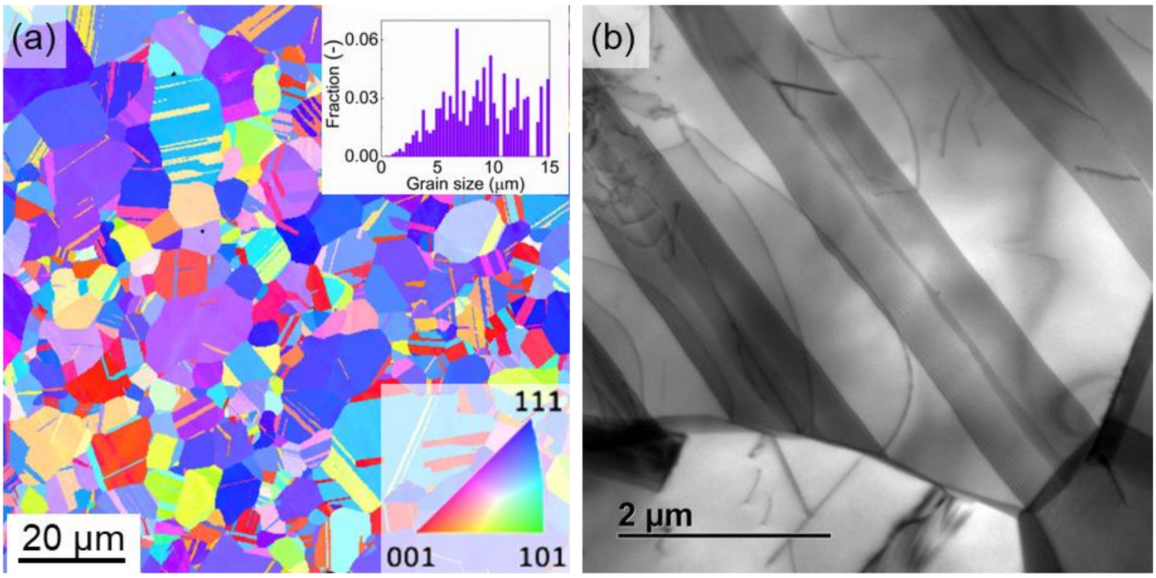

Fig. 5.1: Microstructures in the recrystallized state of CoCrNi: (a) IPF map along the rod axis, (b) bright-field TEM micrograph [63]. The grain size distribution was provided in the inset of (a).

5.2 Low-cycle fatigue response

5.2.1 Cyclic stress response

The tensile peak stress and inelastic strain amplitude were plotted against the *normalized* number of cycles (N/N_f) in Fig. 5.2a and b, respectively, for CoCrNi tested at different strain amplitudes. For comparison, corresponding responses of fine-grained CoCrFeMnNi were also produced in Fig. 5.2.

Similar to that of CoCrFeMnNi, the cyclic stress (*i.e.*, tensile peak stresses) response of CoCrNi in Fig. 5.2a can be divided into three stages: an increase (cyclic hardening stage), followed by a significant decrease (cyclic softening stage), and finally by a minor change (near-steady state) until failure. The initial cyclic hardening stage takes place during the first 20 to 30 cycles, the following cyclic softening stage represents ~ 10% of the lifetime. This indicates that the significant changes in the cyclic stress response represent a small fraction of the lifetime. In other words, the majority of the lifetime is spent in a near-steady state.

The inelastic strain response in Fig. 5.2b is consistent with the evolution of the peak stress, *i.e.*, it mainly manifests an initial sharp decrease followed by a gradual increase and near steady-state until failure. Similar curves showing these evolutions with the number of cycles can be found in Fig. 5.2c and d.

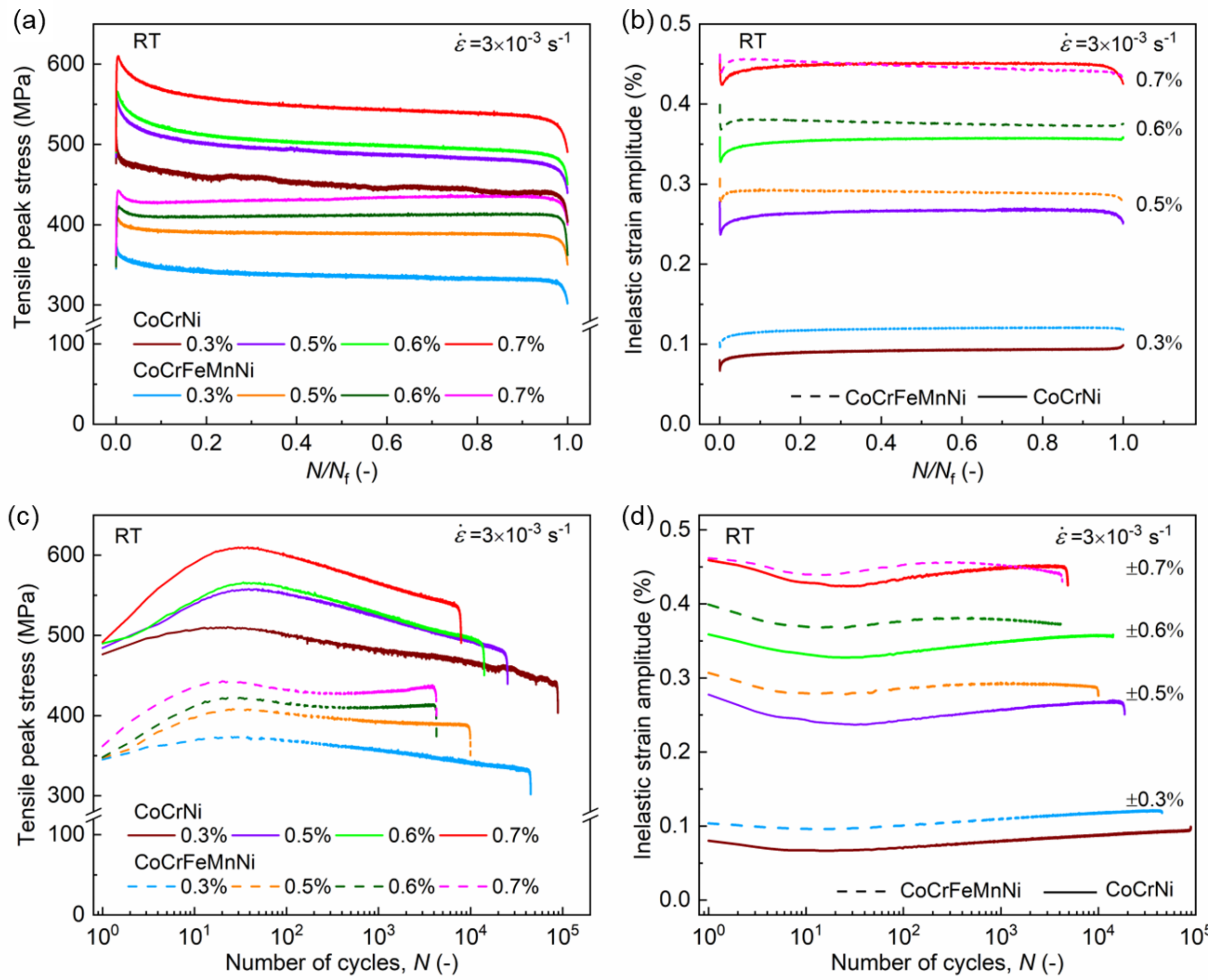

Fig. 5.2: (a) Tensile peak stress and (b) inelastic strain amplitude are plotted against the *normalized* number of cycles (N/N_f), (c) tensile peak stress and (d) inelastic strain amplitude are plotted against the number of cycles (N) at different strain amplitudes for FG CoCrNi and CoCrFeMnNi [63]. The color code in (a, c) is also valid in (b, d).

Upon comparison, CoCrNi exhibits higher cyclic strength and lower inelastic strain than CoCrFeMnNi for all tested strain amplitudes (Fig. 5.2). The lower inelastic strain amplitude in CoCrNi is related to its higher elastic strain ε_e. The higher ε_e is due to its higher cyclic/yield strength despite the higher elastic modulus, see Fig. 5.3. The higher yield strength of CoCrNi has been reported several times [9, 11, 12], and originates from two distinct contributions: 1) higher solid solution strengthening [36, 149] and 2) larger grain boundary strengthening [10, 150].

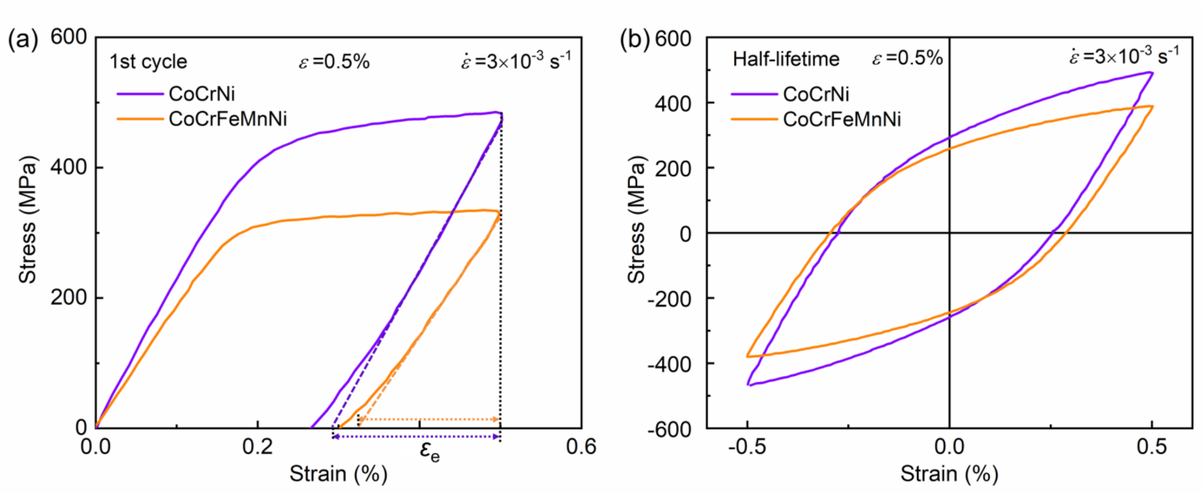

Fig. 5.3: (a) Stress-strain curves of the first quarter of the first cycle, and (b) half-life hysteresis loops, for FG CoCrNi and CoCrFeMnNi tested at 0.5% strain amplitude at RT [63]. CoCrNi exhibits higher cyclic strength and lower inelastic strain than CoCrFeMnNi.

To understand the cyclic stress-strain relation, the plots of saturated stress amplitude $\Delta\sigma/2$ *versus* inelastic strain amplitude $\Delta\varepsilon_{in}/2$ for both materials are provided in Fig. 5.4. The fitted parameters and curves by Eq. 2 are also presented in Fig. 5.4 and Table 5.1. As seen from Fig. 5.4, the slope (*i.e.*, n' value) of CoCrNi (0.08) is lower than that of CoCrFeMnNi (0.19), suggesting the former's lower cyclic hardening ability with respect to strain amplitude. Moreover, the distinct n' values of the two alloys indicate their different slip modes, likely CoCrNi having planar slip. This behavior will be confirmed later by TEM investigations.

Table 5.1: Values of the fitted parameters obtained from the LCF data for FG CoCrNi and CoCrFeMnNi based on Eq. 2.

Material	Cyclic strength coefficient, K' (MPa)	Cyclic strain hardening exponent, n'
CoCrNi	776	0.08

CoCrFeMnNi	1174	0.19

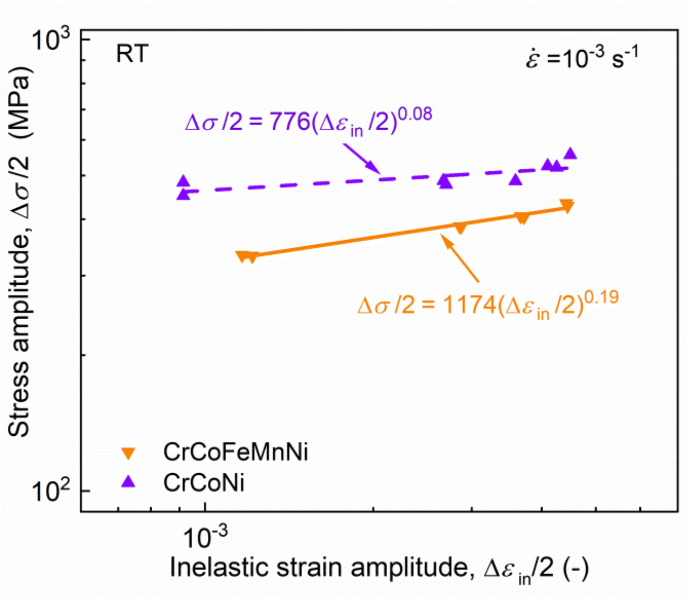

Fig. 5.4: The saturated stress amplitude ($\Delta\sigma/2$) *versus* inelastic strain amplitude ($\Delta\varepsilon_{in}/2$) plots of FG CoCrNi and CoCrFeMnNi.

5.2.2 Low-cycle fatigue life

To seek the difference in their fatigue resistance, the *S*-*N* curves and the Manson-Coffin curves of CoCrNi and CoCrFeMnNi are presented in Fig. 5.5a and b, respectively. For a given stress amplitude (Fig. 5.5a) or inelastic strain amplitude (Fig. 5.5b), CoCrNi alloy exhibits a longer fatigue life than CoCrFeMnNi alloy. The fitted parameters (c and ε'_f) according to Manson-Coffin law [90, 91] are presented in Fig. 5.5b and Table 5.2.

The values of parameter c for both alloys are within the typical range ($-0.7 \leq c \leq -0.5$) observed for most metals [16]. Since the parameter ε'_f is related to the monotonic test's fracture strain [16, 90, 91], the obtained ε'_f for CoCrNi is, as expected, larger than that of CoCrFeMnNi. This evidence suggests that other quinary and quaternary subsets of the CoCrFeMnNi system with higher fracture strain may also exhibit higher LCF resistance.

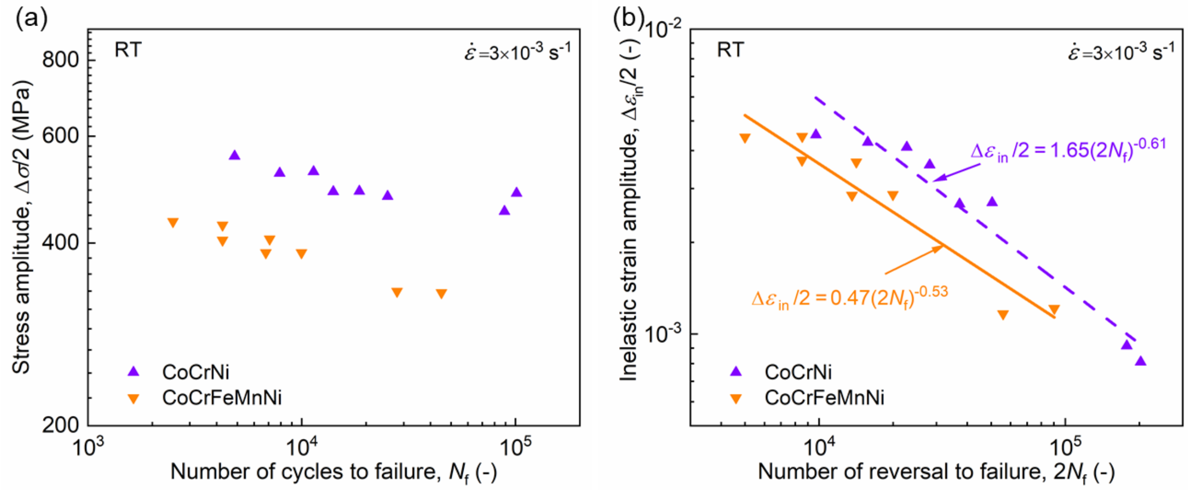

Fig. 5.5: (a) Saturated stress amplitude ($\Delta\sigma/2$) versus number of cycles to failure (N_f), (b) inelastic strain amplitude ($\Delta\varepsilon_{in}/2$) versus number of reversals to failure ($2N_f$) of FG CoCrNi and CoCrFeMnNi [63]. The fitted curves, functions and parameters using the Manson-Coffin law are displayed in (b).

Table 5.2: Values of the fitted parameters obtained from the LCF data for FG CoCrNi and CoCrFeMnNi based on Eq. 3.

Material	Fatigue ductility coefficient, ε'_f	Fatigue ductility exponent, c
CoCrNi	1.66	-0.61
CoCrFeMnNi	0.47	-0.53

5.3 Damage characteristics

The crack growth profile of the CoCrNi sample tested at 0.5% strain amplitude was examined by EBSD. The EBSD data were post-processed into IPF and KAM maps, see Fig. 5.6a-b. Generally, the crack propagates predominantly in a transgranular mode, along with minor intergranular mode (Fig. 5.6a). The KAM map indicates relatively higher KAM values (*i.e.*, higher GNDs density) in the regions neighboring the crack flanks (Fig. 5.6b). This represents that the plastic deformation is accommodated by the emission of dislocations at the crack tip upon cyclic loading.

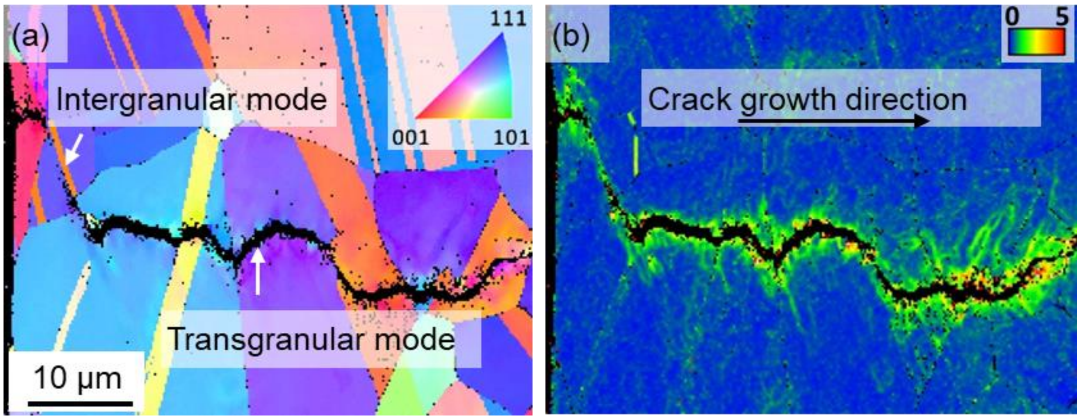

Fig. 5.6: EBSD scan of fatigue crack growth profile for CoCrNi tested at 0.5% strain amplitude.

Fig. 5.7 shows typical fracture surface of a CoCrNi sample tested at 0.5% strain amplitude. The fracture morphology reveals crack initiation from the surface and primarily transgranular crack growth mode. The growth region is covered by striations due to crack-tip blunting and resharpening. Besides, the micro-particles are also found in CoCrNi and proved to be Cr-enriched oxides (not shown here). The above observations for CoCrNi are generally in line with that obtained by fatigue crack propagation tests [26] and similar to that in CoCrFeMnNi alloy (see Section 4.3).

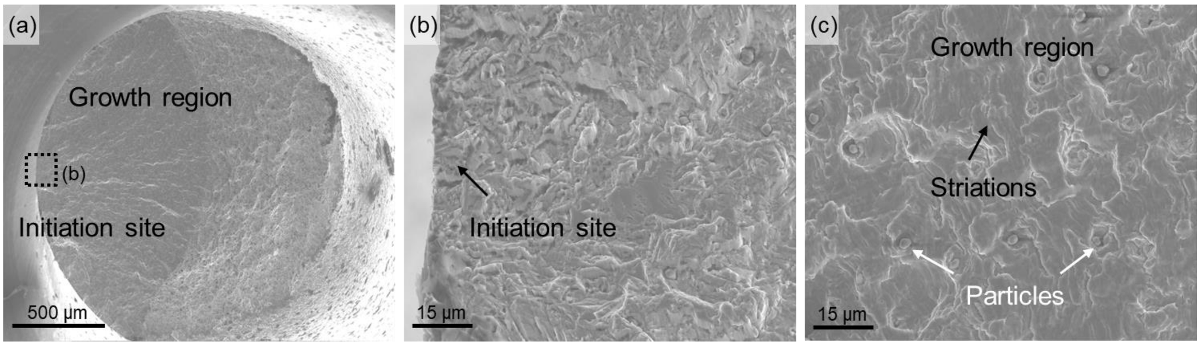

Fig. 5.7: SEM micrographs revealing fracture surface morphologies of CoCrNi tested under 0.5% strain amplitudes at RT.

Though fracture morphologies of the two materials remain similar, the fatigue crack growth threshold ΔK_{TH} of CoCrNi has been reported to be higher than that of CoCrFeMnNi [22, 26]. Specifically, at RT and similar grain size of ~ 7 μm, the ΔK_{TH} of CoCrNi and CoCrFeMnNi is 5.7 MPa√m [26] and 4.8 MPa√m [22], respectively. This indicates that CoCrNi shows higher fatigue crack propagation resistance, which is mainly ascribed to its greater strength and ductility.

5.4 Microstructural evolution

Fig. 5.8 provides a representative IPF map of post-fatigued CoCrNi tested at medium strain amplitude of 0.5%. Upon comparison with the as-recrystallized states (Fig. 5.1a), the alloy exhibits no noticeable changes of texture, grain size and annealing twin fraction after fatigue tests. However, detailed TEM investigations reveal a high density of dislocations with distinct structures, see Fig. 5.9.

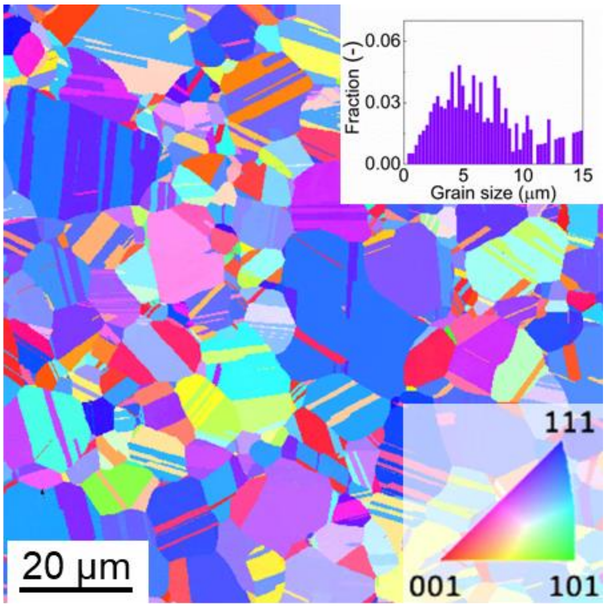

Fig. 5.8: IPF map in the post-fatigued CoCrNi sample tested at 0.5% strain amplitude [63]. The grain size distribution was provided in the inset.

Upon cycling at 0.5% strain amplitude, typical dislocation structures in CoCrNi include stacking faults (SFs), slip bands (SBs), tangles and ill-defined dislocation walls or vein-like substructures (see Fig. 5.9). Out of all, SFs and SBs, along with their debris, are the most prominent structures observed (see Fig. 5.9a-d). In several grains, SFs and SBs are extended on different slip planes, *e.g.*, see marked A, B, C and D in Fig. 5.9a. When edge-on, SBs appear as straight parallel dislocation configurations (see Fig. 5.9b). Besides, most individual dislocations present in the SB are found to be dissociated into Shockley partials with in-between SFs (see Fig. 5.9c-d). Furthermore, dislocations also appear to have interacted on multiple slip systems and formed tangled structures (see Fig. 5.9e). Finally, ill-organized dislocation vein-like substructures were sporadically observed (see Fig. 5.9f). Additionally, careful observations revealed that no deformation twins formed upon cycling.

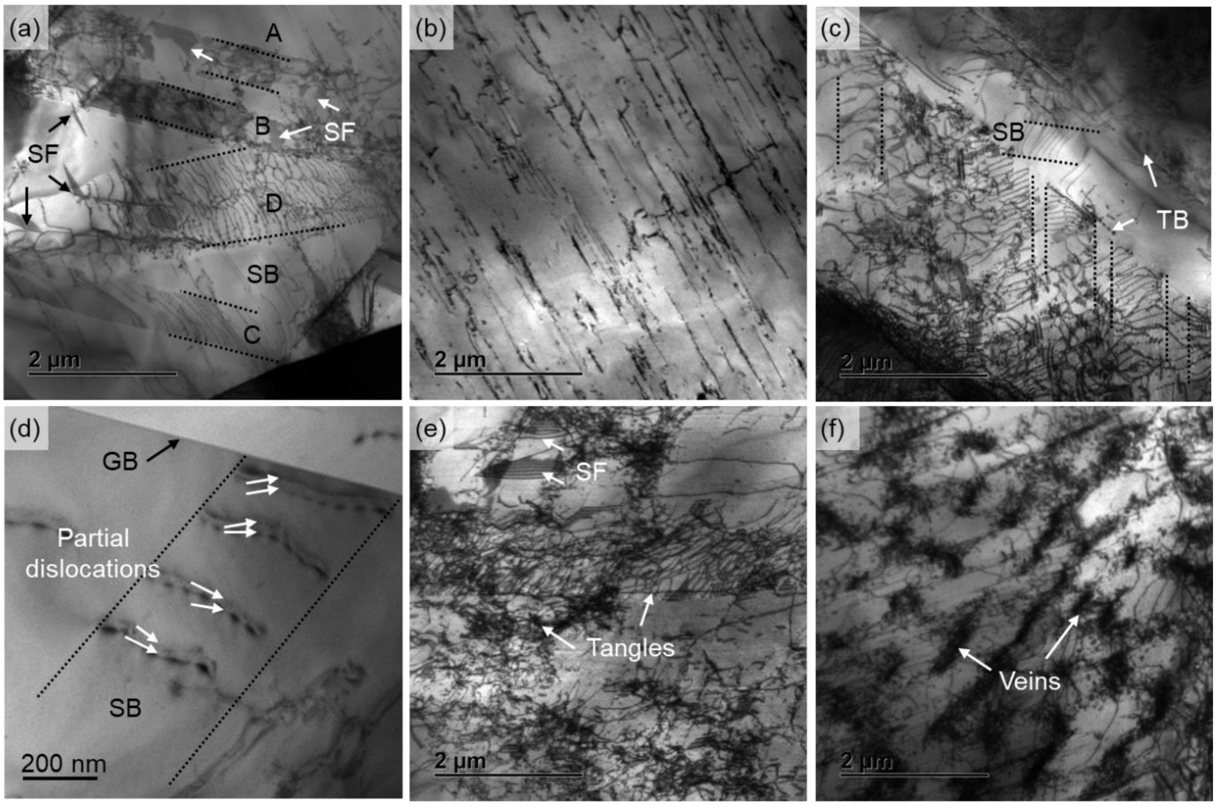

Fig. 5.9: BF-TEM micrographs of post-fatigued CoCrNi tested at 0.5% strain amplitude and RT revealing typical dislocation structures, including (a-c) stacking faults (SFs) and slip bands (SBs) [63]. (b) Edge-on SBs appear as straight parallel dislocation configurations. (c-d) Interactions of SB with annealing twin boundary (TB) and grain boundary (GB). (d) Observed individual dislocations in SBs are dissociated into Shockley partials that are highlighted with pairs of arrows. (e) Dislocation tangles and SFs, and (f) sporadically observed ill-organized dislocation walls or veins-like substructures.

5.5 Discussion

5.5.1 Deformation mechanisms

By comparing the microstructure features between the CoCrNi (Fig. 5.9) and CoCrFeMnNi (Fig. 4.14) at the same 0.5% strain amplitude, their distinct dislocation structures provide insights into the reason for the difference in their LCF resistance.

In CoCrFeMnNi, the localized low-energy dislocation substructures (*e.g.*, walls, veins and/or cells, Fig. 4.14) are more dominantly observed in CoCrFeMnNi, as compared to CoCrNi (Fig. 5.9). This is because of the CoCrFeMnNi comparatively higher SFE (*e.g.*, (30 ± 5) mJ/m^2 [40]) than the latter (*e.g.*, (22 ± 4) mJ/m^2 [12]). The higher SFE facilitates partial dislocations easier constriction into full dislocations and allows the screw parts to undergo cross slip. Therefore, extensive cross slip contributes to the formation of substructures in CoCrFeMnNi. These localized dislocation substructures are associated with the development of extrusions and intrusions on the specimen's surface, where fatigue cracks are known to nucleate [48, 54].

In contrast, due to the relatively lower SFE, the constriction of partial dislocations in CoCrNi is retarded, which reduces the propensity of dislocations cross slip and rearrangement [41]. Therefore, CoCrNi alloy mainly manifests planar dislocation structures (*i.e.*, SBs and SFs, Fig. 5.9), by which dislocations can undergo more reversible movement upon forward and reverse loading. This could explain the higher cumulative inelastic strain (Fig. 5.10a) in CoCrNi compared to CoCrFeMnNi, originating from the former's longer fatigue life. In addition, due to the longer life and larger stress, the total dissipated inelastic strain energy (calculated as the sum of the area of the hysteresis loop to failure, see Fig. 5.10b) is also higher in CoCrNi than CoCrFeMnNi.

Therefore, these planar structures delayed deformation localization in CoCrNi, in comparison to the dislocation substructures in CoCrFeMnNi. In this context, the relatively uniform deformation in CoCrNi could postpone both fatigue crack initiation and propagation process, leading to its superior LCF resistance. The hindered crack propagation process also supports a previous conclusion that CoCrNi alloy exhibits higher fatigue crack propagation resistance compared to CoCrFeMnNi [26]. Taken together, this comparison suggests that reducing SFE results in a transition from wavy slip to planar slip, giving rise to superior fatigue performance for MPEAs.

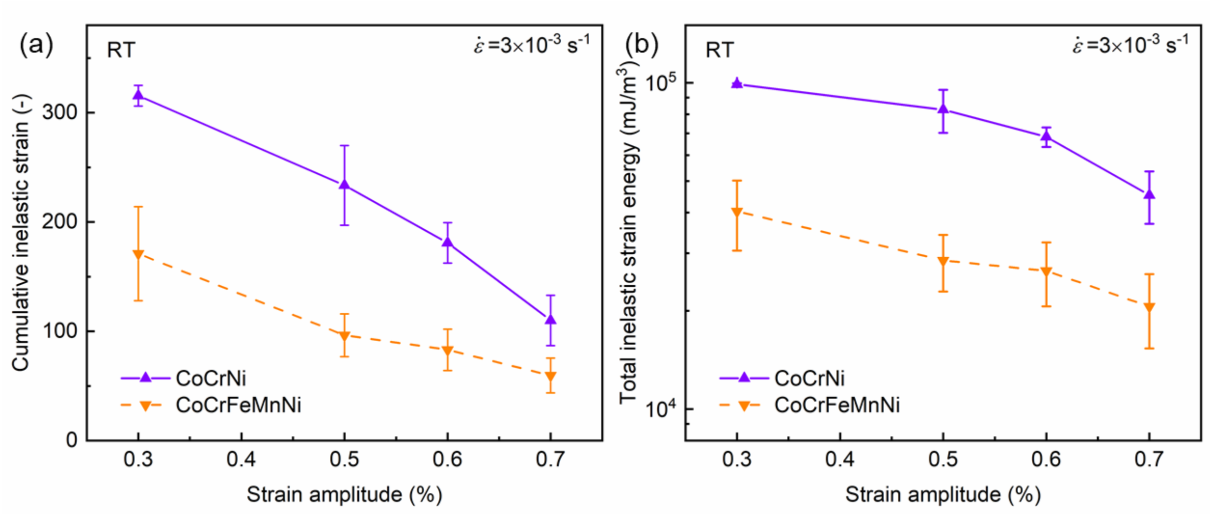

Fig. 5.10: Comparison of (a) cumulative inelastic strain (*i.e.*, $\varepsilon_{cum} = 2 \cdot \Delta\varepsilon_{in} \cdot N_f$) and (b) total inelastic strain energy (calculated as the sum of the area of the hysteresis loop) to failure between CoCrNi and CoCrFeMnNi at different strain amplitudes. The lines are guidelines to the eye, only.

5.5.2 Relation of cyclic stress response to microstructural evolution

Similar to that in CoCrFeMnNi (see Section 4.5.1.2), the cyclic stress response of CoCrNi can also be related to the microstructural evolution. Upon initial cycles' loading, grain-to-grain misorientations (*i.e.*, plastic strain incompatibilities between grains) result in a significant increase in dislocation density close to the grain boundaries. Upon further cycling, as dislocations multiply and spread across grains, they interact with each other and solutes, leading to cyclic hardening. For CoCrNi, additional interactions between dislocations and SFs as well as SBs (that form concurrently) also contribute to the cyclic hardening.

At the subsequent stage, for CoCrFeMnNi alloy, the softening is rationalized by dislocations annihilation and rearrangement into low-energy substructures (*i.e.*, cells and walls). These substructures were found to form at the softening stage (*e.g.*, 500 cycles, see Fig. 4.14) and introduce increased free path for mobile dislocations. For

CoCrNi alloy, the sporadically observed weak-defined wall/vein-like substructures (Fig. 5.9f) may contribute to the softening. Interestingly, these substructures imply activated cross slip in the CoCrNi alloy. This may be not in line with its low SFE, which is supposed to hinder partial dislocations constriction and cross slip. Thus, more detailed investigations are needed to uncover when and how these substructures formed in the CoCrNi alloy.

Following the softening stage, dislocation multiplication and annihilation reach quasi-equilibrium. Therefore, no significant change in dislocation densities or structures leads to quasi-stable cyclic response (*i.e.*, near-steady state) until failure.

5.5.3 Role of deformation twinning and short-range ordering

The absence of deformation twinning (DT) in the present CoCrNi alloy can be explained by the fact that the critical stress required for the onset of twinning (CTS) has not been reached upon cycling. Indeed, for CoCrNi, the CTS was reported to be (740 ± 45) MPa for similar grain sizes (~ 16 μm) [12]. Since the maximum peak stress experienced by the present CoCrNi alloy is around ~ 610 MPa (at the 0.7% stain amplitude), it is reasonable that no DT was activated herein. Thus, the DT did not play a noticeable role in the present material.

Interestingly, a recent work by Heczko et al. [151] revealed the DT in the fatigued CoCrNi alloy. This discrepancy could be attributed to their material's larger grain size (~ 21 μm) as compared to the present CoCrNi alloy (with grain size of ~ 6 ± 3 μm). It is well-accepted that the CTS decreases with increasing grain size, following a Hall-Petch type relationship [105]. Therefore, the larger grain size contributes to a lower CTS value in their investigated CoCrNi alloy, leading to the easier activation of DT in their material, compared to the present CoCrNi alloy.

Additionally, the degree of short-range ordering (SRO) in MPEAs has attracted increasing interest. For CoCrNi, the presence of SRO has only been observed after prolonged annealing at 1000 °C for 120 h, followed by slow furnace-cooling [106]. In the present study, the heat treatments carried out are of a shorter duration (1 h). More importantly, all samples are quenched to RT. Hence, it could be concluded that the

SRO in the present CoCrNi is most likely either nonexistent or negligible. Therefore, SRO did not play a noticeable role in the cyclic response of this material.

5.6 Summary

This chapter investigated the LCF behavior and deformation mechanisms of CoCrNi alloy at room temperature and compared that to that of CoCrFeMnNi alloy. The following conclusions can be drawn from the present chapter:

- CoCrNi shows initial hardening followed by softening and a near-steady state until failure, which is similar to CoCrFeMnNi. The majority of lifetime (~ 90%) is represented by the near-steady state.

- In comparison to CoCrFeMnNi, CoCrNi exhibits higher cyclic strength, lower inelastic strain, and longer lifetime for the same strain amplitude.

- In contrast to the well-defined wavy dislocations substructures (*i.e.*, veins and/or cells-like structures) in CoCrFeMnNi, post-fatigued CoCrNi manifested planar dislocation structures (including SBs and SFs). The planar slip in CoCrNi alloy is mainly ascribed to its lower SFE that facilitates dissociation of full dislocations into partial dislocations.

- Compared to the wavy substructures in CoCrFeMnNi, pronounced planar slip in CoCrNi delays deformation localization, leading to its superior fatigue crack initiation and propagation resistance. Thus, it is suggested that reducing the SFE of MPEAs is an effective strategy to improve their fatigue resistance.

- Investigations on fracture surfaces and crack paths of CoCrNi indicate that fatigue crack initiates from the surface, and propagates in a predominantly transgranular mode. This behavior is similar to that of CoCrFeMnNi. Nevertheless, CoCrNi shows higher crack initiation and propagation resistance.

6 Comparisons to a conventional steel and dual-phase MPEAs

To identify the features contributing to peculiar fatigue properties of MPEAs, this chapter compares the LCF response of CoCrFeMnNi to a conventional FCC steel. Afterwards, to further explore strategies for enhancing fatigue properties of MPEAs, the LCF data of current FCC MPEAs are compared to dual-phase MPEAs.

6.1 Comparison to a conventional steel

For CoCrFeMnNi, with increasing strain amplitude upon cycling, the typical dislocation structures changed from slip bands to well-defined substructures (Section 4.5.1.1). This observation is similar to that observed for a 316L austenitic steel [97, 152]. Likewise, these two materials show similar cyclic stress response (*i.e.*, cyclic hardening followed by softening and near-steady state [153]).

These similarities can be rationalized by their comparable SFEs (CoCrFeMnNi: 30 ± 5 mJ/m^2 [40] and 316L steel: ~ 28 mJ/m^2 [154]), as it is known to strongly influence dislocations slip mode [63, 69]. Based on this comparison, it could be anticipated that such dislocation evolution and cyclic stress response are also applicable for other FCC MPEAs with similar SFEs.

Considering these similarities between the 316L steel and CoCrFeMnNi, the comparison of their detailed fatigue response is of importance. Fig. 6.1 presents their hysteresis loops of two typical cycles (*i.e.*, 2nd and 31st cycles) tested at RT under 0.7% strain amplitude. The 2nd and 31st cycles are chosen as they represent the beginning of cyclic hardening and softening stages, respectively, for both materials [86, 153]. Note that these two materials have similar average grain sizes (of ~ 60 μm) and insignificant texture, which could rule out the influences of grain size and texture on the comparison.

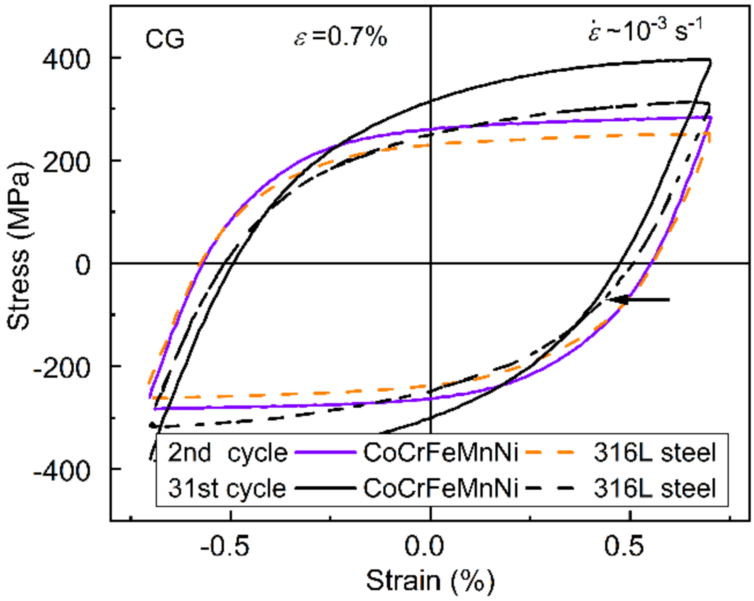

Fig. 6.1: Hysteresis loops of two typical cycles (*i.e.*, the 2nd and 31st cycles) for CG CoCrFeMnNi and 316L steel (of average grain sizes ~ 60 μm [153]), which are tested at RT under 0.7% strain amplitude [86].

As evident, at the 2nd cycle, both materials show similar inelastic strain (*i.e.*, half-width of hysteresis loops at zero stress in Fig. 6.1). At the 31st cycle, due to cyclic hardening, both materials exhibit a decrease in inelastic strain. However, CoCrFeMnNi shows a lower inelastic strain at the 31st cycle than 316L steel. Furthermore, the lower inelastic strain in CoCrFeMnNi results from its higher cyclic strength (see peak stresses at the 31st cycle in Fig. 6.1), stemming from its larger solid solution strengthening and grain boundary strengthening than 316L steel. This lower inelastic strain of CoCrFeMnNi than 316L steel is expected to hold during the whole near-steady state, which takes up the majority of lifetime for both materials. Therefore, it is anticipated that CoCrFeMnNi has a longer lifetime than 316L steel at the same total strain and stress conditions.

Together, this comparison suggests that CoCrFeMnNi or its subsets with higher strength and sufficient ductility could be good candidates with better LCF resistance, as compared to conventional FCC steels (*e.g.*, 316L steel) in safety-critical engineering applications. For more accurate comparison on their lifetime, LCF tests of the same sample size would be needed for 316L steel, which is beyond the scope of this work.

6.2 Comparisons to dual-phase MPEAs

The earlier comparison between FCC CoCrNi and CoCrFeMnNi has suggested that reducing the SFE could be an effective strategy for improving the fatigue resistance of MPEAs (Section 5.5.1). To explore other potential strategies, the LCF data of the present FCC MPEAs were compared to dual-phase MPEAs (with FCC matrix and embedded BCC precipitates), such as $Al_{0.5}$CoCrFeMnNi [155] and $Al_{0.5}$CoCrFeNi [76]).

The Wöhler and Manson-Coffin curves of these materials are shown in Fig. 6.2a-b. Note that these materials have similar FCC grain sizes (~ 5−9 μm) and insignificant texture. Thus, the grain size and texture effects on the LCF performance could be neglected, ensuring reasonably fair comparisons.

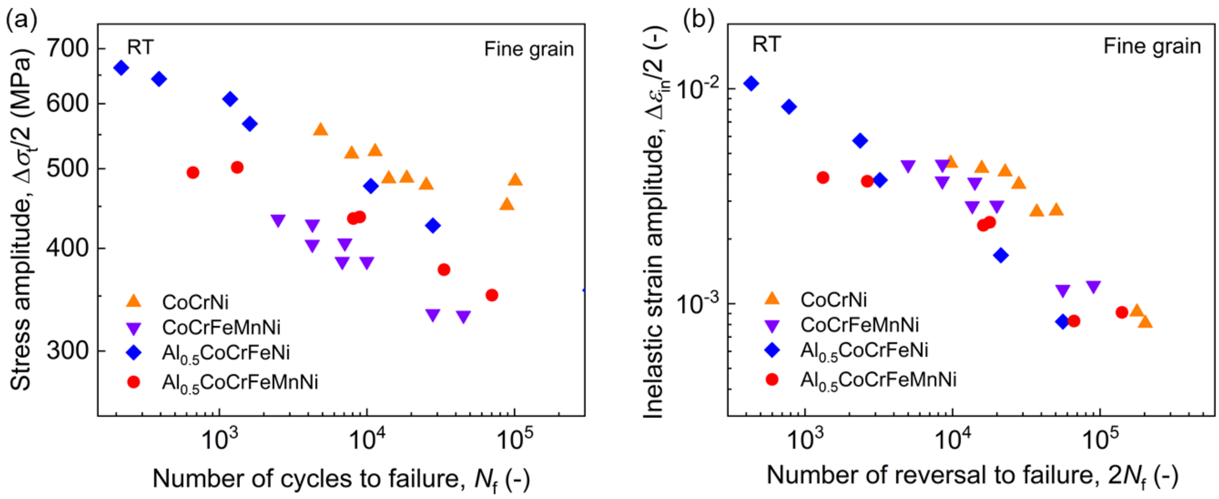

Fig. 6.2: Comparison of fatigue life including (a) Wöhler and (b) Manson-Coffin curves for four different MPEAs, including FCC CoCrNi and CoCrFeMnNi, as well as dual-phase $Al_{0.5}$CoCrFeMnNi [155] and $Al_{0.5}$CoCrFeNi [76].

Firstly, the data of FCC CoCrFeMnNi (in *purple*) were compared to dual-phase $Al_{0.5}$CoCrFeMnNi (in *red*). For a given stress amplitude (Fig. 6.2a), the $Al_{0.5}$CoCrFeMnNi exhibits longer lifetime than CoCrFeMnNi, indicating the former's higher cyclic stress resistance. For a given $\Delta\varepsilon_{in}/2$ (Fig. 6.2b), the data for $Al_{0.5}$CoCrFeMnNi and CoCrFeMnNi almost lies on top of each other at low and medium strain amplitudes (0.3% and 0.5%), indicating their comparable cyclic strain-amplitude resistance. This comparison suggests that introducing dual-phase microstructure for

FCC MPEAs is an effective method to enhance cyclic stress resistance, meanwhile maintaining comparable cyclic strain resistance at low-to-medium strain amplitudes (0.3% and 0.5%). The reason is related to the fact that the dual-phase MPEA possesses additional precipitate hardening, preserving sufficient ductility compared to FCC MPEAs [155]. Nevertheless, at high strain amplitude (0.7%), $Al_{0.5}CoCrFeMnNi$ shows shorter life than CoCrFeMnNi (Fig. 6.2b). This appears to originate from earlier crack initiation from phase boundaries at high strain amplitudes (for more details, see Ref. [155]).

Secondly, the data of FCC CoCrNi (in *orange*) were compared to dual-phase $Al_{0.5}CoCrFeNi$ (in *blue*) [76] and $Al_{0.5}CoCrFeMnNi$ (in *red*), see Fig. 6.2. In general, the CoCrNi exhibits the longest lifetime upon comparison to both $Al_{0.5}CoCrFeMnNi$ and $Al_{0.5}CoCrFeNi$, suggesting its highest cyclic stress and strain resistance. The reason can be ascribed to 1) larger solid solution strengthening (due to larger mean atomic displacement as a result of higher Cr percentage) [6], and 2) relatively uniform deformation (owing to lower SFE which promotes planar slip, see Section 5.5.1).

The *last* comparison was made between the two dual-phase MPEAs. For a given stress condition in Fig. 6.2a, the $Al_{0.5}CoCrFeMnNi$ (in *red*) exhibits a shorter life compared to $Al_{0.5}CoCrFeNi$ (in *blue*). For a given inelastic strain amplitude in Fig. 6.2b, the data of both $Al_{0.5}CoCrFeMnNi$ and $Al_{0.5}CoCrFeNi$ almost lie on top of each other, despite experimental scatter. The higher stress resistance of $Al_{0.5}CoCrFeNi$ may also originate from its higher Cr percentage, which leads to larger solid solution strengthening, as compared to the $Al_{0.5}CoCrFeMnNi$ alloy.

Together, these comparisons imply that introducing dual-phase microstructure, reducing the SFE of FCC phase and increasing Cr percentage (*e.g.*, $Al_xCoCrNi$ system) are effective strategies to further improve the LCF performance of MPEAs.

6.3 Summary

- By comparing to a 316L steel, CoCrFeMnNi is expected to show a longer lifetime due to the lower inelastic strain at each cycle. This suggests that CoCrFeMnNi MPEA or its subsets with higher strength (stemming from higher solid solution strengthening and grain boundary strengthening) and sufficient ductility (due to their similar SFEs) could provide enhanced LCF resistance, as compared to conventional FCC steels.

- By comparing the LCF data of present FCC MPEAs to those of dual-phase $Al_{0.5}CoCrFeMnNi$ and $Al_{0.5}CoCrFeNi$ MPEAs, it is suggested that introducing dual-phase microstructures, reducing the SFE of FCC phase and increasing Cr percentage (*e.g.*, $Al_xCoCrNi$ system) are effective strategies for tailoring MPEAs with enhanced fatigue resistance.

7 Summary and outlook

7.1 Summary

Conventional alloys based on one or two principal elements have shown a limit for achieving excellent combined mechanical properties. Multi-principal element alloys (MPEAs) provide a huge opportunity for the material science community to explore materials with promising combinations of mechanical properties. Currently, primary focus has been put on understating the MPEAs monotonic deformation behavior, with their cyclic deformation behavior yet to be addressed. Therefore, this work is designed to showcase the low-cycle fatigue (LCF) behavior of two model MPEAs, namely CoCrFeMnNi and CoCrNi alloys.

7.1.1 LCF behavior of CoCrFeMnNi alloy

The LCF responses including cyclic stress response and lifetime were obtained by performing fatigue-tests for the CoCrFeMnNi (with two distinct grain sizes, ~ 6 μm and ~ 60 μm) at different strain amplitudes and temperatures (RT and 550 °C). The operating cyclic deformation mechanisms (with emphasis on the influences of *temperature*, *grain size, cycle number*, *strain amplitude*, and *grain orientation*) were elucidated by extensive TEM investigations.

On one hand, at ***RT***, the CoCrFeMnNi manifests initial cyclic hardening followed by softening and near-steady state before failure. Fatigue results indicate that reducing *grain size* leads to enhanced LCF lifetime for a given total stress and strain amplitude. Nevertheless, for a given inelastic strain amplitude, reducing *grain size* has no significant effect on the lifetime at the investigated *grain size* range.

TEM investigations reveal that, at RT, increasing ***cycle number*** leads to dislocation structures transition from initial slip bands (and tangles) to ill-defined dislocation substructures (*i.e.*, veins, cells, walls separated by channels), finally to their well-defined versions. The channels are believed to originate from extensive annihilation of screw dislocations. This confirms that cross/wavy slip contributes to the dislocation substructure formation. Therefore, the microstructural evolution with *cycle number* reflects dislocation slip mode transition from initially planar slip to wavy slip. Equally importantly, this evolution can be linked well with the observed cyclic stress response: cyclic hardening (dislocations multiplication) followed by softening (substructures formation) and near-steady state (quasi-stabilized dislocation density and configuration). Moreover, dislocations in substructures (*i.e.*, veins, walls, and cells) are proven to have different Burgers vectors. This indicates that, apart from the wavy slip, multiple slip also contributes to dislocation substructures formation.

Further TEM investigations demonstrate that dislocation structure mainly consisted of planar slip bands at low ***strain amplitude*** (0.3%); while at larger *strain amplitudes* (0.5% and 0.7%), dislocation substructures including veins, walls, labyrinth, and cells prevailed. This represents that, with increasing *strain amplitude* at RT, dislocation slip mode changes from planar slip to wavy slip, due to multiple slip activation (including cross/wavy slip) at higher *strain amplitude*.

Further analyses show that, dislocation structure in polycrystalline CoCrFeMnNi is dictated more by the constraints from neighboring grains rather than ***grain orientation***. In addition, various dislocation structures (*e.g.*, walls and cells) were observed in a single grain, which is also rationalized by the constraint effects from the neighboring grains.

On the other hand, at ***550 °C***, the CoCrFeMnNi exhibits initial cyclic hardening followed by a near-steady state until failure. Upon comparison to RT, the cyclic response exhibits temperature dependence, *i.e.*, absence of cyclic softening, presence of serrated flow and reduction in lifetime at 550 °C.

TEM studies reveal that, at 550 °C, with increasing ***cycle number***, the slip mode remains planar slip at low strain amplitudes (0.2% and 0.3%); whereas it changes from initially planar slip to coexisting planar slip and wavy slip at medium-to-high strain amplitudes (0.5% and 0.75%). The planar slip at medium-to-high strain amplitudes is rather unexpected and arises from the increase of the stacking fault width (likely originating from Suzuki segregation). This Suzuki segregation partly restricts cross/wavy slip at 550 °C. The presence of planar slip relatively reduced cross slip and consequently limited substructures explained well the absence of cyclic softening.

Moreover, the coexisting planar slip can be linked with the observed serrated flow, which is interpreted by the interactions between planar mobile dislocations and solute atoms. Further TEM investigations show chemical segregation (in the form of Cr- and NiMn-enriched secondary phases) near grain boundaries. The formation of these phases could be considered as evidence of elemental diffusion, which is responsible for the increased stacking fault width and serrated flow in CoCrFeMnNi at 550 °C.

7.1.2 LCF behavior of CoCrNi alloy

The LCF behavior of CoCrNi alloy was investigated by performing fatigue-tests at RT under different strain amplitudes and compared to CoCrFeMnNi alloy. The underlying deformation mechanisms were clarified by TEM characterizations.

Similar to CoCrFeMnNi, CoCrNi shows initial hardening followed by softening and a near-steady state until failure. Differently, CoCrNi exhibits higher cyclic strength, lower inelastic strain, and longer lifetime at the same strain amplitude.

In contrast to the wavy-substructures (*i.e.*, veins walls and cells separated by channels) prevailing in CoCrFeMnNi, CoCrNi mainly exhibits planar dislocation structures (including slip bands and stacking faults). The planar slip in CoCrNi alloy is mainly ascribed to its lower stacking fault energy (SFE), as lower SFE facilitates dissociation of full dislocations into partial dislocations, which hinders dislocation cross slip. In comparison to prevalent wavy slip in CoCrFeMnNi, the pronounced planar slip in CoCrNi delays deformation localization, leading to its superior fatigue resistance. This suggests that reducing SFE is an effective method to enhance fatigue resistance of MPEAs.

Investigations on fracture surfaces and crack growth profiles for CoCrFeMnNi and CoCrNi revealed their damage mechanisms. In specific, both alloys manifest crack initiation from sample surfaces and predominant transgranular crack growth behavior. Nevertheless, the CoCrNi exhibits higher crack initiation and propagation resistance compared to CoCrFeMnNi, due to the former’s planar slip behavior.

7.1.3 Comparisons to a conventional steel and dual-phase MPEAs

To identify the potential peculiarity of MPEAs and explore strategies for improving their fatigue resistance, LCF data of present FCC MPEAs were compared to a conventional FCC steel (*i.e.*, 316L steel) and dual-phase MPEAs (*i.e.*, $Al_{0.5}$CoCrFeMnNi and $Al_{0.5}$CoCrFeNi).

By comparing to a 316L steel, CoCrFeMnNi likely shows longer lifetime for the same strain amplitude. This is related to the lower inelastic strain at each cycle experienced by CoCrFeMnNi, due to its larger strength (stemming from solid solution and grain boundary strengthening) than conventional FCC steels. This suggests that CoCrFeMnNi MPEA or its subsets with larger strength and sufficient ductility (due to low-to-medium SFE) could provide enhanced LCF resistance, as compared to conventional FCC steels.

By further comparing to $Al_{0.5}$CoCrFeMnNi and $Al_{0.5}$CoCrFeNi dual-phase MPEAs, this work suggests that introducing dual-phase microstructures (*i.e.*, FCC matrix and BCC precipitates), reducing SFE and enhancing Cr percentage are effective strategies to tailor MPEAs with enhanced fatigue resistance.

In sum, this work characterized the LCF behavior of FCC CoCrFeMnNi and CoCrNi model MPEAs (including comparisons to a conventional FCC steel and dual-phase MPEAs), and uncovered the microstructural origins of their behavior. Thus, this work not only serves as a reference system to advance the understanding of the cyclic deformation mechanisms for FCC MPEAs, but also proposes strategies for enhancing fatigue resistance of MPEAs.

7.2 Outlook

Despite the above findings captured in this thesis, further efforts are needed in the following aspects.

- This work revealed that, for CoCrFeMnNi, dislocation-rich regions (*i.e.*, veins, walls and cells) are composed of dislocations from multiple slip systems. This observation differs from the previous finding that dislocation walls mainly consist of dislocations from primary slip systems [94]. To further unravel the detailed role of multiple slip, discrete dislocation dynamics modeling and fatigue studies on single crystals could be beneficial.

- This work compared the LCF response between CoCrFeMnNi and 316L steel, with the data of 316L steel cited from Ref. [153]. This comparison may involve sample size influence on the LCF response. Thus, for a more comprehensive comparison, LCF tests for the 316L steel with the same sample size are required.

- This work demonstrated the cyclic deformation mechanisms of CoCrNi alloy mainly tested at 0.5% strain amplitude. As the underlying deformation mechanisms vary with testing parameters (such as temperature, strain amplitude and cycle number), it is of significance to further examine how these parameters affect the deformation mechanisms (*e.g.*, dislocation structures) of CoCrNi alloy.

Bibliography

[1] Y.F. Ye, Q. Wang, J. Lu, C.T. Liu, Y. Yang, High-entropy alloy: challenges and prospects, Materials Today, 19 (2016) 349-362.

[2] B. Cantor, I.T.H. Chang, P. Knight, A.J.B. Vincent, Microstructural development in equiatomic multicomponent alloys, Materials Science and Engineering: A, 375-377 (2004) 213-218.

[3] E.P. George, W.A. Curtin, C.C. Tasan, High entropy alloys: A focused review of mechanical properties and deformation mechanisms, Acta Materialia, 188 (2020) 435-474.

[4] D.B. Miracle, O.N. Senkov, A critical review of high entropy alloys and related concepts, Acta Materialia, 122 (2017) 448-511.

[5] M.-H. Tsai, J.-W. Yeh, High-Entropy Alloys: A Critical Review, Materials Research Letters, 2 (2014) 107-123.

[6] F.G. Coury, G. Zepon, C. Bolfarini, Multi-Principal Element Alloys from the CrCoNi Family: Outlook and Perspectives, Journal of Materials Research and Technology, 15 (2021) 3461-3480.

[7] B. Gludovatz, A. Hohenwarter, D. Catoor, E.H. Chang, E.P. George, R.O. Ritchie, A fracture-resistant high-entropy alloy for cryogenic applications, Science, 345 (2014) 1153-1158.

[8] B. Gludovatz, A. Hohenwarter, K.V. Thurston, H. Bei, Z. Wu, E.P. George, R.O. Ritchie, Exceptional damage-tolerance of a medium-entropy alloy CrCoNi at cryogenic temperatures, Nat Commun, 7 (2016) 10602.

[9] Z. Wu, H. Bei, G.M. Pharr, E.P. George, Temperature dependence of the mechanical properties of equiatomic solid solution alloys with face-centered cubic crystal structures, Acta Materialia, 81 (2014) 428-441.

[10] F. Otto, A. Dlouhý, C. Somsen, H. Bei, G. Eggeler, E.P. George, The influences of temperature and microstructure on the tensile properties of a CoCrFeMnNi high-entropy alloy, Acta Materialia, 61 (2013) 5743-5755.

[11] A.S. Tirunilai, T. Hanemann, C. Reinhart, V. Tschan, K.P. Weiss, G. Laplanche, J. Freudenberger, M. Heilmaier, A. Kauffmann, Comparison of cryogenic deformation of the concentrated solid solutions CoCrFeMnNi, CoCrNi and CoNi, Materials Science and Engineering: A, 783 (2020) 139290.

[12] G. Laplanche, A. Kostka, C. Reinhart, J. Hunfeld, G. Eggeler, E.P. George, Reasons for the superior mechanical properties of medium-entropy CrCoNi compared to high-entropy CrMnFeCoNi, Acta Materialia, 128 (2017) 292-303.

[13] J. Miao, C.E. Slone, T.M. Smith, C. Niu, H. Bei, M. Ghazisaeidi, G.M. Pharr, M.J. Mills, The evolution of the deformation substructure in a Ni-Co-Cr equiatomic solid solution alloy, Acta Materialia, 132 (2017) 35-48.

[14] Z. Wu, Y. Gao, H. Bei, Thermal activation mechanisms and Labusch-type strengthening analysis for a family of high-entropy and equiatomic solid-solution alloys, Acta Materialia, 120 (2016) 108-119.

[15] J. Schijve, Fatigue of structures and materials, Springer Netherlands, Dordrecht, 2001.

[16] S. Suresh, Fatigue of materials, Cambridge university press, Cambridge, 1998.

[17] A. Chauhan, D. Litvinov, J. Aktaa, High temperature tensile properties and fracture characteristics of bimodal 12Cr-ODS steel, Journal of Nuclear Materials, 468 (2016) 1-8.

[18] A. Chauhan, D. Litvinov, J. Aktaa, Deformation and damage mechanisms of a bimodal 12Cr-ODS steel under high-temperature cyclic loading, International Journal of Fatigue, 93 (2016) 1-17.

[19] C.W. Shao, P. Zhang, R. Liu, Z.J. Zhang, J.C. Pang, Q.Q. Duan, Z.F. Zhang, A remarkable improvement of low-cycle fatigue resistance of high-Mn austenitic TWIP alloys with similar tensile properties: Importance of slip mode, Acta Materialia, 118 (2016) 196-212.

[20] J. Nellessen, S. Sandlöbes, D. Raabe, Effects of strain amplitude, cycle number and orientation on low cycle fatigue microstructures in austenitic stainless steel studied by electron channelling contrast imaging, Acta Materialia, 87 (2015) 86-99.

[21] F.D. León-Cázares, R. Schlütter, T. Jackson, E.I. Galindo-Nava, C.M.F. Rae, A multiscale study on the morphology and evolution of slip bands in a nickel-based superalloy during low cycle fatigue, Acta Materialia, 182 (2020) 47-59.

[22] K.V.S. Thurston, B. Gludovatz, A. Hohenwarter, G. Laplanche, E.P. George, R.O. Ritchie, Effect of temperature on the fatigue-crack growth behavior of the high-entropy alloy CrMnFeCoNi, Intermetallics, 88 (2017) 65-72.

[23] Y.-K. Kim, G.-S. Ham, H.S. Kim, K.-A. Lee, High-cycle fatigue and tensile deformation behaviors of coarse-grained equiatomic CoCrFeMnNi high entropy alloy and unexpected hardening behavior during cyclic loading, Intermetallics, 111 (2019) 106486.

[24] Y.Z. Tian, S.J. Sun, H.R. Lin, Z.F. Zhang, Fatigue behavior of CoCrFeMnNi high-entropy alloy under fully reversed cyclic deformation, Journal of Materials Science & Technology, 35 (2019) 334-340.

[25] Z. Chlup, S. Fintová, H. Hadraba, I. Kuběna, M. Vilémová, J. Matějíček, Fatigue Behaviour and Crack Initiation in CoCrFeNiMn High-Entropy Alloy Processed by Powder Metallurgy, Metals, 9 (2019) 1110.

[26] J. Rackwitz, Q. Yu, Y. Yang, G. Laplanche, E.P. George, A.M. Minor, R.O. Ritchie, Effects of cryogenic temperature and grain size on fatigue-crack propagation in the medium-entropy CrCoNi alloy, Acta Materialia, 200 (2020) 351-365.

[27] R.S. Mishra, R.S. Haridas, P. Agrawal, High entropy alloys – Tunability of deformation mechanisms through integration of compositional and microstructural domains, Materials Science and Engineering: A, 812 (2021) 141085.

[28] F. Otto, Y. Yang, H. Bei, E.P. George, Relative effects of enthalpy and entropy on the phase stability of equiatomic high-entropy alloys, Acta Materialia, 61 (2013) 2628-2638.

[29] K.Y. Tsai, M.H. Tsai, J.W. Yeh, Sluggish diffusion in Co–Cr–Fe–Mn–Ni high-entropy alloys, Acta Materialia, 61 (2013) 4887-4897.

[30] M. Vaidya, K.G. Pradeep, B.S. Murty, G. Wilde, S.V. Divinski, Bulk tracer diffusion in CoCrFeNi and CoCrFeMnNi high entropy alloys, Acta Materialia, 146 (2018) 211-224.

[31] A. Gali, E.P. George, Tensile properties of high- and medium-entropy alloys, Intermetallics, 39 (2013) 74-78.

[32] G. Laplanche, A. Kostka, O. Horst, G. Eggeler, E.P. George, Microstructure evolution and critical stress for twinning in the CrMnFeCoNi high-entropy alloy, Acta Materialia, 118 (2016) 152-163.

[33] A.S. Tirunilai, J. Sas, K.-P. Weiss, H. Chen, D.V. Szabó, S. Schlabach, S. Haas, D. Geissler, J. Freudenberger, M. Heilmaier, A. Kauffmann, Peculiarities of deformation of CoCrFeMnNi at cryogenic temperatures, Journal of Materials Research, 33 (2018) 3287-3300.

[34] S. Sun, Y. Tian, H. Lin, H. Yang, X. Dong, Y. Wang, Z. Zhang, Transition of twinning behavior in CoCrFeMnNi high entropy alloy with grain refinement, Materials Science and Engineering: A, 712 (2018) 603-607.

[35] K. Lu, A. Chauhan, D. Litvinov, A.S. Tirunilai, J. Freudenberger, A. Kauffmann, M. Heilmaier, J. Aktaa, Micro-mechanical deformation behavior of CoCrFeMnNi high-entropy alloy, Journal of Materials Science & Technology, 100 (2022) 237-245.

[36] C. Varvenne, A. Luque, W.A. Curtin, Theory of strengthening in fcc high entropy alloys, Acta Materialia, 118 (2016) 164-176.

[37] S. Lee, M.J. Duarte, M. Feuerbacher, R. Soler, C. Kirchlechner, C.H. Liebscher, S.H. Oh, G. Dehm, Dislocation plasticity in FeCoCrMnNi high-entropy alloy: quantitative insights from in situ transmission electron microscopy deformation, Materials Research Letters, 8 (2020) 216-224.

[38] Z.C. Cordero, B.E. Knight, C.A. Schuh, Six decades of the Hall–Petch effect – a survey of grain-size strengthening studies on pure metals, International Materials Reviews, 61 (2016) 495-512.

[39] G. Laplanche, P. Gadaud, C. Bärsch, K. Demtröder, C. Reinhart, J. Schreuer, E.P. George, Elastic moduli and thermal expansion coefficients of medium-entropy subsystems of the CrMnFeCoNi high-entropy alloy, Journal of Alloys and Compounds, 746 (2018) 244-255.

[40] N.L. Okamoto, S. Fujimoto, Y. Kambara, M. Kawamura, Z.M. Chen, H. Matsunoshita, K. Tanaka, H. Inui, E.P. George, Size effect, critical resolved shear stress, stacking fault energy, and solid solution strengthening in the CrMnFeCoNi high-entropy alloy, Scientific Reports, 6 (2016) 35863.

[41] D. Hull, D.J. Bacon, Introduction to dislocations, Butterworth-Heinemann, Amsterdam, Boston, Heidelberg, London, New York, Paris, San Diego, San Francisco, Singapore, Sydney, Tokyo, 2001.

[42] N. Thompson, Dislocation Nodes in Face-Centred Cubic Lattices, Proceedings of the Physical Society. Section B, 66 (1953) 481.

[43] H. Mughrabi, Microstructural mechanisms of cyclic deformation, fatigue crack initiation and early crack growth, Philos Trans A Math Phys Eng Sci, 373 (2015) 20140132.

[44] F. Ellyin, Fatigue Damage, Crack Growth and Life Prediction, Chapman & Hall, London, Weinheim, New York, Tokyo, Melbourne, Madras, 1997.

[45] Z. Basinski, S. Basinski, Fundamental aspects of low amplitude cyclic deformation in face-centred cubic crystals, Progress in Materials Science, 36 (1992) 89-148.

[46] P. Lukáš, M. Klesnil, J. Krejčí, Dislocations and persistent slip bands in copper single crystals fatigued at low stress amplitude, physica status solidi (b), 27 (1968) 545-558.

[47] U. Essmann, H. Mughrabi, Annihilation of dislocations during tensile and cyclic deformation and limits of dislocation densities, Philosophical Magazine A, 40 (1979) 731-756.

[48] J. Polák, V. Mazánová, M. Heczko, I. Kuběna, J. Man, Profiles of persistent slip markings and internal structure of underlying persistent slip bands, Fatigue & Fracture of Engineering Materials & Structures, 40 (2017) 1101-1116.

[49] S. Lavenstein, Y. Gu, D. Madisetti, J.A. El-Awady, The heterogeneity of persistent slip band nucleation and evolution in metals at the micrometer scale, Science, 370 (2020) eabb2690.

[50] G.M. Castelluccio, D.L. McDowell, Mesoscale cyclic crystal plasticity with dislocation substructures, International Journal of Plasticity, 98 (2017) 1-26.

[51] C.W. Shao, P. Zhang, Y.K. Zhu, Z.J. Zhang, J.C. Pang, Z.F. Zhang, Improvement of low-cycle fatigue resistance in TWIP steel by regulating the grain size and distribution, Acta Materialia, 134 (2017) 128-142.

[52] P. Li, S.X. Li, Z.G. Wang, Z.F. Zhang, Unified factor controlling the dislocation evolution of fatigued face-centered cubic crystals, Acta Materialia, 129 (2017) 98-111.

[53] V. Gerold, H.P. Karnthaler, On the origin of planar slip in f.c.c. alloys, Acta Metallurgica, 37 (1989) 2177-2183.

[54] H. Mughrabi, Cyclic Slip Irreversibilities and the Evolution of Fatigue Damage, Metallurgical and Materials Transactions A, 40 (2009) 1257-1279.

[55] H. Mughrabi, Dislocations in fatigue, Dislocations and properties of real materials, (1984) 244-262.

[56] M.D. Sangid, The physics of fatigue crack initiation, International Journal of Fatigue, 57 (2013) 58-72.

[57] P. Paris, F. Erdogan, A critical analysis of crack propagation laws, Journal of Basic Engineering, 85 (1963) 528-533.

[58] R.O. RITCHIE, Mechanisms of fatigue-crack propagation in ductile and brittle solids, International Journal of Fracture, 100 (1999) 55-83.

[59] K. Suzuki, M. Koyama, S. Hamada, K. Tsuzaki, H. Noguchi, Planar slip-driven fatigue crack initiation and propagation in an equiatomic CrMnFeCoNi high-entropy alloy, International Journal of Fatigue, 133 (2020) 105418.

[60] A.G. Wang, X.H. An, J. Gu, X.G. Wang, L.L. Li, W.L. Li, M. Song, Q.Q. Duan, Z.F. Zhang, X.Z. Liao, Effect of grain size on fatigue cracking at twin boundaries in a CoCrFeMnNi high-entropy alloy, Journal of Materials Science & Technology, 39 (2019) 1-6.

[61] S.A.A. Shams, G. Jang, J.W. Won, J.W. Bae, H. Jin, H.S. Kim, C.S. Lee, Low-cycle fatigue properties of CoCrFeMnNi high-entropy alloy compared with its conventional counterparts, Materials Science and Engineering: A, 792 (2020) 139661.

[62] K. Lu, A. Chauhan, D. Litvinov, M. Walter, A.S. Tirunilai, J. Freudenberger, A. Kauffmann, M. Heilmaier, J. Aktaa, High-temperature low cycle fatigue behavior of an equiatomic CoCrFeMnNi high-entropy alloy, Materials Science and Engineering: A, 791 (2020) 139781.

[63] K. Lu, A. Chauhan, M. Walter, A.S. Tirunilai, M. Schneider, G. Laplanche, J. Freudenberger, A. Kauffmann, M. Heilmaier, J. Aktaa, Superior low-cycle fatigue properties of CoCrNi compared to CoCrFeMnNi, Scripta Materialia, 194 (2021) 113667.

[64] S. Picak, T. Wegener, S.V. Sajadifar, C. Sobrero, J. Richter, H. Kim, T. Niendorf, I. Karaman, On the Low Cycle Fatigue Response of CoCrNiFeMn High Entropy Alloy with Ultra-fine Grain Structure, Acta Materialia, 205 (2020) 116540.

[65] D.J. Morrison, Influence of grain size and texture on the cyclic stress-strain response of nickel, Materials Science and Engineering: A, 187 (1994) 11-21.

[66] D.J. Morrison, J.C. Moosbrugger, Effects of grain size on cyclic plasticity and fatigue crack initiation in nickel, International Journal of Fatigue, 19 (1997) 51-59.

[67] P. Li, S.X. Li, Z.G. Wang, Z.F. Zhang, Formation mechanisms of cyclic saturation dislocation patterns in [001], [011] and [-111] copper single crystals, Acta Materialia, 58 (2010) 3281-3294.

[68] X.W. Li, Y. Zhou, W.W. Guo, G.P. Zhang, Characterization of dislocation structures in copper single crystals using electron channelling contrast technique in SEM, Crystal Research and Technology: Journal of Experimental and Industrial Crystallography, 44 (2009) 315-321.

[69] P. Li, S. Li, Z. Wang, Z. Zhang, Fundamental factors on formation mechanism of dislocation arrangements in cyclically deformed fcc single crystals, Progress in Materials Science, 56 (2011) 328-377.

[70] M.S. Pham, S.R. Holdsworth, K.G.F. Janssens, E. Mazza, Cyclic deformation response of AISI 316L at room temperature: Mechanical behaviour, microstructural evolution, physically-based evolutionary constitutive modelling, International Journal of Plasticity, 47 (2013) 143-164.

[71] J.Y. He, W.H. Liu, H. Wang, Y. Wu, X.J. Liu, T.G. Nieh, Z.P. Lu, Effects of Al addition on structural evolution and tensile properties of the FeCoNiCrMn high-entropy alloy system, Acta Materialia, 62 (2014) 105-113.

[72] J.M. Park, J. Moon, J.W. Bae, J. Jung, S. Lee, H.S. Kim, Effect of annealing heat treatment on microstructural evolution and tensile behavior of Al0.5CoCrFeMnNi high-entropy alloy, Materials Science and Engineering: A, 728 (2018) 251-258.

[73] H.T. Jeong, W.J. Kim, Microstructure tailoring of Al0.5CoCrFeMnNi to achieve high strength and high uniform strain using severe plastic deformation and an annealing treatment, Journal of Materials Science & Technology, 71 (2021) 228-240.

[74] S. Shukla, T. Wang, S. Cotton, R.S. Mishra, Hierarchical microstructure for improved fatigue properties in a eutectic high entropy alloy, Scripta Materialia, 156 (2018) 105-109.

[75] K. Liu, M. Komarasamy, B. Gwalani, S. Shukla, R.S. Mishra, Fatigue behavior of ultrafine grained triplex Al0. 3CoCrFeNi high entropy alloy, Scripta Materialia, 158 (2019) 116-120.

[76] R. Feng, Y. Rao, C. Liu, X. Xie, D. Yu, Y. Chen, M. Ghazisaeidi, T. Ungar, H. Wang, K. An, P.K. Liaw, Enhancing fatigue life by ductile-transformable multicomponent B2 precipitates in a high-entropy alloy, Nat Commun, 12 (2021) 3588.

[77] J.-P. Zou, X.-M. Luo, B. Zhang, Y.-W. Luo, H.-L. Chen, F. Liang, G.-P. Zhang, Enhancing bending fatigue resistance of the CoCrFeMnNi high-entropy alloy thin foils by Al addition, Materials Science and Engineering: A, 831 (2022).

[78] A. Chauhan, Deformation and damage mechanisms of ODS steels under high-temperature cyclic loading, Karlsruhe Institute of Technology, Dissertation, (2018).

[79] C. Petersen, V. Shamardin, A. Fedoseev, G. Shimansky, V. Efimov, J. Rensman, The ARBOR irradiation project, Journal of Nuclear Materials, 307-311 (2002) 1655-1659.

[80] A. E2714-13, Standard Test Method for Creep-Fatigue Testing, ASTM International, West Conshohocken, PA, (2013) 1-15.

[81] M.S. Pham, C. Solenthaler, K.G.F. Janssens, S.R. Holdsworth, Dislocation structure evolution and its effects on cyclic deformation response of AISI 316L stainless steel, Materials Science and Engineering: A, 528 (2011) 3261-3269.

[82] M. Calcagnotto, D. Ponge, E. Demir, D. Raabe, Orientation gradients and geometrically necessary dislocations in ultrafine grained dual-phase steels studied by 2D and 3D EBSD, Materials Science and Engineering: A, 527 (2010) 2738-2746.

[83] P.B. Hirsch, A. Howie, R.B. Nicholson, D.W. Pashley, M.J. Whelan, L. Marton, Electron Microscopy of Thin Crystals, Physics Today, 19 (1966) 93-95.

[84] D.B. Williams, C.B. Carter, The transmission electron microscope, in: Transmission electron microscopy, Springer, New York, 1996, pp. 3-17.

[85] Brent Fultz, J. Howe, Transmission Electron Microscopy, Springer, New York, 2008.

[86] K. Lu, A. Chauhan, A.S. Tirunilai, J. Freudenberger, A. Kauffmann, M. Heilmaier, J. Aktaa, Deformation mechanisms of CoCrFeMnNi high-entropy alloy under low-cycle-fatigue loading, Acta Materialia, 215 (2021) 117089.

[87] J. Morrow, Cyclic plastic strain energy and fatigue of metals, Internal friction, damping, and cyclic plasticity, ASTM International, (1965) 45–87.

[88] C.E. Feltner, C. Laird, Cyclic stress-strain response of F.C.C. metals and alloys-I Phenomenological experiments, Acta Metallurgica, 15 (1967) 1621-1632.

[89] D. Han, Y.J. Zhang, X.W. Li, A crucial impact of short-range ordering on the cyclic deformation and damage behavior of face-centered cubic alloys: A case study on Cu-Mn alloys, Acta Materialia, 205 (2021) 116559.

[90] S.S. Manson, Behavior of materials under conditions of thermal stress, National Advisory Committee for Aeronautics, 1953.

[91] L. Coffin Jr, A study of the effects of cyclic thermal stresses on a ductile metal, Transactions of the American Society of Mechanical Engineers, New York, 76 (1954) 931-950.

[92] K. Lu, A. Chauhan, D. Litvinov, J. Aktaa, Temperature-dependent cyclic deformation behavior of CoCrFeMnNi high-entropy alloy, International Journal of Fatigue, 160 (2022) 106863.

[93] Y. Li, C. Laird, Cyclic response and dislocation structures of AISI 316L stainless steel. Part 2: polycrystals fatigued at intermediate strain amplitude, Materials Science and Engineering: A, 186 (1994) 87-103.

[94] H. Mughrabi, Dislocation wall and cell structures and long-range internal stresses in deformed metal crystals, Acta Metallurgica, 31 (1983) 1367-1379.

[95] T. Tabata, H. Fujita, M.-A. Hiraoka, K. Onishi, Dislocation behaviour and the formation of persistent slip bands in fatigued copper single crystals observed by high-voltage electron microscopy, Philosophical Magazine A, 47 (1983) 841-857.

[96] K. Obrtlík, T. Kruml, J. Polák, Dislocation structures in 316L stainless steel cycled with plastic strain amplitudes over a wide interval, Materials Science and Engineering: A, 187 (1994) 1-9.

[97] M. Gerland, J. Mendez, P. Violan, B. Ait Saadi, Evolution of dislocation structures and cyclic behaviour of a 316L-type austenitic stainless steel cycled in vacuo at room temperature, Materials Science and Engineering: A, 118 (1989) 83-95.

[98] P. Lukáš, L. Kunz, Role of persistent slip bands in fatigue, Philosophical Magazine, 84 (2004) 317-330.

[99] S.J. Basinski, Z.S. Basinski, A. Howie, Early stages of fatigue in copper single crystals, The Philosophical Magazine: A Journal of Theoretical Experimental and Applied Physics, 19 (1969) 899-924.

[100] A. Winter, O. Pedersen, K. Rasmussen, Dislocation microstructures in fatigued copper polycrystals, Acta Metallurgica, 29 (1981) 735-748.

[101] M. Gerland, P. Violan, Secondary cyclic hardening and dislocation structures in type 316 stainless steel at 600°C, Materials Science and Engineering, 84 (1986) 23-33.

[102] D. Kuhlmann-Wilsdorf, C. Laird, Dislocation behavior in fatigue, Materials Science and Engineering, 27 (1977) 137-156.

[103] D. Kuhlmann-Wilsdorf, Theory of plastic deformation:-properties of low energy dislocation structures, Materials Science and Engineering: A, 113 (1989) 1-41.

[104] L. Kubin, M. Sauzay, Persistent slip bands: The bowing and passing model revisited, Acta Materialia, 132 (2017) 517-524.

[105] M.A. Meyers, O. Vöhringer, V.A. Lubarda, The onset of twinning in metals: a constitutive description, Acta Materialia, 49 (2001) 4025-4039.

[106] R. Zhang, S. Zhao, J. Ding, Y. Chong, T. Jia, C. Ophus, M. Asta, R.O. Ritchie, A.M. Minor, Short-range order and its impact on the CrCoNi medium-entropy alloy, Nature, 581 (2020) 283-287.

[107] S.I. Hong, C. Laird, Mechanisms of slip mode modification in F.C.C. solid solutions, Acta Metallurgica et Materialia, 38 (1990) 1581-1594.

[108] J. Cohen, M. Fine, Some aspects of short-range order, J. Phys. Radium, 23 (1962) 749-762.

[109] Q.J. Li, H. Sheng, E. Ma, Strengthening in multi-principal element alloys with local-chemical-order roughened dislocation pathways, Nat Commun, 10 (2019) 3563.

[110] S.M. Copley, B.H. Kear, The dependence of the width of a dissociated dislocation on dislocation velocity, Acta Metallurgica, 16 (1968) 227-231.

[111] C. Buque, J. Bretschneider, A. Schwab, C. Holste, Dislocation structures in cyclically deformed nickel polycrystals, Materials Science and Engineering: A, 300 (2001) 254-262.

[112] Y. El-Madhoun, A. Mohamed, M. Bassim, Cyclic stress–strain behavior of polycrystalline nickel, Materials Science and Engineering: A, 385 (2004) 140-147.

[113] H. Suzuki, Chemical interaction of solute atoms with dislocations, Sci. Rep. Res. Inst. Tohoku Univ. A, 4 (1952) 455-463.

[114] P. Gallagher, The influence of alloying, temperature, and related effects on the stacking fault energy, Metallurgical Transactions, 1 (1970) 2429-2461.

[115] H. Saka, Experimental evidence for Suzuki segregation to the stacking fault of an extended dislocation in a Cu-Si alloy, Philosophical Magazine A, 47 (1983) 131-140.

[116] Y. Kaneko, K. Kaneko, A. Nohara, H. Saka, Evidence for Suzuki effect in an Fe-Ni-Cr austenitic stainless steel, Philosophical Magazine A, 71 (1995) 399-407.

[117] G.B. Viswanathan, R. Shi, A. Genc, V.A. Vorontsov, L. Kovarik, C.M.F. Rae, M.J. Mills, Segregation at stacking faults within the γ′ phase of two Ni-base superalloys following intermediate temperature creep, Scripta Materialia, 94 (2015) 5-8.

[118] G.W. Han, I.P. Jones, R.E. Smallman, Direct evidence for Suzuki segregation and Cottrell pinning in MP159 superalloy obtained by FEG(S)TEM/EDX, Acta Materialia, 51 (2003) 2731-2742.

[119] Y. Koizumi, T. Nukaya, S. Suzuki, S. Kurosu, Y. Li, H. Matsumoto, K. Sato, Y. Tanaka, A. Chiba, Suzuki segregation in Co–Ni-based superalloy at 973K: An experimental and computational study by phase-field simulation, Acta Materialia, 60 (2012) 2901-2915.

[120] M. Kawamura, M. Asakura, N.L. Okamoto, K. Kishida, H. Inui, E.P. George, Plastic deformation of single crystals of the equiatomic Cr−Mn−Fe−Co−Ni high-entropy alloy in tension and compression from 10 K to 1273 K, Acta Materialia, 203 (2021) 116454.

[121] B. Schuh, F. Mendez-Martin, B. Völker, E.P. George, H. Clemens, R. Pippan, A. Hohenwarter, Mechanical properties, microstructure and thermal stability of a nanocrystalline CoCrFeMnNi high-entropy alloy after severe plastic deformation, Acta Materialia, 96 (2015) 258-268.

[122] J.Y. He, C. Zhu, D.Q. Zhou, W.H. Liu, T.G. Nieh, Z.P. Lu, Steady state flow of the FeCoNiCrMn high entropy alloy at elevated temperatures, Intermetallics, 55 (2014) 9-14.

[123] F. Otto, A. Dlouhý, K.G. Pradeep, M. Kuběnová, D. Raabe, G. Eggeler, E.P. George, Decomposition of the single-phase high-entropy alloy CrMnFeCoNi after prolonged anneals at intermediate temperatures, Acta Materialia, 112 (2016) 40-52.

[124] W. Zhou, L.M. Fu, P. Liu, X.D. Xu, B. Chen, G.Z. Zhu, X.D. Wang, A.D. Shan, M.W. Chen, Deformation stimulated precipitation of a single-phase CoCrFeMnNi high entropy alloy, Intermetallics, 85 (2017) 90-97.

[125] E.J. Pickering, R. Muñoz-Moreno, H.J. Stone, N.G. Jones, Precipitation in the equiatomic high-entropy alloy CrMnFeCoNi, Scripta Materialia, 113 (2016) 106-109.

[126] M. Heczko, V. Mazánová, R. Gröger, T. Záležák, M.S. Hooshmand, E.P. George, M.J. Mills, A. Dlouhý, Elemental segregation to lattice defects in the CrMnFeCoNi high-entropy alloy during high temperature exposures, Acta Materialia, 208 (2021) 116719.

[127] S. Hong, K. Lee, S. Lee, Dynamic strain aging effect on the fatigue resistance of type 316L stainless steel, International Journal of Fatigue, 27 (2005) 1420-1424.

[128] H. Zhou, Y. He, M. Cui, Y. Cen, J. Jiang, Dependence of dynamic strain ageing on strain amplitudes during the low-cycle fatigue of TP347H austenitic stainless steel at 550°C, International Journal of Fatigue, 56 (2013) 1-7.

[129] S. Goyal, S. Mandal, P. Parameswaran, R. Sandhya, C.N. Athreya, K. Laha, A comparative assessment of fatigue deformation behavior of 316 LN SS at ambient and high temperature, Materials Science and Engineering: A, 696 (2017) 407-415.

[130] M.S. Pham, S.R. Holdsworth, Dynamic strain ageing of AISI 316L during cyclic loading at 300°C: Mechanism, evolution, and its effects, Materials Science and Engineering: A, 556 (2012) 122-133.

[131] M. Valsan, D. Sastry, K.B. Sankara Rao, S. Mannan, Effect of strain rate on the high-temperature low-cycle fatigue properties of a nimonic PE-16 superalloy, Metallurgical and materials transactions a, 25 (1994) 159-171.

[132] S. Hong, The tensile and low-cycle fatigue behavior of cold worked 316L stainless steel: influence of dynamic strain aging, International Journal of Fatigue, 26 (2004) 899-910.

[133] R. Sandhya, K.B.S. Rao, S. Mannan, R. Devanathan, Substructural recovery in a cold worked Ti-modified austenitic stainless steel during high temperature low cycle fatigue, International journal of fatigue, 23 (2001) 789-797.

[134] S.K. Krovvidi, S. Goyal, A. Bhaduri, Low cycle fatigue and creep-fatigue response of the 316Ti stainless steel, Frattura ed Integrità Strutturale, 13 (2019) 577-584.

[135] R. Carroll, C. Lee, C.W. Tsai, J.W. Yeh, J. Antonaglia, B.A. Brinkman, M. LeBlanc, X. Xie, S. Chen, P.K. Liaw, K.A. Dahmen, Experiments and Model for Serration Statistics in Low-Entropy, Medium-Entropy, and High-Entropy Alloys, Scientific Repports, 5 (2015) 16997.

[136] H.Y. Yasuda, K. Shigeno, T. Nagase, Dynamic strain aging of Al0.3CoCrFeNi high entropy alloy single crystals, Scripta Materialia, 108 (2015) 80-83.

[137] M. Komarasamy, K. Alagarsamy, R.S. Mishra, Serration behavior and negative strain rate sensitivity of Al0.1CoCrFeNi high entropy alloy, Intermetallics, 84 (2017) 20-24.

[138] S. Chen, X. Xie, B. Chen, J. Qiao, Y. Zhang, Y. Ren, K.A. Dahmen, P.K. Liaw, Effects of Temperature on Serrated Flows of Al0.5CoCrCuFeNi High-Entropy Alloy, Jom, 67 (2015) 2314-2320.

[139] S. Chen, X. Xie, W. Li, R. Feng, B. Chen, J. Qiao, Y. Ren, Y. Zhang, K.A. Dahmen, P.K. Liaw, Temperature effects on the serrated behavior of an Al0.5CoCrCuFeNi high-entropy alloy, Materials Chemistry and Physics, 210 (2018) 20-28.

[140] P. G. McCormick, A model for the Portevin-Le Chatelier effect in substitutional alloys, Acta Metallurgica, 20 (1972) 351-354.

[141] A.H. Cottrell, D. Dexter, Dislocations and plastic flow in crystals, American journal of physics, 22 (1954) 242-243.

[142] S. Huang, W. Li, S. Lu, F. Tian, J. Shen, E. Holmström, L. Vitos, Temperature dependent stacking fault energy of FeCrCoNiMn high entropy alloy, Scripta Materialia, 108 (2015) 44-47.

[143] Y.B. Kang, S.H. Shim, K.H. Lee, S.I. Hong, Dislocation creep behavior of CoCrFeMnNi high entropy alloy at intermediate temperatures, Materials Research Letters, 6 (2018) 689-695.

[144] D.W. Kim, W.-S. Ryu, J.H. Hong, S.-K. Choi, Effect of nitrogen on high temperature low cycle fatigue behaviors in type 316L stainless steel, Journal of Nuclear Materials, 254 (1998) 226-233.

[145] V.S. Srinivasan, M. Valsan, R. Sandhya, K. Bhanu Sankara Rao, S.L. Mannan, D.H. Sastry, High temperature time-dependent low cycle fatigue behaviour of a type 316L(N) stainless steel, International Journal of Fatigue, 21 (1999) 11-21.

[146] S.L. Mannan, Role of dynamic strain ageing in low cycle fatigue, Bulletin of Materials Science, 16 (1993) 561-582.

[147] J. Polák, R. Petráš, M. Heczko, I. Kuběna, T. Kruml, G. Chai, Low cycle fatigue behavior of Sanicro25 steel at room and at elevated temperature, Materials Science and Engineering: A, 615 (2014) 175-182.

[148] A. Chauhan, J. Hoffmann, D. Litvinov, J. Aktaa, High-temperature low-cycle fatigue behavior of a 9Cr-ODS steel: Part 1 - pure fatigue, microstructure evolution and damage characteristics, Materials Science and Engineering: A, 707 (2017) 207-220.

[149] N.L. Okamoto, K. Yuge, K. Tanaka, H. Inui, E.P. George, Atomic displacement in the CrMnFeCoNi high-entropy alloy – A scaling factor to predict solid solution strengthening, AIP Advances, 6 (2016) 125008.

[150] M. Schneider, E.P. George, T.J. Manescau, T. Záležák, J. Hunfeld, A. Dlouhý, G. Eggeler, G. Laplanche, Analysis of strengthening due to grain boundaries and annealing twin boundaries in the CrCoNi medium-entropy alloy, International Journal of Plasticity, 124 (2020) 155-169.

[151] M. Heczko, V. Mazánová, C.E. Slone, M. Shih, E.P. George, M. Ghazisaeidi, J. Polák, M.J. Mills, Role of deformation twinning in fatigue of CrCoNi medium-entropy alloy at room temperature, Scripta Materialia, 202 (2021) 113985.

[152] T. Mayama, K. Sasaki, M. Kuroda, Quantitative evaluations for strain amplitude dependent organization of dislocation structures due to cyclic plasticity in austenitic stainless steel 316L, Acta Materialia, 56 (2008) 2735-2743.

[153] M.S. Pham, S.R. Holdsworth, Role of microstructural condition on fatigue damage development of AISI 316L at 20 and 300°C, International Journal of Fatigue, 51 (2013) 36-48.

[154] T. Magnin, C. Ramade, J. Lepinoux, L.P. Kubin, Low-cycle fatigue damage mechanisms of F.c.c. and B.c.c. polycrystals: Homologous behaviour?, Materials Science and Engineering: A, 118 (1989) 41-51.

[155] K. Lu, F. Knöpfle, A. Chauhan, H.T. Jeong, D. Litvinov, M. Walter, W.J. Kim, J. Aktaa, Low-cycle fatigue behavior and deformation mechanisms of a dual-phase Al0.5CoCrFeMnNi high-entropy alloy, International Journal of Fatigue, 163 (2022) 107075.

List of Tables

List of Figures

List of Publications [5]

Contributions in journals:

1. K. Lu, A. Chauhan, A.S. Tirunilai, J. Freudenberger, A. Kauffmann, M. Heilmaier, J. Aktaa, Deformation mechanisms of CoCrFeMnNi high-entropy alloy under low-cycle-fatigue loading, Acta Materialia 215 (2021) 117089.

2. K. Lu, A. Chauhan, M. Walter, A.S. Tirunilai, M. Schneider, G. Laplanche, J. Freudenberger, A. Kauffmann, M. Heilmaier, J. Aktaa, Superior low-cycle fatigue properties of CoCrNi compared to CoCrFeMnNi, Scripta Materialia 194 (2021) 113667.

3. K. Lu, A. Chauhan, D. Litvinov, M. Walter, A.S. Tirunilai, J. Freudenberger, A. Kauffmann, M. Heilmaier, J. Aktaa, High-temperature low cycle fatigue behavior of an equiatomic CoCrFeMnNi high-entropy alloy, Materials Science and Engineering: A 791 (2020) 139781.

4. K. Lu, A. Chauhan, D. Litvinov, J. Aktaa, Temperature-dependent cyclic deformation behavior of CoCrFeMnNi high-entropy alloy, International Journal of Fatigue 160 (2022) 106863.

5. K. Lu, F. Knöpfle, A. Chauhan, H.T. Jeong, D. Litvinov, M. Walter, W.J. Kim, J. Aktaa, Low-cycle fatigue behavior and deformation mechanisms of a dual-phase Al0.5CoCrFeMnNi high-entropy alloy, International Journal of Fatigue, 163 (2022) 107075.

6. K. Lu, A. Chauhan, D. Litvinov, A.S. Tirunilai, J. Freudenberger, A. Kauffmann, M. Heilmaier, J. Aktaa, Micro-mechanical deformation behavior of CoCrFeMnNi high-entropy alloy, Journal of Materials Science & Technology, 100 (2022) 237-245.

[5] Publications 1-4, and part of publication 5 are from the current thesis.

7. K. Lu, A. Chauhan, F. Knöpfle, J. Aktaa, Effective and back stresses evolution upon cycling a high-entropy alloy, Materials Research Letters, 10 (2022) 369-376.

8. K. Lu, F. Knöpfle, A. Chauhan, D. Litvinov, M. Schneider, G. Laplanche, J. Aktaa, Elevated-temperature cyclic deformation mechanisms of CoCrNi in comparison to CoCrFeMnNi, Scripta Materialia, 220 (2022) 114926.

9. K. Lu, A. Chauhan, D. Litvinov, M. Schneider, G. Laplanche, J. Aktaa, Fatigue deformation mechanisms in a CoCrNi multi-principal element alloy: A case of low stacking fault energy, To be submitted (2022).

Contributions in Conferences (*presenter):

1. K. Lu*, A. Chauhan, A. S. Tirunilai, M. Schneider, G. Laplanche, J. Freudenberger, A. Kauffmann, M. Heilmaier, J. Aktaa, Low-cycle fatigue behaviors of medium-entropy CrCoNi and high-entropy CrCoFeMnNi alloys, 3rd International Conference on High Entropy Materials, Sep 27 - Oct 01, 2020, Berlin, Germany (Oral talk).

2. K. Lu*, A. Chauhan, A. S. Tirunilai, M. Schneider, G. Laplanche, J. Freudenberger, A. Kauffmann, M. Heilmaier, J. Aktaa, Low-cycle fatigue behavior and deformation mechanisms of CoCrFeMnNi and CoCrNi, 9th International Conference on Low Cycle Fatigue, June 21 - June 23 2022, Berlin, Germany (Oral talk).

3. K. Lu*, F. Knöpfle, A. Chauhan, H.T. Jeong, D. Litvinov, M. Walter, W.J. Kim, J. Aktaa, Low-cycle fatigue behavior and deformation mechanisms of a dual-phase Al0.5CoCrFeMnNi high-entropy alloy, 19th International Conference on Strength of Materials, June 26 - July 1 2022, Metz, France (Oral talk).

4. K. Lu*, A. Chauhan, D. Litvinov, J. Aktaa, Temperature-dependent cyclic deformation behavior of CoCrFeMnNi with comparison to CoCrNi, Sep 27- Sep 29 2022, Darmstat, Germany (Poster).

5. K. Lu, A. Chauhan, A. S. Tirunilai, A. Kauffmann, M. Heilmaier, M. Schneider, G. Laplanche, J. Freudenberger, J. Aktaa*, Deformation mechanisms of CoCrNi and CoCrFeMnNi MPEAs under low-cycle fatigue loading: Comparison and correlation with lifetime, 2023 TMS Annual Meeting & Exhibition, Fatigue in Materials: Fundamentals, Multiscale Characterizations and Computational Modeling, to be held, March 19 - March 23, 2023, San Diego, California, USA (Invited talk).

Acknowledgments

First, I would like to express my deepest gratitude to my supervisor Prof. Dr. Jarir Aktaa for offering me the exciting opportunity to pursue a PhD degree in his group. This thesis and the efforts captured during my PhD could not have been achieved without his solid support, suggestions and continuous encouragement. I am also grateful for the research freedom he provided, which allows me to freely explore the open interesting questions; and I really enjoyed this journey. I also thank him for supporting me to attend international conferences, which gave me the opportunity to discuss with many international colleagues (famous professors and young researchers), stimulated and further my research.

I take this opportunity to thank Prof. Dr. Martin Heilmaier for his willingness to provide a second review for this thesis and for his valuable and critical comments during my PhD. With his advice, I always try to be more critical about my work. I also thank Prof. Dr. Thomas Böhlke for being a chair of my PhD examination.

I am deeply grateful to Dr. Ankur Chauhan, who has been a second advisor to me. Ankur has been an excellent example of patience and kindness, and he is a role model for me as a young researcher. I am really glad to work with him and learned a lot from him.

I am also thankful to Dr. Alexandre Kauffmann, Dr. Aditya Srinivasan Tirunilai, Prof. Dr. Guillaume Laplanche, and Prof. Dr. Jens Freudenberger for their valuable insights to my work and generous support in providing the investigated materials.

I express my thanks to Dr. Mario Walter and Dr. Dimitri Litvinov for the fruitful discussion and for guiding me using the fatigue testing machine and electron microscopies. I also thank Melina Blem, Edmund Böck, Ewald Ernst, Ralf Dahm, Steffen Kohnle, and Dr. Reiner Mönig for their help in my experiments.

Sincere thanks to my nice colleagues Dr. Ermile Gaganidze, Qian Yuan, Mathias Jetter, Roshan Rajakrishnan, Dr. Jie Gao, Dr. Kuo Zhang, Dr. Thilo Grammes and other members of the institute for providing a wonderful and warm environment. Thanks to

Fabian Knöpfle for the help in translating the abstract into the German version and the fruitful discussion during his master thesis work.

Special thanks to KIT library for 365-days opening, which gives me opportunity working on many weekends.

Thanks to my friends Huihuang Xia, Dr. Kai Wu, Dr. Hao Shi, Dr. Qing Zhou, Dr. Juan Li and many other friends for their help during my stay in Germany.

Lastly, I am deeply indebted to my wife (Chengfeng Dong), my parents and little sister. They have always been showing their support, patience and love these years.

This thesis marks the end of my time at KIT and the beginning of my next career. I hope that in the future, I can maintain the passion for open questions and research that I have developed during my PhD.